Charles University

Faculty of Science

Study programme: Biology

Branch of study: Cellular and Developmental Biology – Cell Physiology

Bc. Václav Bočan

Searching for microtubule inner proteins

Pátrání po vnitřních proteinech mikrotubulů

Master's thesis

Supervisor: RNDr. Lenka Libusová, Ph.D.

Prague, 2021

Acknowledgement

Tuhle práci bych nenapsal bez tvé obětavé podpory a lásky, Kadlíku. Za to jsem ti navždy zavázán. Lenko, tobě děkuji za trpělivost, vedení a všechny připomínky. Vojtovi, Terce a Štěpánce patří velké poděkování za to, jakou skvělou (někdy i pracovní) atmosféru v našem doupěti tvoří. Bude mi chybět! Johanna, I owe you a big thank for your supporting but honest attitude. Shame I couldn't spend longer time at your lab. Davide, working with you was a great pleasure, hope you're doing great in the UK. Ondru Honcovi a dr. Radovanu Fišerovi jsem vděčný za nezištnou a nadstandardní pomoc se sortem a fluorescenční spektrometrií. Spermie jsou tvrdohlavé, co naplat, ale díky vám si daly říct. Bez darovaného materiálu od Vladimíra Vargy, Ondry Šimoníka, ISB Zásmuky (CRV Czech Republic, s. r. o.) a ISB Hradištko pod Medníkem (Natural, s. r. o.) bych diplomku sotva mohl dokončit.

Má práce je tak i vaší prací. Děkuji!

Prohlášení

Prohlašuji, že jsem závěrečnou práci zpracoval samostatně a že jsem uvedl všechny použité informační zdroje a literaturu. Tato práce ani její podstatná část nebyla předložena k získání jiného nebo stejného akademického titulu.

Declaration

I honestly declare that I wrote this thesis on my own and that I stated all used literature and other information sources. This work or its significant part was not used to previously acquire any other or same academic title.

V Praze / In Prague, 2021-08-11

Abstract

Microtubules (MTs) – cylindrical polymers of α- and β-tubulin – maintain numerous irreplaceable functions in all eukaryotic cells. For this complex involvement of MTs in many cellular processes, precise tuning of their post-translational modifications, polymerization state, and interactome is crucial. Recently, a new mode of interactions with MTs was discovered – several microtubule inner proteins (MIPs) can enter the lumen of MTs.

Little is known about MIPs in dynamic MTs in the cytoplasmic network. Only two proteins have been shown to bind to the inside of dynamic MTs so far: αTAT1 and MAP6; other proteins have been suggested to. Stabilised MTs, like the axoneme of the flagellum, contain dozens of orderly bound MIPs in the lumen and new ones are being added. MIPs are believed to play a role during axonemal assembly and to increase the stiffness required for flagellar beating.

This diploma thesis investigated MIPs in both dynamic and axonemal MTs. In the first part of the thesis, the goal was to identify candidates for new MIPs in the dynamic MTs by two independent approaches – proximity-labelling by promiscuous biotin ligase using αTAT1 and MAP6 as baits, and direct isolation of MTs from cells and washing away outer proteins. Isolated proteins were then identified using mass spectrometry.

In the second part, the work aims to identify candidates for members of a newly discovered helical complex in the lumen of vertebrate sperm cell axoneme, termed TAILS (Tail Axoneme Intra-Lumenal Spiral). Candidates were identified by mass spectrometry analysis performed on isolated flagellum fragments, separated via cytometry sorting.

Keywords

microtubules, microtubule inner proteins, α-tubulin acetyltransferase 1 (αTAT1), microtubule-associated protein 6 (MAP6), tail axoneme intra-lumenal spiral (TAILS)

Abstrakt

Mikrotubuly – válcovité polymery α- a β-tubulinu – vykonávají v eukaryotických buňkách řadu nezastupitelných funkcí. Jelikož jsou zapojeny do mnoha buněčných dějů, jejich posttranslační modifikace, rychlost polymerizace a interaktom musí být pečlivě regulovány. V nedávné době byl objeven nový způsob interakce proteinů s mikrotubuly, a to v podobě vnitřních mikrotubulárních proteinů, které vstupují přímo do lumen mikrotubulů.

O vnitřních proteinech dynamických mikrotubulů v cytoplasmě je známo velmi málo. Zatím byly objeveny pouze dva: αTAT1 a MAP6. Stabilizované mikrotubuly, jako například ty v axonemě bičíku, obsahují desítky pravidelně uspořádaných vnitřních mikrotubulárních proteinů, přičemž jsou stále objevovány nové. Pravděpodobně hrají úlohu pro výstavbu axonemy a její zpevnění, což je nezbytné pro odolávání mechanickým silám vytvářeným v bičíku při pohybu.

Tato diplomová práce přispívá k poznání vnitřních mikrotubulárních proteinů, a to jak v dynamických, tak v axonemálních mikrotubulech. Ve své první části se práce věnuje hledání nových vnitřních proteinů uvnitř dynamických mikrotubulů. K dosažení tohoto cíle jsou využity dva nezávislé přístupy – značení sousedících proteinů pomocí nespecifické biotin ligázy, navedené do lumen mikrotubulu fúzí s proteinem αTAT1 nebo MAP6, a přímá izolace mikrotubulů z buněčné kultury, z jejichž povrchu byly odmyty vnější proteiny. Izolované proteiny jsou následně identifikovány pomocí hmotnostní spektrometrie.

Druhá část práce se věnuje identifikaci kandidátů na členy nově objeveného helikálního komplexu jménem TAILS, který má podobu spirály uvnitř mikrotubulů bičíku spermií. Kandidátní proteiny jsou identifikovány pomocí hmotnostní spektrometrické analýzy vzorků nabohacených o fragmenty bičíku spermií pomocí třídicí průtokové cytometrie.

Klíčová slova

mikrotubuly, vnitřní mikrotubulární proteiny, α-tubulin acetyltransferáza 1 (αTAT1), protein asociovaný s mikrotubuly 6 (MAP6), tail axoneme intra-lumenal spiral (TAILS)

List of abbreviations

- AU – arbitrary units
- BioID – proximity-dependent biotin identification
- BLAST – Basic Local Alignment Search Tool
- BP – bandpass
- BSA – bovine serum albumin
- DAPI – 4′,6-diamidino-2-phenylindole
- DCDC2C – doublecortin domain-containing 2C
- dH_2O – distilled water
- DIC – differential interference contrast
- DM – dichroic mirror
- DMEM – Dulbecco's modified eagle medium
- DMSO – dimethyl sulfoxide
- dNTPs – deoxyribonucleoside triphosphates
- EGTA – ethylene glycol-bis(2-aminoethylether)-N,N,N',N'-tetraacetic acid
- EM – electron microscope, electron microscopy
- ET – electron tomography
- FACS – fluorescence-activated cell sorting
- Flp-in – flippase-in system
- FRT – flippase recognition target
- FSC-A – forward scatter, area of peak
- GDP – guanosine diphosphate
- GFP – green fluorescent protein
- GTP – guanosine triphosphate
- HDAC6 – histone deacetylase 6
- HRP – horseradish peroxidase
- IF – immunofluorescence, immunofluorescent
- K40 – lysine 40
- LP – longpass
- MAP – microtubule-associated protein
- MIP – microtubule inner protein
- MS – mass spectrometry
- MT – microtubule, microtubular
- MTD – microtubule doublet
- PAGE – polyacrylamide gel electrophoresis
- PBS – phosphate buffer saline
- PCR – polymerase chain reaction
- PD – Petri dish
- PFA – paraformaldehyde
- PTM – post-translational modification
- RPE – retina pigment epithelium
- SDS – sodium dodecyl sulphate
- SSC-A – side scatter, area of peak
- STOP – Stable Tubule-Only Polypeptide
- TAILS – Tail Axoneme Intra-Lumenal Spiral
- TB – transformation buffer
- TEMED – tetramethylethylenediamine
- Tet-On – tetracycline-inducible expression system
- U2OS – U-2 osteosarcoma
- αTAT1 – α-tubulin acetyltransferase 1 *(not to be confused with TAT1 tubulin antibody)*

A minuscule letter "s" is added to denote plural form, e. g. MTs = microtubules.

Table of Contents

1. Introduction

1.1. The microtubule

Microtubules (MTs) are cylindrical polymers of α- and β-tubulin dimers (Ludueña *et al.* 1977), associated in a head-to-tail alternating manner (Erickson 1974, Baker & Amos 1978). Longitudinal association of multiple tubulin heterodimers gives rise to tubulin protofilaments within one MT, most often in the number of 13 (Tilney *et al.* 1973), but exceptions exist (e. g. 11 and 15 protofilaments in MTs of *Caenorhabditis elegans*, (Chalfie & Thomson 1982)). The whole MT is a polarized structure – at the minus end, α-tubulin is exposed; the plus end terminates by β-tubulin (Nogales *et al.* 1999). The approximate outer diameter of MTs is 25 nm, the lumen has a diameter of 14–15 nm (Nogales *et al.* 1998, Shida *et al.* 2010). A schematic depiction of MT structure is in **Fig. 1**.

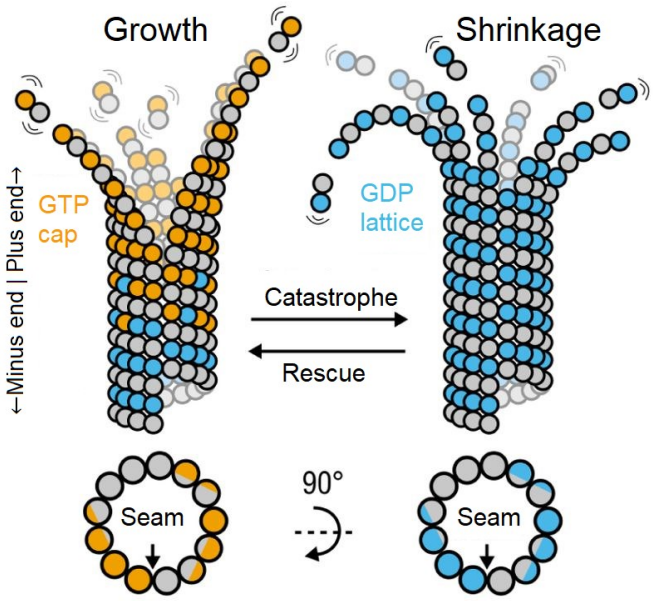

Fig. 1: Schematic representation of a microtubule and its dynamics. β-tubulin subunits are in colour (orange – GTP-bound, blue – GDP-bound), α-tubulin is in grey. Phases of growth by addition of new tubulin dimers and phases of depolymerization by loss of dimers switches stochastically (in events called catastrophes and rescues). Catastrophes occur when the GTP cap at the plus end is lost. The position of the seam – the discontinuous lateral contact of α- and β-tubulin subunit in the lattice – is indicated. Reprinted from (Igaev & Grubmüller 2020), modified.

In the cytoplasm, α- and β-tubulin dimerize with the dissociation constant of 10^{-11} mol/l. Given the usual concentrations of tubulin in a mammalian cell, virtually all tubulin is in the dimeric form (Caplow & Fee 2002). Both α- and β-tubulin bind guanosine triphosphate (GTP), but only the β-tubulin subunit can hydrolyse GTP to guanosine diphosphate (GDP) (Nogales *et al.* 1998). GTPase activity is present in assembled MTs only, free tubulin dimers do not hydrolyse GTP (David-Pfeuty *et al.* 1977). Simultaneous addition of GTP-bound tubulin dimers to the plus end and simultaneous hydrolysis of GTP on β-tubulin yielding GDP in the lattice give rise to pertaining GTP region at the very plus end (Roostalu *et al.* 2020), called the GTP cap. The GTP/GDP state, among other things, dictates the dynamics of the MT (**Fig. 1**).

1.1.1. Dynamics of MTs

MTs can grow on both ends by polymerization of tubulin dimers (Mitchison & Kirschner 1984). The growth can switch to rapid depolymerization in events called catastrophes (Odde *et al.* 1995) and be rescued back to the growing phase (Walker *et al.* 1988). These transitions are called dynamic instability (Mitchison & Kirschner 1984), refer to **Fig. 1**. Catastrophes and rescues are not entirely stochastic events, since newly polymerized MTs show a lower probability of catastrophes than longer and older MTs (Odde *et al.* 1995, Gardner *et al.* 2011). A proposed explanation is that the structure of the plus end is evolving in time and possibly gathers defects that increase the chance of a catastrophe. The rescues could then happen preferentially at "GTP island" sites within the MT, where the hydrolysis of GTP in the lattice has not been completed (Dimitrov *et al.* 2008).

1.1.1.1. Dynamic and stable MTs

Not all MTs show identical dynamics. Some MTs manifest the classical dynamic instability behaviour (Mitchison & Kirschner 1984). Axonemal MTs, on the other hand, are far less dynamic (Orbach & Howard 2019), and their length is controlled by the transport of tubulin building blocks to the distal tip where the plus end of MTs is located (W. F. Marshall & Rosenbaum 2001), reviewed in (S. Kim & Dynlacht 2013). The minus end of axonemal MTs shows no observable turnover (W. F. Marshall & Rosenbaum 2001), so tubulin is effectively "buried" in the proximal part of the axoneme, being recycled only when the whole axoneme is disassembled. A more recent finding relativizes this claim, though, because MTs can incorporate tubulin dimers not only at the ends but also along their length (Schaedel *et al.* 2015). Additionally, there are indications that entry of material to the lumen of axonemal MTs post-assembly is possible (Vaughan *et al.* 2006).

Diversification of MTs to more and less dynamic takes place also in the growth cone of the neuron (the distal structure at the end of an axon which facilitates pathfinding and wiring to other neurons during development, reviewed in (Pinto-Costa & Sousa 2021)). In the growth cone, highly dynamic MTs protrude into sprouting and retracting filopodia; stabilised MTs are present in the axon shaft (Schaefer *et al.* 2002). Participation of MTs in specialized cellular structures (like the growth cone) is however not necessary for observing differences in dynamics of MTs within one cell – individual MTs in the cytoplasm of fibroblasts can have different dynamics, which cannot be inferred from their spatial arrangement (Webster & Borisy 1989). Another example is found in the bristles of *Drosophila*: MTs constitute there two distinct populations with different dynamics and preferred orientations (Bitan *et al.* 2012). Distinct dynamics might stem from the need of functional specialization of MTs, e. g. for transport to the apical or basolateral side of a polarized epithelial cell (Poüs *et al.* 1998) Apparently, the dynamicity of MTs, together with the resistance to various depolymerization agents like detergents (Witman, Carlson, & Rosenbaum 1972) is rather a continuous spectrum than distinctive categories.

1.1.1.2. Selected modifiers of MT dynamics[1]

Post-translational modifications (PTMs) of tubulin (e. g. acetylation of α-tubulin) play an important role in the tuning of MT dynamics, reviewed in (MacTaggart & Kashina 2021). PTMs occur mostly at the acidic C-terminus of tubulin, exposed to the environment (Bigman & Levy 2020). The regulation of MT dynamics, stability, and potential to interact with various proteins through PTMs is called the tubulin code, summarized in (Janke 2014). Examples of the PTMs are detyrosination, polyglutamylation, and polyglycylation (happening at the C-terminal tail). Acetylation of lysine 40 (K40) of α-tubulin is located in the lumen (Nogales *et al.* 1999). This PTM is long-known (L'Hernault & Rosenbaum 1985). K40 is predominantly acetylated in long-lived and stable MTs (LeDizet & Piperno 1986). An ongoing debate is running whether K40 acetylation is a passive mark of stable MTs, or whether it contributes to the stability of MTs itself (Eshun-Wilson *et al.* 2019). The recent data suggest that K40 acetylation does affect the lattice – it weakens the lateral contacts of protofilaments, rendering them more flexible and less prone to spreading of defects like missing tubulin dimers (Eshun-Wilson *et al.* 2019).

Small molecules are another key tool to manipulate and probe the dynamics of MTs. Paclitaxel (also known by the registered name taxol) is widely used in experimental work and the treatment of cancer (Weaver 2014). Paclitaxel, isolated from the bark of *Taxus brevifolia*, stabilizes MTs against cold and calcium-induced damage, lowers the critical tubulin concentration needed for MT assembly, and prevents depolymerization (Schiff *et al.* 1979). The taxanoid binding site (where paclitaxel and related drugs bind) is located in the lumen of assembled MTs; paclitaxel passes the fenestrations in the MT lattice to enter the lumen (**Fig. 2**) (Nogales *et al.* 1995). More precisely, paclitaxel associates with an intermediate binding site available from the solution and is then flipped inside to its proper binding position (Freedman *et al.* 2009). Paclitaxel-bound MTs show increased flexibility and tend to have fewer protofilaments than drug-free MTs (Kellogg *et al.* 2017).

[1] A bewildering array of regulators (including proteins, post-translational modifications, and drugs) is known, and it is not possible to state a detailed description of each. We focus here only on the acetylation of lysine 40 in α-tubulin and a small molecule paclitaxel, since these are the most relevant for the results presented here.

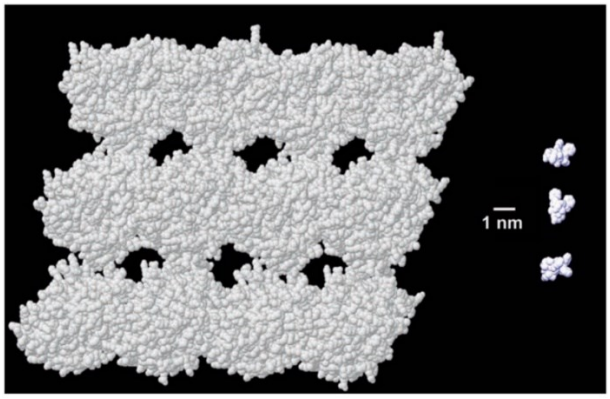

Fig. 2: Atomic van der Waals models of MT lattice and paclitaxel. Fenestrations in the MT lattice (light grey) are large enough to enable lumen entry of paclitaxel (white smaller molecules). Proteins are too bulky to enter via fenestrations. Reprinted from (José Fernando Díaz *et al.* 2003), modified.

1.1.2. The axoneme

MTs in the cilia and flagella[2] of most eukaryotic organisms assemble into a conserved structure called the axoneme (reviewed in (Ishikawa 2017)). The overall structure is depicted in **Fig. 3**. Usually, the axoneme comprises one central pair of single MTs, surrounded by nine outer MT doublets (MTDs) (Fawcett & Porter 1954) in the so-called "9 + 2" arrangement. In the MTD, one MT (called A-tubule) is fully assembled with 13 protofilaments, the B-tubule is attached to the A-tubule and contains only 10 protofilaments (reviewed in (Kohl & Bastin 2005)). 11th protofilament was sometimes distinguished in the B-tubule, but it is thinner (Nicastro *et al.* 2006) and is actually composed of other proteins than tubulin (Nicastro *et al.* 2011, Dymek *et al.* 2019).

The "9 + 2" arrangement does not apply to non-motile primary cilia, which lacks the central pair (Kiesel *et al.* 2020). Overall, human primary cilia are less organised as their "9 + 0" structure is present at the very base only. In more distal parts, the organization becomes less ordered since some MTs are terminating along the cilium, not only at its end (Kiesel *et al.* 2020). Furthermore, the "9 + 0" arrangement does not preclude the motility of the cilium, because some motile cilia were found to have this structure (Nonaka *et al.* 1998). "9 + 2" pattern is common but not universal; spiders, for instance, can possess "9 + 3" axoneme in their sperm cells (Dallai *et al.* 1995). Much more divergent patterns are to be found in protists, like the minimalistic motile flagellum with mere three MTDs ("3 + 0") in gregarine *Diplauxis hatti* (Prensier *et al.* 1980).

In the motile cilia, the beating pattern is facilitated by the dynein molecular motors which are repeatedly switched on and off (J. Lin & Nicastro 2018). The dynein motors are protruding from the A-tubule and walk on the B-tubule of a neighbouring MTD (Walton *et al.* 2021) (**Fig. 3**). They are arranged into outer and inner dynein arms and walk towards the minus end at the base of the axoneme (Schroer *et al.* 1989). MTDs are interconnected with nexin links, which, besides other roles, help to redistribute the mechanical load of dynein arms (Oda, Yanagisawa, & Kikkawa 2014).

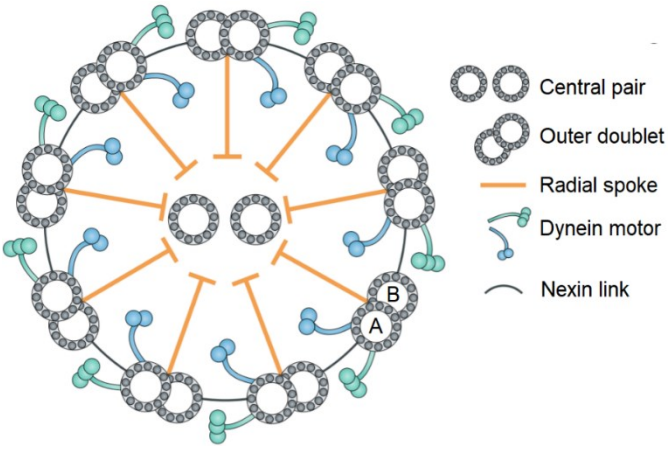

Fig. 3: A schematic structure of the axoneme on a transverse cut with the typical "9 + 2" arrangement. A central pair of singlet MTs is surrounded by 9 peripheral MTDs. In the MTD, one MT is complete with 13 protofilaments (the A-tubule), another incomplete MT with 10 protofilaments is attached to it (the B-tubule). Other structural features (radial spokes, dynein motors, and nexin links) are included. Reprinted from (Gilpin *et al.* 2020) and modified.

[2] The terms "cilium" and "flagellum" can be used interchangeably, their structure is identical (for motile cilia). Flagellum is more often used when referring to motile cells (like the sperm cell). Cilium is used when referring to nonmotile cells (like the airway epithelial cells).

1.2. MIPs in dynamic MTs[3]

1.2.1. Early discoveries of MIPs

Since early EM (electron microscopy) structural studies using chemical fixation of cells followed by heavy metal staining, MTs were observed to sometimes contain luminal material. This was confirmed for human blood platelets (Xu & Afzelius 1988), frog olfactory neurons (Burton 1984), or frog gliocytes (Rodríguez Echandía *et al.* 1968). No data were published on the identity or function of the luminal content at the time since resolving molecular details were unreachable with that method. Furthermore, from today's perspective, some but not all of the observations of dark-lumen MTs could be possibly attributed to staining artefacts (e. g. dark-lumen MTs in (Sandborn *et al.* 1964)). An example of dense-core MTs stained with heavy metals is in **Fig. 4**. Later, these proteins inside microtubules were named microtubule inner proteins (MIPs) (Nicastro *et al.* 2006).

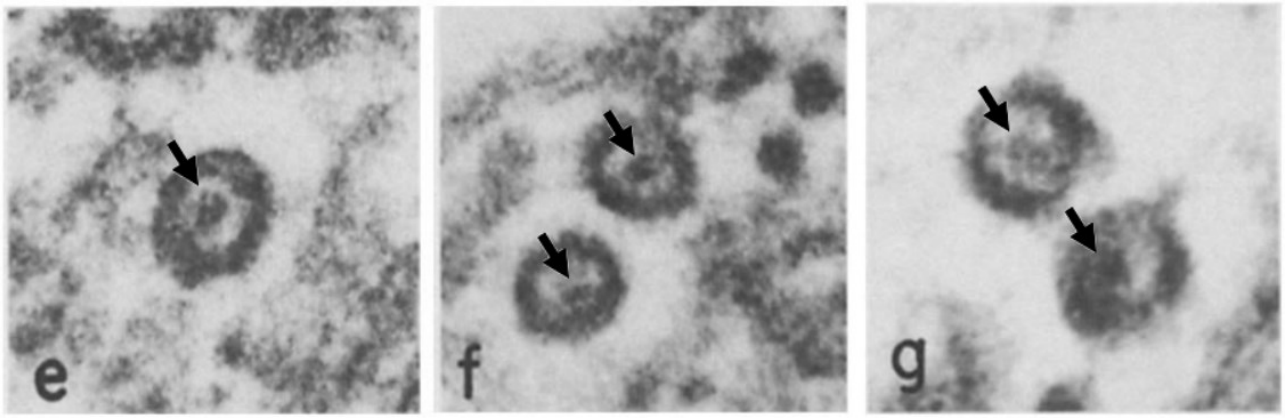

Fig. 4: MTs from frog olfactory neurons containing luminal material. Samples were stained with tannic acid and osmium tetroxide and cut transversely. Arrows are pointing to intraluminal densities. 518,000× magnified. Reprinted from (Burton 1984).

1.2.2. Cryo-EM techniques applied on MIPs in dynamic MTs

New insight was gained with the advent of cryo-EM techniques used with embedding in vitreous ice which enable high contrast even in the absence of any contrasting agent (reviewed by (Al-Amoudi *et al.* 2004)). Garvalov and colleagues examined rat neurons, astrocytes, and stem cells by cryo-EM, and found abundant MT luminal particles with a diameter of approximately 7 nm (Garvalov *et al.* 2006) (**Fig. 5**). Particles were distributed non-homogenously, but their interspacing was in multiples of 4 nm (the length of tubulin monomer repeat in the lattice). The authors suggested that the tubulin acetyltransferase (not yet identified at that time) or deacetylase could account for these densities. Similar particles with a diameter of 6 nm were found in Chinese-hamster ovary cells (Bouchet-Marquis *et al.* 2007) and mouse embryonic fibroblasts (Koning *et al.* 2008). Neurons had higher numbers of particles with shorter distances compared to non-neuronal cells.

1.2.3. α-tubulin acetyltransferase 1

α-tubulin acetyltransferase 1 (αTAT1, not to be confused with anti-tubulin TAT1 antibody) was the first identified MIP (Akella *et al.* 2010, Shida *et al.* 2010). In *C. elegans*, the luminal particles in neurons responsible for touch sensitivity disappear when αTAT1 and its additional paralog are deleted (Topalidou *et al.* 2012). αTAT1 acetylates K40 of α-tubulin, no other substrate is known but they possibly exist, at least in *C. elegans* (Akella *et al.* 2010). K40 is massively acetylated especially in the axoneme (L'Hernault & Rosenbaum 1985, Akella *et al.* 2010), but also in axons (S. Lin *et al.* 2017)

[3] Classification to "dynamic MTs" and "axonemal MTs" is discussed on page 42.

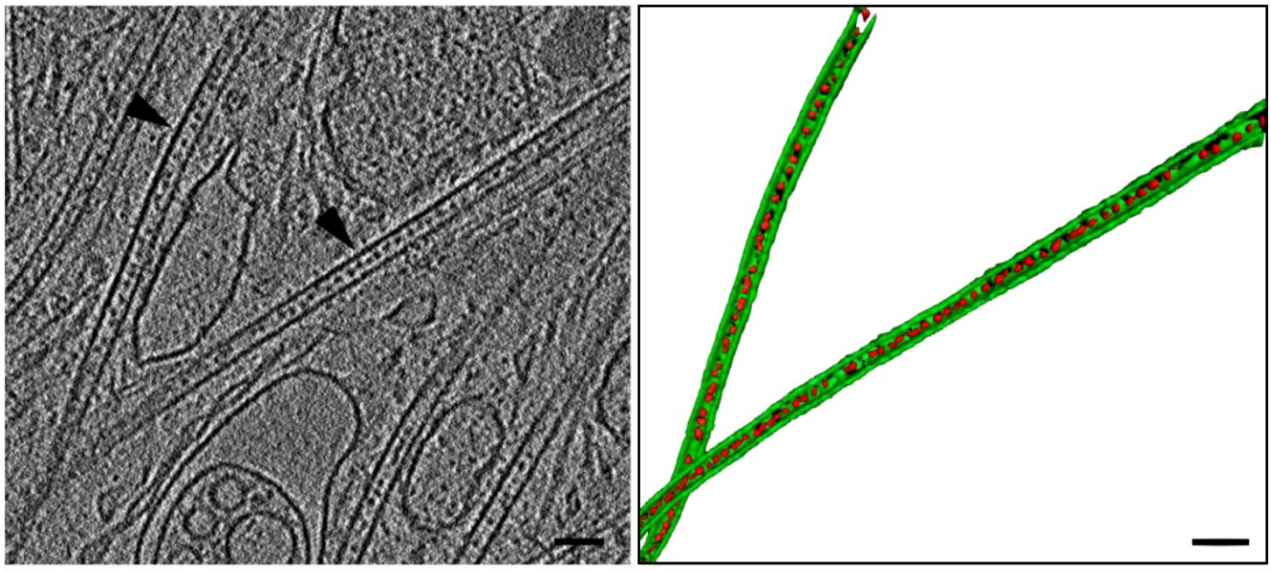

Fig. 5: Luminal particles in MTs of rat neuronal processes. Thin slice with a rat neuronal process was acquired using cryo-ET (left). Two MTs (black arrowheads) were 3D-reconstructed; MT lattice is in green, luminal particles in red (right). Scale bar size not reported, inferred to be 50 nm from other figures in the publication. Reprinted from (Garvalov *et al.* 2006).

and non-neuronal cells (Soppina *et al.* 2012). K40 residue and its acetylation by αTAT1 is conserved among cilia-bearing organisms (Piperno & Fuller 1985, Shida *et al.* 2010), so it is possible to use *Danio rerio* αTAT1 for acetylation of porcine tubulin (Kormendi *et al.* 2012). αTAT1 is however missing in plants and fungi (Akella *et al.* 2010).

There is a disagreement whether αTAT1 is the only K40 acetyltransferase in the human (Shida *et al.* 2010, Kalebic, Sorrentino, *et al.* 2013), or whether another tubulin acetyltransferase enzyme exists (Akella *et al.* 2010). αTAT1 paralog named αTAT2 exists in *C. elegans* but not in the human (Shida *et al.* 2010, Kormendi *et al.* 2012) A knock-out mice strain of αTAT1 gene has no detectable levels of K40 α-tubulin acetylation. Intriguingly, no major phenotype is observed in the strain, although sperm motility is affected (Kalebic, Sorrentino, *et al.* 2013). These arguments are in favour of αTAT1 being the solely α-tubulin K40 acetyltransferase, at least in mammals. Oppositely, the catalytic subunit Elp3 of the elongator complex can acetylate α-tubulin, too (Creppe *et al.* 2009). A definite conclusion is still to be drawn.

K40 acetylation is counteracted by histone deacetylase 6 (HDAC6) (Hubbert *et al.* 2002). Sirtuin 2 is another K40 deacetylase, using both assembled and depolymerized tubulin as the substrate (North *et al.* 2003). HDAC5 was identified as the third tubulin deacetylase (Y. Cho & Cavalli 2012). No data on luminal localization of sirtuin 2 and HDAC5 are available. HDAC6 localization is discussed in chapter 1.2.5.

1.2.3.1. αTAT1 as a MIP

The structure of the N-terminal part of αTAT1 is known (Friedmann *et al.* 2012, Szyk *et al.* 2014); C-terminal residues (from position ~200) are disordered and not required for the enzymatic function (Shida *et al.* 2010, Friedmann *et al.* 2012, Taschner *et al.* 2012). The fold of αTAT1 is similar to histone acetyltransferases and the size is permitting for the enzyme, which is monomeric, to enter the lumen (Kormendi *et al.* 2012). A basic cleft on the surface of αTAT1 harbours the complementary acidic loop with K40 of the α-tubulin (Taschner *et al.* 2012). This residue was previously shown to face inward the MT lumen (Nogales *et al.* 1999, Huilin Li *et al.* 2002, Soppina *et al.* 2012), so it was unclear how does αTAT1 reach its substrate because assembled MTs are strongly preferred over free tubulin dimers as the substrate (Webster & Borisy 1989, Akella *et al.* 2010).

Immediately after the discovery of αTAT1, it was proposed that αTAT1 enters the MT from its open extremities (Akella *et al.* 2010). Acetylation patterns in the axoneme supported this hypothesis – acetylated tubulin was most abundant at one or both ends and vanished in the middle of the MTs. αTAT1 is approximately 3–6 nm in diameter and can hardly fit through the 1.7 nm fenestrations of the tubulin lattice (Nogales *et al.* 1999, Taschner *et al.* 2012) (see **Fig. 2**).

αTAT1 was suggested to enter the lumen in three different ways: 1) Accessing the lumen through the ends (as mentioned above) or lattice defects (Akella *et al.* 2010, Coombes *et al.* 2016). 2) Through co-polymerization with tubulin, mentioned in a review by (Perdiz *et al.* 2011). 3) By accessing the K40-containing loop from the outside in synergy with MT "breathing" (transient openings in the lattice) (Shida *et al.* 2010, Yajima *et al.* 2012). In their detailed work, Coombes and co-authors showed that the end-entry route is the most probable one (Coombes *et al.* 2016). In their hands, αTAT1 diffusion inside the lumen was restricted by a high on-off binding rate to the tubulin lattice. Consequently, acetylation of α-tubulin was predominantly located around entry sites (i. e. the ends and breaks in the lattice). This mode of lumen entry is supported by older works reporting the acetylation patterns in distinct domains on MTs (Webster & Borisy 1989). αTAT1, however, associates with the outer surface as well. Affinity towards the exterior of MTs could facilitate a sufficient entry rate by concentrating αTAT1 nearby the entry points (that is, the terminal openings and lattice defects) (Howes *et al.* 2014).

A very recent article probed the accessibility of MT lumen and visualized the lumen entry in real-time (Nihongaki *et al.* 2021) (previous work relied on post-entry labelling by antibodies (Coombes *et al.* 2016)). The authors reliably show that large proteins like IgG antibodies cannot reach the lumen if the sample is not fixed. To quantitatively test the lumen entry in living cells, they expressed β-tubulin with inserted rapamycin dimerization domain in the middle of the tubulin protein sequence, so that the dimerization domain is facing the lumen. Upon rapamycin treatment, a fluorescent protein fused to a complementary dimerization domain translocates to the MT lumen through the ends and lattice defect sites (**Fig. 6**). Interestingly, co-polymerization with tubulin seems to be the main route of entry, but diffusion-driven entry is observable as well. Once in the lumen, proteins diffuse 0.2–1 μm/min, depending on the concentration of the fluorescent probe. These findings shed new light on the problem of MT lumen entry, but the topic is still mostly unexplored. Ways how MIPs enter the lumen thus remain unclear.

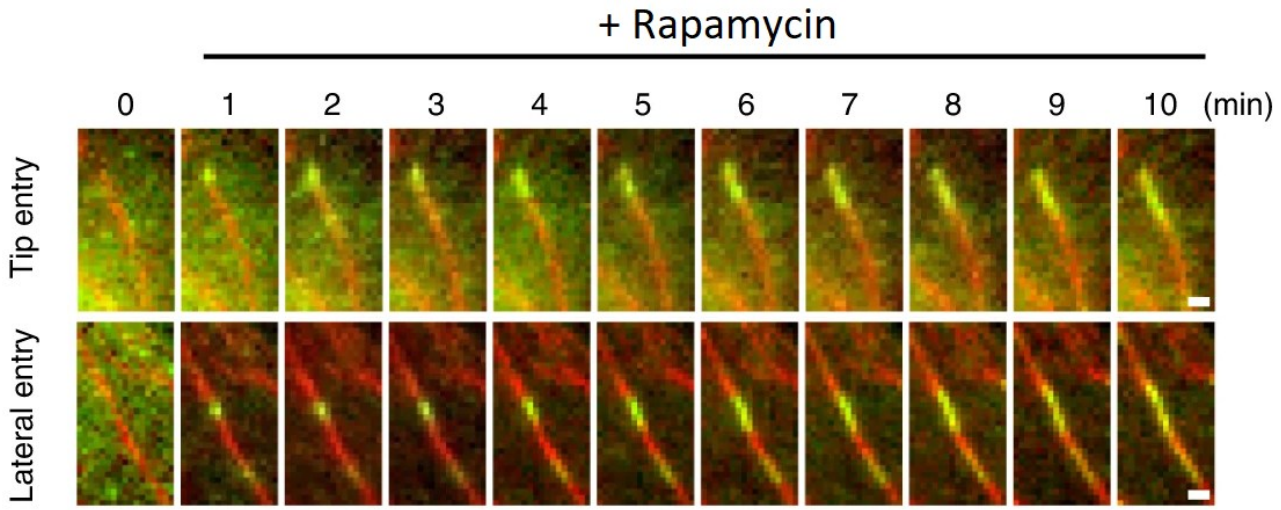

Fig. 6: Direct observation of luminal entry of proteins by diffusion. Cells expressing β-tubulin with inserted dimerization domain facing to the lumen were transfected with yellow fluorescent protein fused to rapamycin dimerization domain. Upon rapamycin treatment, the fluorescent protein signal begins to translocate to the MT, either at the tip (top row), or by lateral entry (bottom row) where the lattice is locally perturbed. This diffusion-driven entry is observable when polymerization of new MTs is halted by nocodazole, and cells are extracted by detergent. Tubulin is in red, YFP signal is in green. Scale bar 1 μm. Reprinted from (Nihongaki *et al.* 2021) and modified.

1.2.4. Microtubule-associated protein 6

Microtubule-associated protein 6 (MAP6) was initially identified as a calmodulin-binding protein associated with cold-stable MTs in neuronal tissues, as reviewed in (Bosc *et al.* 2003). Its original name was STOP (Stable Tubule-Only Polypeptide) because it protects MTs from the cold- and nocodazole-induced depolymerization (Guillaud *et al.* 1998, Andrieux *et al.* 2002). Three isoforms are

generated from a single gene by alternative splicing (Bosc *et al.* 2003). MAP6 is highly expressed in the human lungs and brain; testis, heart, muscles, and kidneys show lower MAP6 expression (Aguezzoul *et al.* 2003). The pivotal role of MAP6 in neural tissues is pronounced in MAP6-deficient mice, which evinces schizophrenic behaviour, albeit lacking any morphological or somatic impairment (Andrieux *et al.* 2002). Unsurprisingly, MAP6 mutations are linked to schizophrenia in humans, too (Shimizu *et al.* 2006).

The propensity of MAP6 to bind MTs and protect them from cold-induced depolymerization stems from its structure (Lefèvre *et al.* 2013). Upon cooling, MAP6 progressively associates with MTs and prevents their depolymerization (Delphin *et al.* 2012). This is caused by an increase of affinity of MAP6 towards MTs in lower temperatures, probably by cold-induced structural changes (Delphin *et al.* 2012). Such behaviour implies that MAP6 might have low-structured regions, which is in agreement with its tendency to form aggregates in amyotrophic lateral sclerosis patients (Letournel *et al.* 2003).

Surprisingly, MAP6 is also a MIP. A recent work (Cuveillier *et al.* 2020) reports that MAP6 knockout neurons possess luminal particles in 27 % of MTs, compared to 64 % of wild-type cells. The authors then co-polymerized MAP6 with tubulin and many luminal densities attributed to MAP6 appeared (**Fig. 7**). When MAP6 is added to already preformed MTs, no inner particles are observable. Furthermore, MAP6 increases the frequency of catastrophes, but it slows down depolymerization at the same time. Lastly, MAP6 substantially changes the lattice of the MT when bound inside – it induces a twist of the MT and creates apertures. Hence, the authors suggest that MAP6 acts as a stabilizing MAP along the lattice, as a dynamicity modulator at the ends of the MTs, and as a MIP inside the lumen, entering by co-polymerization. Further work will be needed to confirm this hypothesis.

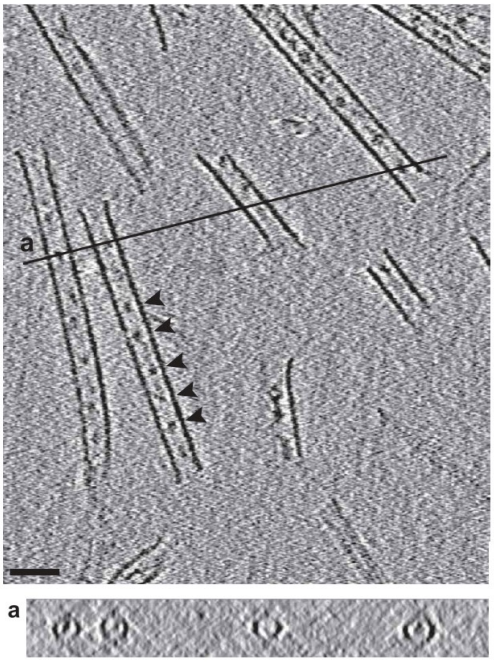

Fig. 7: MTs co-polymerized with MAP6, visualized by cryo-ET. A transverse section view along the black line is shown below the main figure with visible luminal material. Arrowheads mark the densities inside one MT. Reprinted from (Cuveillier *et al.* 2020).

1.2.5. Other and putative MIPs of dynamic MTs

Other proteins besides αTAT1 and MAP6 are suggested to be MIPs in dynamic MTs. HDAC6 was first thought to deacetylate only assembled MTs (Hubbert *et al.* 2002). Others (Miyake *et al.* 2016) claimed that HDAC6 prefers free tubulin dimers as the substrate but can enter the lumen of MTs as well. HDAC6 has no preference for ends and deacetylates MTs stochastically along their whole length, oppositely to αTAT1 (Coombes *et al.* 2016). Another work suggests a third mode of action, and that HDAC6 strongly prefers free tubulin with no activity towards MTs (Skultetyova *et al.* 2017). A definitive answer is not available yet. The molecular size of HDCA6 (~130 kDa compared to ~47 kDa mass of αTAT1) is not in favour of luminal entry, though.

Tau protein is well-known for the tendency to form plaques in neural cells leading to Alzheimer's disease (reviewed in (Ittner & Götz 2011)). Tau lacks ordered tertiary structure (Popov *et al.* 2019). Although not being a true MIP, tau is suggested to protrude to the lumen from the outside through the fenestrations and compete with paclitaxel at its binding site (Kar *et al.* 2003). Inaba and colleagues (Inaba *et al.* 2018) designed a tau-derived peptide that localizes to the lumen of MTs, revealed by gold bead-labelling and EM. Contrary to these claims, other works did not find any influence between tau and paclitaxel site-binding drugs (Kadavath *et al.* 2015) or do not report on tau protrusion inside MTs when resolving the structure of the tau-tubulin interface (Kadavath *et al.* 2018). Hence, tau membership in the MIP team remains elusive.

Recently, an unexpected phenomenon of actin filament presence in the lumen of MTs was noted (Paul *et al.* 2020). Actin appears inside MTs only when treatment with kinesore, a kinesin-targeting drug, is applied to cells. This drug induces MTs to bundle, loop, and create projections at the cell periphery, where the actin filaments are found in the lumen of MTs. The relevance of this discovery is unclear since no details pertaining to the route of entry and the role of kinesore are known.

1.3. MIPs in axonemal MTs

Similarly to dynamic MTs, early axonemal MIPs studies utilize contrasting techniques and transmission EM of thin sections. One of the first reports on MIPs in the axoneme (Stanley *et al.* 1972) describes a development process of *Drosophila melanogaster* spermatids. Authors note that during the maturation, MTs in the axoneme accumulate dense luminal material of unknown composition and function. A similar pattern was also published more recently (Ghosh-Roy *et al.* 2004), **Fig. 8**. Material-containing axonemal MTs are also present in other species, e. g. in spiders (Dallai *et al.* 1995), humans (Afzelius *et al.* 1995), and *Trypanosoma* (Vaughan *et al.* 2006). The resolution obtained in these studies (using transmission EM performed on samples usually stained by heavy metals or tannic acid, fixed, and embedded in resin) can hardly yield any atomic details, though. Sub-nanometre resolution is needed to resolve secondary structures of proteins, which can facilitate protein identification (Ichikawa *et al.* 2017).

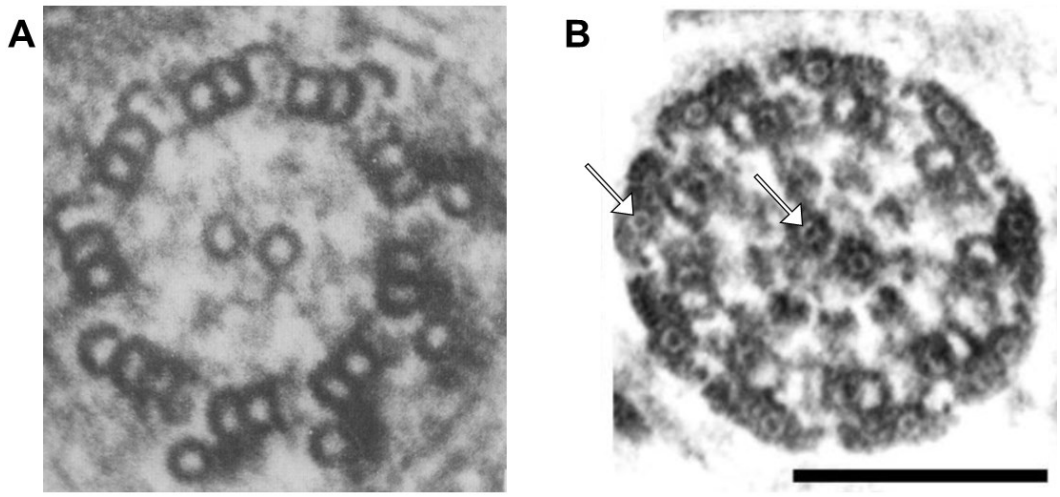

Fig. 8: Axoneme of *Drosophila melanogaster* spermatids accumulates luminal material in the lumen of MTs. A: Early stage of spermatid development. Axoneme on a transverse cut shows no luminal material in MTs. **B:** Late stage of spermatid development. All MTs now contain dense luminal material as seen on a transverse cut through the axoneme. Arrows are pointing to two of the material-containing MTs. **A:** 226,000× magnified, reprinted from (Stanley *et al.* 1972). **B:** Scale bar 200 nm, reprinted from (Ghosh-Roy *et al.* 2004).

1.3.1. Cryo-EM techniques applied to axonemal MIPs

Progress in revealing the architecture of the axoneme was immensely boosted by cryo-EM techniques. In cryo-electron tomography (cryo-ET), the sample is rapidly frozen in liquid ethane, so that water contained in the biological sample vitrifies into amorphous ice. Thin samples are then imaged

by an EM in a series of tilts. 3D reconstruction or tomogram is then calculated from individual images taken in different angles; reviewed by (Wagner *et al.* 2017). A complementary approach, called single particle cryo-EM, utilizes a classification of individual objects from EM pictures into groups by similarity (i. e. particles with similar structure and orientation). A complex 3D model is then assembled if enough particles in all rotations are captured. Summarized e. g. in (Cheng *et al.* 2015). Both techniques revolutionized structural biology and the research on MIPs.

The first work to show MIPs (and coined the term) in the axoneme by cryo-ET was performed on sea urchin sperm and flagella of *Chlamydomonas reinhardtii* (Nicastro *et al.* 2006); this work achieved an overall resolution of ~4 nm. This value is close to the resolution limit needed to reveal MIPs, because one previous work by the same group, also performed on sea urchin sperm, did not reveal any MIPs in the axoneme (Nicastro *et al.* 2005). More detailed structures followed both from *C. reinhardtii* or *Tetrahymena thermophila* (**Fig. 9**) (Pigino *et al.* 2012, Ichikawa *et al.* 2017, Ma *et al.* 2019). No high-resolution structure from the human is available yet. A comparison of the three most common model organisms in axonemal research – *C. reinhardtii*, *T. thermophila*, and sea urchin – showed substantial but still incomplete conservation of luminal structures in MTDs (Pigino *et al.* 2012).

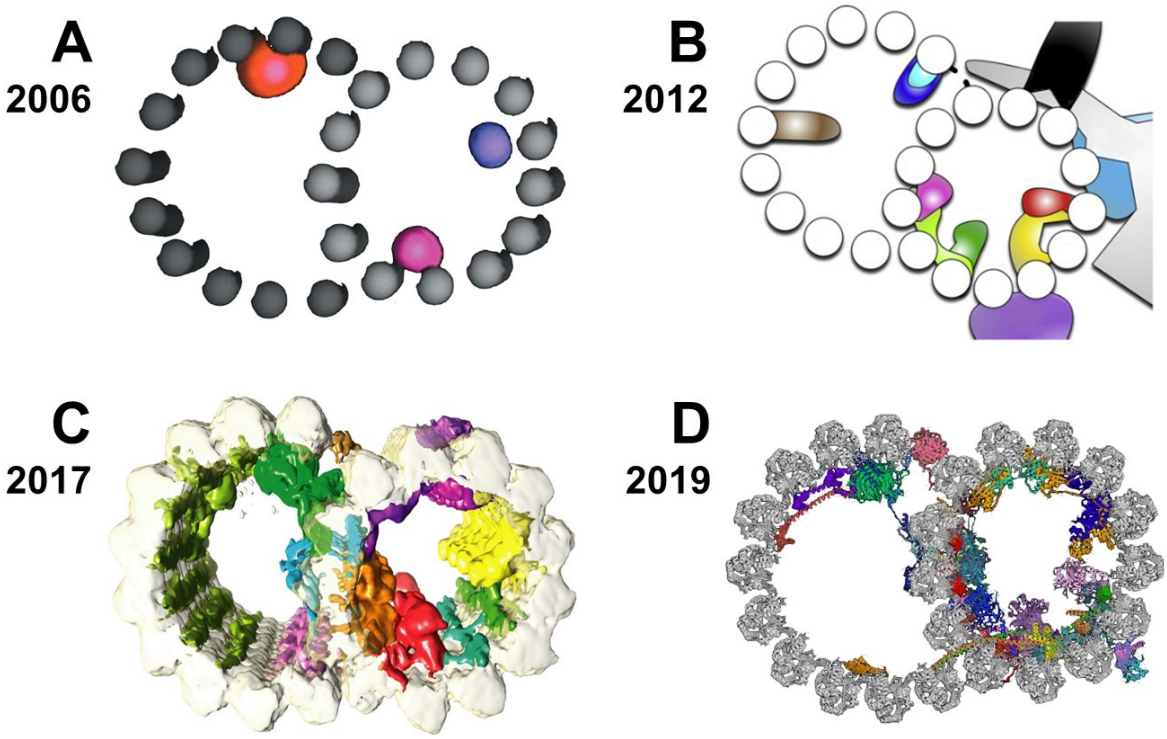

Fig. 9: Progress in structures of the axoneme and contained MIPs. Four depictions of one MTD of the axoneme of *Chlamydomonas reinhardtii* (**A**, **B**, **D**) or *Tetrahymena thermophila* (**C**) from four publications are compared. The year of publishing is stated. MTDs are viewed on transverse sections with various MIPs in colour; **A** and **B** are schemas, **C** and **D** are three-dimensional reconstructions made by single particle cryo-EM. The resolution reached is 4, 3.4, 0.57, and 0.35 nm respectively for structures **A**–**D**. Note that the B-tubule in structure **A** is drawn with 11 protofilaments. Reprinted from (Nicastro *et al.* 2006, Pigino *et al.* 2012, Ichikawa *et al.* 2017, Ma *et al.* 2019) and modified.

The most recent and most detailed structure of the MTDs comes from the flagellum of *C. reinhardtii* (Ma *et al.* 2019). This unprecedently detailed model reached atomic resolution by single particle cryo-EM and identified 33 MIPs (**Fig. 9 D**). MIPs decorate nearly all the inner surface of the MTD, being more abundant in the A-tubule than the B-tubule. MIPs have different repeat lengths (8, 16, or 48 nm), that is, what is the distance of the protein on the axoneme between its repeated occurrence. Repeat lengths of 24 and 96 nm are exclusive to outer proteins. The overall repeat length of the axoneme is now believed to be 96 nm and is imposed by two outer proteins acting as "molecular rulers" (Oda, Yanagisawa, Kamiya, *et al.* 2014). Interestingly, when these ruler proteins are artificially extended by insertion of one extra domain, the overall repeat length of the axoneme

increases accordingly. MIPs appear to have a separate overall repeat length of 48 nm (Ma *et al.* 2019). The repeat lengths are dictated by the size of the tubulin dimer, which is 8 nm (Nogales *et al.* 1995).

Other important conclusions stem from the work of (Ma *et al.* 2019). First, MIPs are observed to protrude through the lattice fenestrations either from the A-tubule towards the B-tubule lumen or from the lumen to the outside, where contacts to e. g. outer dynein arms are made. This penetrating through tubulin lattice was also reported in earlier structures (Ichikawa *et al.* 2017). MIPs thus facilitate the inside-outside communication on MTs, which might have important implications for the K40 acetylation readout. Two MIPs were indeed shown to bind to the K40 loop of α-tubulin. Second, new light was shed on the roles of MIPs in the axoneme. Their predominant function is to reinforce the MT they are contained in against the mechanical stress generated by flagellum bending (Owa *et al.* 2019). A previous report discovered that deletion of MIP protein RIB72 in *T. thermophila* leads to slower swimming speed and abnormal beating patterns (Stoddard *et al.* 2018). There is little to no data on axonemal MIPs lumen entry. Ma and colleagues speculate that MIPs co-assemble with the whole axoneme in a precisely organized manner (Ma *et al.* 2019). The possible turnover of axonemal MIPs (if any exists) remains unexplored.

1.3.2. TAILS complex in sperm cells

MIPs in the axoneme can associate with the tubulin wall in a longitudinal manner, copying the direction of protofilaments (Nicastro *et al.* 2011). An alternative mode of MIPs binding is a spiral pattern created by adhering to laterally neighbouring tubulin dimers. This pattern was first observed by cryo-ET in the distal part of the axoneme of human sperm cells, and the complex of MIPs was named TAILS (Tail Axoneme Intra-Lumenal Spiral) (Zabeo *et al.* 2018). A 3D reconstruction and a schematic model are in **Fig. 10**. A cryo-EM image of MTs containing TAILS is in **Fig. 11**.

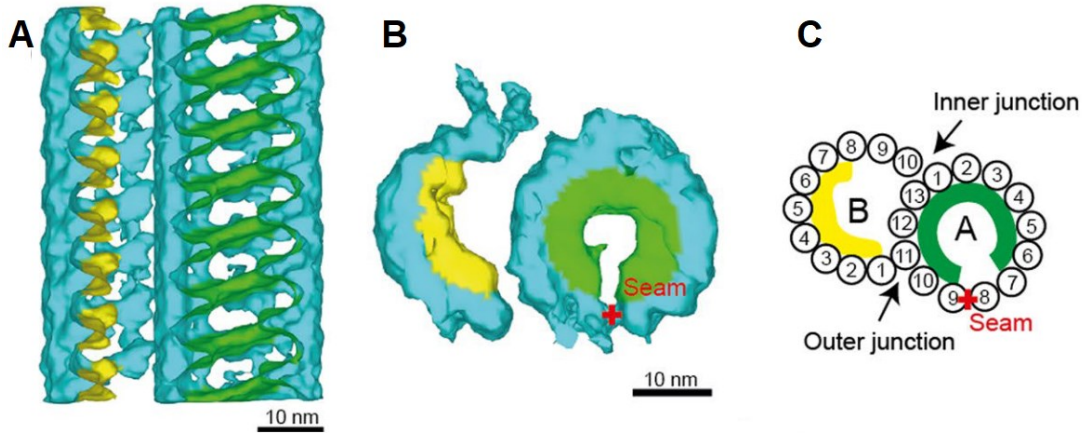

Fig. 10: TAILS complex in the human sperm cell axoneme. A: Longitudinal reconstruction of a MTD (blue) containing the left-handed spiral of TAILS with 8 nm pitch in the A-tubule (green) and TAILS-like structure in the B-tubule. **B:** A top view on a MTD containing TAILS (plus end facing the reader). The position of the seam in the A-tubule is indicated. **C:** A scheme of a MTD containing TAILS. The TAILS spiral (green) is interrupted at the seam in the A-tubule. Reprinted from (Zabeo *et al.* 2018).

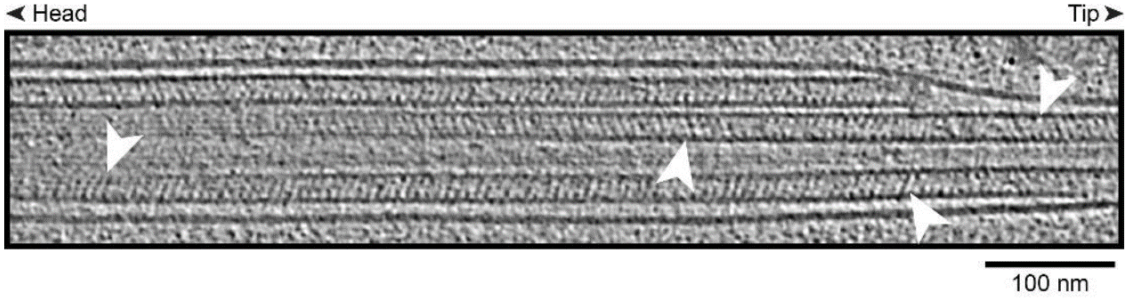

Fig. 11: TAILS appears as regular oblique striation on MTs. A cryo-EM picture of a human sperm cell near the flagellum tip. Arrowheads are pointing to MTs containing TAILS. Direction towards the head and the tip are denoted. Reprinted from (Zabeo 2021).

TAILS is present in both A-tubule (fully-assembled spiral) and B-tubule (as a TAILS-like structure). The complex spans from the most distal part of the end-piece (also known as the tip) where MTDs are split into singlet MTs (Zabeo *et al.* 2019) to the zone where A- and B-tubule are merged into MTDs. TAILS is terminated approximately 3 μm from the tip (Zabeo *et al.* 2018). TAILS also fills the central pair singlet MTs, up to 10 μm from the tip. The composition of this complex, atomic structure, way of assembly, and function are unknown. The speculation is that TAILS can reinforce the lattice, suppress the dynamics of the plus end of axonemal MTs (since there is no intraflagellar transport in sperm cells which is needed to replenish dissociated GDP tubulin by fresh GTP tubulin (San Agustin *et al.* 2015)), or induce a tip-specific structure of MT lattice to define a distinct binding surface for alleged MIPs and MAPs (Zabeo 2021).

Unpublished preliminary results (Zabeo 2021) show the evolutionary distribution of TAILS: It is present in the bull, chicken, and frog *Xenopus tropicalis*. Also sperm cells of pigs and horses contain TAILS (Leung *et al.* 2021), but the complex is, however, missing in *C. reinhardtii* (Jordan *et al.* 2018), *T. brucei* (Zabeo 2021), and surprisingly in mice as well (Leung *et al.* 2021). A MIP similar to TAILS was observed in the lumen of MTs in the basal body (a structure continuous with the axoneme, anchoring it in the cytoplasm) of bovine tracheal cilia (Greenan *et al.* 2020).

The identities of proteins constituting the TAILS complex are not known, although doublecortin domain-containing 2C protein (DCDC2C) is a good candidate (Zabeo 2021). This understudied protein was reported to localize solely to the tip in human sperm cells (Jumeau *et al.* 2017). The mouse DCDC2C knock-out strain shows significant phenotype only for skeletal defects (as published by the International Mouse Phenotyping Consortium, www.mousephenotype.org/data/genes/MGI:1915761). No other data on the structure or function of DCDC2C are available. Other members of the doublecortin family act as MT stabilizers and enhancers of nucleation (Moores *et al.* 2004). A related protein DCDC2A was linked to hear loss when mutated in humans (Grati *et al.* 2015). DCDC2A localizes to kinocilia of sensory hair cells and along the whole length of primary cilia.

2. Aims

This thesis aimed to address the knowledge gap of microtubule inner proteins (MIPs) identity, particularly in the dynamic structurally nonspecialized microtubules of human cells[4], and the Tail Axoneme Intra-Lumenal Spiral (TAILS) complex in vertebrate sperm cells.

As for the dynamic MTs which are part of the general cytoplasmic cytoskeletal network, not much is known about MIPs inside since cryo-EM data cannot be enhanced by averaging of precisely repeating patterns. This thesis strived in its first part to generate a set of biochemical and visualization tools and methods allowing the indirect study of MIPs in dynamic MTs.

A handful of proteins has been identified as MIPs in the axonemes of various model organisms, especially protists like *Chlamydomonas reinhardtii* (Ma *et al.* 2019) or *Tetrahymena thermophila* (Stoddard *et al.* 2018). The second part of this thesis contributed to endeavours to identify the constituent of the newly described TAILS complex.

Specifically, the list of goals was following:

1. Obtain lists of new candidate proteins for MIPs in dynamic MTs using two independent approaches followed by mass spectrometry (MS) analysis, i. e. proximity-dependent biotin identification (BioID) by a promiscuous biotin ligase, and isolation of microtubules from cultured human cells.
    1.1 Prepare a set of cell lines stably expressing fusion proteins with the biotin ligase and isolate biotinylated proteins, enriched in prospective MIPs.
    1.2 Optimize the method of direct MTs isolation from cultured mammalian cells.
    1.3 Generate proteomes from both approaches, searching for MIPs candidate proteins.
2. Obtain a list of candidate proteins for the TAILS complex in sperm cells by immunofluorescent (IF) labelling and subsequent FACS (fluorescent-activated cell sorting) and MS analysis. Optimize the methods of IF labelling and FACS applied to bull sperm cells.

[4] Classification to "dynamic MTs" and "Axonemal MTs" is discussed on page 42.

3. Materials & methods

3.1. Materials

3.1.1. Buffers & media

PBS (Phosphate buffer saline)
137 mmol/l NaCl (Penta, s. r. o., Prague, Czech Republic)
2.7 mmol/l KCl (Lachema, s. r. o., Brno, Czech Republic)
10 mmol/l Na_2HPO_4 (Lachema, s. r. o., Brno, Czech Republic)
1.8 mmol/l KH_2PO_4 (Penta, s. r. o., Prague, Czech Republic)
pH adjusted to 7.4 by NaOH or HCl.

HBSS (Hank's balanced salt solution)
137 mmol/l NaCl (Penta, s. r. o., Prague, Czech Republic)
5 mmol/l KCl (Lachema, s. r. o., Brno, Czech Republic)
1.1 mmol/l $Na_2HPO_4 \cdot 12\ H_2O$ (Lachema, s. r. o., Brno, Czech Republic)
0.4 mmol/l KH_2PO_4 (Penta, s. r. o., Prague, Czech Republic)
5.5 mmol/l glucose (Merck KGaA, Darmstadt, Germany)
4 mmol/l $NaHCO_3$ (Lachema, s. r. o., Brno, Czech Republic)
pH adjusted to 6.9 by NaOH or HCl. Autoclaved.

MSB (microtubule-stabilizing buffer)
To be dissolved in HBSS.
20 mmol/l MES (2-(*N*-morpholino)ethanesulfonic acid) (Merck KGaA, Darmstadt, Germany)
2 mmol/l EGTA (ethylene glycol-bis(β-aminoethyl ether)-*N*,*N*,*N*′,*N*′-tetraacetic acid) (Merck KGaA, Darmstadt, Germany)
2 mmol/l $MgCl_2$ (Penta, s. r. o., Prague, Czech Republic)
4 % (w/V) PEG 6000 (polyethylene glycol, average molar mass 6000 g/mol) (Merck KGaA, Darmstadt, Germany)
For fixation of cells prior to IF labelling, paraformaldehyde (PFA) was dissolved in MSB to reach 3 % (w/V). (Merck KGaA, Darmstadt, Germany)

LB (lysogeny broth)
5 g bacto tryptone (BD, Franklin Lakes, New Jersey, USA)
2.5 g yeast extract (Applichem, Council Bluffs, Iowa, USA)
5 g NaCl (Penta, s. r. o., Prague, Czech Republic)
Filled to 0.5 l with dH_2O (distilled water). Autoclaved.
Agar PDs (Petri dishes) were prepared from ready-to-dissolve LB broth with agar (Lennox) (Merck KGaA, Darmstadt, Germany) with 100 µg/ml ampicillin. (Merck KGaA, Darmstadt, Germany).

SOB (Super optimal broth)
2 % (w/V) tryptone/peptone (Thermo Fisher Scientific, Waltham, Massachusetts, USA)
0.5 % (w/V) yeast extract (Applichem, Council Bluffs, Iowa, USA)
10 mmol/l NaCl (Penta, s. r. o., Prague, Czech Republic)
2.5 mmol/l KCl (Lachema, s. r. o., Brno, Czech Republic)
Autoclaved.
Added 10 mmol/l $MgCl_2$ (as sterile-filtered solution). (Penta, s. r. o., Prague, Czech Republic)

TB (transformation buffer)
10 mmol/l PIPES (piperazine-N,N′-bis(2-ethanesulfonic acid)) (Merck KGaA, Darmstadt, Germany)
15 mmol/l $CaCl_2$ (Lachema, s. r. o., Brno, Czech Republic)
250 mmol/l KCl (Lachema, s. r. o., Brno, Czech Republic)

pH adjusted to 6.7 by KOH or HCl. Autoclaved, supplied with sterile-filtered $MnCl_2$ to reach 55 mmol/l. (Carl Roth GmbH, Karlsruhe, Germany)

10× TAE buffer (tris, acetic acid, EDTA)
48.4 g tris base (tris(hydroxymethyl)aminomethane) (Merck KGaA, Darmstadt, Germany)
11.4 ml acetic acid (glacial) (Penta, s. r. o., Prague, Czech Republic)
3.7 g EDTA (ethylenediaminetetraacetic acid) (Lach-ner, Neratovice, Czech Republic)
Filled with dH_2O to 1 l. Diluted 10 times for use.

4× Laemmli denaturing buffer
62.5 mmol/l tris (Merck KGaA, Darmstadt, Germany)
2 % (w/V) SDS (sodium dodecyl sulphate) (Merck KGaA, Darmstadt, Germany)
10 % (w/V) glycerol (Penta, s. r. o., Prague, Czech Republic)
5 % (V/V) mercaptoethanol (Merck KGaA, Darmstadt, Germany)
0.02 % (w/V) bromophenol blue (Merck KGaA, Darmstadt, Germany)
Diluted 4 times before use.

5% polyacrylamide gel (stacking)
125 mmol/l tris (as a solution, pH 6.8) (Merck KGaA, Darmstadt, Germany)
5 % (V/V) acrylamide/bis-acrylamide 30% solution (Merck KGaA, Darmstadt, Germany)
1 % (w/V) SDS (Merck KGaA, Darmstadt, Germany)
1% (w/V) ammonium persulphate (Merck KGaA, Darmstadt, Germany)
0.04 % (V/V) TEMED (tetramethylethylenediamine) (Merck KGaA, Darmstadt, Germany)
dH_2O filled to 4 ml.

8% polyacrylamide gel (running)
375 mmol/l tris (as a solution, pH 8.8) (Merck KGaA, Darmstadt, Germany)
27 % (V/V) acrylamide/bis-acrylamide 30% solution (Merck KGaA, Darmstadt, Germany)
1 % (w/V) SDS (Merck KGaA, Darmstadt, Germany)
1% (w/V) ammonium persulphate (Merck KGaA, Darmstadt, Germany)
0.04 % (V/V) TEMED (Merck KGaA, Darmstadt, Germany)
dH_2O filled to 10 ml.

PAGE (polyacrylamide gel electrophoresis) running buffer
25 mmol/l tris (Merck KGaA, Darmstadt, Germany)
192 mmol/l glycine (Penta, s. r. o., Prague, Czech Republic)
0.1 % (w/V) SDS (Merck KGaA, Darmstadt, Germany)
Filtered.

Blotting buffer
25 mmol/l tris (Merck KGaA, Darmstadt, Germany)
192 mmol/l glycine (Penta, s. r. o., Prague, Czech Republic)
20 % (V/V) methanol (Penta, s. r. o., Prague, Czech Republic)
Filtered, used prechilled to 4 °C.

TBST (tris-buffered saline + tween)
10 mmol/l tris (Merck KGaA, Darmstadt, Germany)
150 mmol/l NaCl (Penta, s. r. o., Prague, Czech Republic)
0.05 % Tween 20 (V/V) (Merck KGaA, Darmstadt, Germany)
pH adjusted to 7.4 by NaOH or HCl.

HMP buffer / BRB80 (high-molarity PIPES / Brinkley reassembly buffer)
HMP and BRB80 buffers are used in various scaled dilutions. Molarity is denoted as a number, e. g. HMP400 means 400 mmol/l HMP. BRB80 is used instead of HMP80 by custom.
For HMP1000 (lower molarities are prepared by diluting HMP1000 in dH_2O):
1 mol/l PIPES (piperazine-N,N′-bis(2-ethanesulfonic acid)) (Merck KGaA, Darmstadt, Germany)
10 mmol/l $MgCl_2$ (Penta, s. r. o., Prague, Czech Republic)

20 mmol/l EGTA (Merck KGaA, Darmstadt, Germany)
pH adjusted to 6.9 with KOH or HCl.

Lysis buffer for isolation of intact MTs
For 200 µl:
1.5 % (V/V) NP-40 detergent (Merck KGaA, Darmstadt, Germany)
10 µmol/l paclitaxel (Merck KGaA, Darmstadt, Germany)
10 mmol/l ATP (Merck KGaA, Darmstadt, Germany)
125 µmol/l GTP (Thermo Fisher Scientific, Waltham, Massachusetts, USA)
15 µmol/l cytochalasin D (Thermo Fisher Scientific, Waltham, Massachusetts, USA)
1× cOmplete protease inhibitors (Roche, Basel, Switzerland)
5 µl DNase I (Merck KGaA, Darmstadt, Germany)
Filled to 200 µl with HMP250 (final molarity ~HMP200).
Prepared fresh from components before use.

Lysis buffer for isolation of MTs polymerized in cell lysate
0.5 % (V/V) Tween 20 detergent
10 mmol/l ATP (Merck KGaA, Darmstadt, Germany)
1× cOmplete protease inhibitors (Roche, Basel, Switzerland)
5 µl DNase (Merck KGaA, Darmstadt, Germany)
Filled to 200 µl with BRB80.
Prepared fresh from components before use.

Cell culture medium
DMEM (Dulbecco's Modified Eagle Medium) with GlutaMAX and 4.5 g/l glucose (Thermo Fisher Scientific, Waltham, Massachusetts, USA)
1× penicillin-streptomycin solution (Biowest, Riverside, Missouri, USA)
10 % (V/V) calf bovine serum (Thermo Fisher Scientific, Waltham, Massachusetts, USA)

3.1.2. Antibodies

Antibodies used in this thesis are listed in **Table 1** and **Table 2**. TAT1 antibody is not to be confused with αTAT1 α-tubulin acetyltransferase.

Table 1: Primary antibodies used in this thesis.

Name	Target protein	Type	Dilution Usage	Source
TAT1	α-tubulin	Mouse monoclonal	1:25 IF labelling	(Woods et al. 1989), V. Varga (IMG, Prague, Czech Republic)
DCDC2C	DCDC2C	Rabbit polyclonal	1:150 IF labelling	Abcam, Cambridge, United Kingdom
YL1/2	α-tubulin	Rat monoclonal	1:50 immunoprecipitation	

Table 2: Secondary antibodies and protein labels used in this thesis. HRP, horseradish peroxidase.

Name	Conjugated moiety	Type	Dilution Usage	Manufacturer
DAM DL488	DyLight 488	Donkey anti-mouse	1:400 IF labelling	Jackson ImmunoResearch Laboratories Inc, West Grove, Pennsylvania, USA
GAR cy3	Cy3	Goat anti-rabbit	1:400 IF labelling	
Streptavidin-HRP	HRP	–	1:1000 Western blot	Thermo Fisher Scientific, Waltham, Massachusetts, USA

3.1.3. Primers

Primers were acquired from Merck KGaA, Darmstadt, Germany. Used primers are listed in **Table 3**. Primers were shipped as a lyophilized powder, dissolved in PCR (polymerase chain reaction) grade dH_2O to 100 µmol/l stock aliquots, and stored at −20 °C.

Table 3: DNA primers used in this thesis. GFP, green fluorescent protein.

Name	Sequence (5'→3')
ATAT1_F_KpnI	TTAGGTACCAATGGAGTTCCCGTTCGATG
ATAT1_Iso4_R_XhoI	TTCTCGAGTTAGTATCGACTCTCCTCAGAG
miniTurbo_PmeI_F	AAGTTTAAACATGGGCAAGCCCATCCCCAACCC
miniTurbo_multi_R	AAGGATCCTTAAACTCGAGTGTACATGGTAC-CGTCCAGGGTCAGGCGCTCCAG
GFP mTurbo_KpnI_F	AAGGTACCATGGTGAGCAAGGGCGAGGAG
GFP mTurbo_R	CTTGTACAGCTCGTCCATGCC
MAP6iso1_fwd_BsrGI	AATGTACAATGGCGTGGCCGTGCATCAC
MAP6iso1_rev_XhoI	ACCTCGAGTCAAGGGGAGCTCTCAATGT
MAP4_BsrGI_F	CTTGTACACAATGGCTGACCTCAGTCTTGCAG
MAP4_Xho_R	AGCTCGAGGATGCTTGTCTCCTGGATCTGG
GFP_tubulin_F	ATGGTACCGCCACCATGGTGAGCAAGGGCGAG
GFP_tubulin_R	CCGGTGGATCCTTAGTATTCCTCTCCTTCTTCC

3.1.4. Plasmids

A list of plasmids used directly to generate results included in the thesis is in **Table 4**. Other plasmids used for cloning but not directly for any results presented here are listed in **Table 5**. Maps of vectors from **Table 4** are attached as Supplement 1.

Table 4: Plasmids used in this thesis and reported in the Results section.

Name	Structure
miniTurbo-GFP	pGFT3-V5-miniTurbo-GFP
GFP-αTAT1	pGFT3-GFP-αTAT1_isoform4
αTAT1-GFP	pGFT3-αTAT1_isoform4-linker-GFP
miniTurbo-GFP-αTAT1	pGFT3-V5-miniTurbo-GFP-αTAT1_isoform4
GFP-MAP6	pGFT3-GFP-MAP6_rat
MAP6-GFP	pGFT3-MAP6_rat-linker-GFP
miniTurbo-GFP-MAP6	pGFT3-V5-miniTurbo-GFP-MAP6_rat
MAP6-miniTurbo-GFP	pGFT3-MAP6_rat-linker-V5-miniTurbo-GFP
miniTurbo-GFP-MAP4	pGFT3-V5-miniTurbo-GFP-MAP4
GFP-α-tubulin	pGFT3-GFP-α-tubulin

Table 5: Other plasmids used for cloning.

Name/structure	Source	Used for
pGFT3-BioID2-HA	Vladimír Varga, Institute of Molecular Genetics, Prague, Czech Republic	Backbone for vectors with Flp-in system
pOG44	Vladimír Varga, Institute of Molecular Genetics, Prague, Czech Republic	FLP recombinase bearing plasmid for stable RPE cell lines
pEGFP-N1-MAP6	Annie Andrieaux, Grenoble Institute of Neuroscience, France	Source of MAP6 gene
pCDNA3-V5-mini-Turbo-NES	Addgene, Watertown, Massachusetts, USA; plasmid #107170	Source of miniTurbo gene

3.1.5. Cells

Bull sperm acquisition and storage

Frozen bull sperm in plastic straws was gifted by Ondřej Šimoník (Group of Reproductive Biology, Czech Academy of Science) and bull insemination station in Hradištko pod Medníkem (Natural Ltd., Czech Republic). Straws were stored in liquid nitrogen upon acquisition. Thawing was done in a warm water bath.

Bacterial cell lines

DH5α transformation-competent *E. coli* strain was prepared in our laboratory from naïve DH5α cells.

Human cell lines

hTERT RPE-1 cells (human telomerase reverse transcriptase-immortalised retina pigment epithelium) with TET-ON inducible expression system and integrated Flp-in (Flippase-in) FRT (flippase recognition target) sequence were generously gifted by V. Varga (IMG, Prague, Czech Republic).

U2OS cell line (human osteosarcoma epithelium) was originally acquired from the ATCC collection (Manassas, Virginia, USA).

3.2. Methods

3.2.1. MIPs in dynamic MTs

3.2.1.1. Preparation of transformation-competent DH5α bacterial cells

Cells were prepared as described in (Inoue *et al.* 1990). Single colony of naïve DH5α *E. coli* was inoculated from LB agar PD to 3 ml of SOB medium and grown overnight at 37 °C. 1 ml of suspension was then inoculated into 240 ml of SOB medium and grown at 24 °C while shaken vigorously. When optical density of 0.6 at 600 nm was reached, the culture was transferred on ice and cooled for 10 min. The suspension was spun down at 2500 g, 4 °C, 10 min. The pellet was resuspended in 80 ml of ice-cold TB on ice. Spun down again after 10 min on ice. The pellet was resuspended in 20 ml of ice-cold TB, supplied with 7 ml of DMSO (dimethyl sulfoxide; 7 % V/V final concentration), and mixed well. Cells were aliquoted into prechilled microtubes on ice and frozen in liquid nitrogen.

3.2.1.2. Molecular cloning

MAP6 gene source was pEGFP-N1-MAP6 vector, αTAT1 gene was cloned from custom cDNA library of U2OS cells (mRNA of αTAT1 gene for primers design number NM_024909 in GenBank database), miniTurbo gene was cloned from pCDNA3-V5-miniTurbo-NES vector.

PCR (polymerase chain reaction) was usually performed with mixtures as in **Table 6**. The usual PCR cycler program, performed in GE-touch thermal gradient cycler (Bio-Gener, Hangzhou, China), is listed in **Table 7**.

Table 6: PCR mixtures used for molecular cloning. Reaction WAS prepared on ice in PCR thin-wall microtubes or PCR strips. dNTPs, deoxyribonucleoside triphosphate.

Component	Quantity
Nuclease-free H_2O	Filled to volume 25 µl
5× Q5 reaction buffer (New England Biolabs, Ipswich, Massachusetts, USA)	5 µl
10 mmol/l dNTPs	0.5 µl
10 µmol/l forward primer	1.25 µl
10 µmol/l reverse primer	1.25 µl
Template DNA	~1 ng of plasmid DNA
Q5 Hot Start High Fidelity DNA polymerase (New England Biolabs, Ipswich, Massachusetts, USA)	0.25 µl

Table 7: PCR program used for molecular cloning.

Step	Cycle	Temperature	Time
Initial denaturation	1×	98 °C	30 s
Denaturation	30×	98 °C	10 s
Annealing of primers		Calculated by online NEB Tm Calculator	20 s
Elongation		72 °C	30 s / kb of amplicon
Final extension	1×	72 °C	120 s

DNA was digested using FastDigest endonucleases BsrGI, KpnI, PmeI, XhoI (Thermo Fisher Scientific, Waltham, Massachusetts, USA). Reactions were set in microcentrifuge tubes. The composition was following: 1 µl of enzyme (or each enzyme if multiple were used), 2 µl of 10× FastDigest Green buffer, 10 µl extracted DNA or 1 µg of plasmid DNA, nuclease-free H_2O filled to 20 µl. The digestion was performed at 37 °C for 30 min.

PCR products and DNA digested by endonucleases were analysed on 0.8% agarose gels prepared with TAE buffer and labelled in-gel by 0.01% (w/V) ethidium bromide. Bands of desired lengths were cut out of the gel and contained DNA was isolated using agarose gel extraction kit (Jena Bioscience, Jena, Germany), according to manufacturer's manual.

Ligation of vector backbone and inserts was carried in the following setup: 6 µl of kit-purified insert was mixed with 2 µl of digested and kit-purified backbone, 1 µl of T4 ligase buffer, and T4 DNA ligase (Thermo Fisher Scientific, Waltham, Massachusetts, USA); mixed well and incubated overnight at 20 °C.

Ligated constructs were transformed to transformation-competent *E. coli* DH5α strain (prepared after (Inoue *et al.* 1990)) for plasmid amplification by heat shock method. 100 µl of bacterial suspension was thawed on ice and incubated with ligated plasmid for 30 min. After the heat shock at 42 °C for 60 s, the suspension was chilled on ice for 5 min and then regenerated at 37 °C for at least 30 min with added 250 µl of SOB medium. The suspension was then planted on an agar PD ampicillin and incubated overnight at 37 °C.

Colonies of transformed *E. coli* were tested by colony PCR for presence of the desired plasmid sequence and orientation of inserted DNA fragments. In brief, a pair of primers aligning both to inserted and backbone sequences was used. Diluted single colony biomass was used instead of template DNA. Initial denaturation was prolonged to 90 s for colony PCR. Positive colonies were then inoculated to 4 ml of LB containing 100 µg/ml ampicillin and incubated at 37 °C overnight on a shaker. Plasmids were isolated using GeneJET Plasmid Miniprep kit (Thermo Fisher Scientific, Waltham, Massachusetts, USA) according to manufacturer's manual. DNA concentration was measured using NanoDrop One (Thermo Fisher Scientific, Waltham, Massachusetts, USA). Plasmids were verified by Sanger dideoxy termination sequencing method at DNA sequencing facility, Faculty of Science, Chares University, Prague.

3.2.1.3. Human cell culture *in vitro*

Human cells were cultured at 37 °C, 5 % CO_2 humidified atmosphere. Cells were passaged at ~90 % confluency; usually, 90 % of cells was removed during a passage. Cells were first washed with sterile PBS and detached from the surface by trypsin-EDTA solution (Biowest, Riverside, Missouri, USA). Trypsin was then inactivated by adding serum-containing media to cells. Cells were centrifuged 120 g, 3 min. Supernatant was discarded, pellet of cells was resuspended in fresh medium. 1/10 of cells was planted back to original container (usually a 25 cm^2 flask) with fresh media.

3.2.1.4. Transfection of cells for microscopy and selection of RPE stable lines

For transient expression of vectors, cells were transfected by X-tremeGENE HP DNA transfection reagent (Roche, Basel, Switzerland). Cells were planted onto 4-chamber 3.5cm PDs and transfected after four hour after planting earliest. 0.5 µg of plasmid DNA was diluted in DMEM without serum nor antibiotics and mixed well. 1 µl of X-tremeGENE reagent was pipetted directly into the mixture and mixed. The transfection mixture was added directly onto cells after 20 min of incubation. RPE cells were induced upon transfection with 20 ng/ml doxycycline. All cells were observed on a confocal microscope 24 h after transfection.

For selection of RPE stable lines, RPE cells were planted onto 6-well dish plasticware. After 6–24 h, cells were transfected with jetOPTIMUS transfection reagent (Polyplus transfection, Illkirch, France). In 200 µl of jetOPTIMUS buffer, 0.2 µg of pGFT plasmid DNA was mixed with 1.8 µg of pOG44 vector DNA bearing the flippase gene. Then, 3 µl of jetOPTIMUS transfection reagent was pipetted directly into the solution. After 10 min of incubation, the mixture was loaded directly onto cells. The medium was replaced for fresh 4 h after transfection. Negative (no pGFT DNA) and positive (an unrelated vector with GFP gene, without FRT sequence) controls were included in each transfection. Transgenic cells were selected by geneticin (G418 sulphate) antibiotic (Thermo Fisher Scientific, Waltham, Massachusetts, USA), added to media one day after transfection, 400 µg/ml (adjusted to partial potency of the antibiotic). Selection was carried until all cells in negative control died. For microscopy, cells were induced by 20 ng/ml doxycycline one day prior.

3.2.1.5. Isolation of intact MTs from RPE cells

One 10cm PD of RPE stable cell line was grown for each isolation experiment to ~95 % confluency. Cells were induced 24 h before starting the experiment by 20 ng/ml doxycycline hyclate (Merck KGaA, Darmstadt, Germany) added to culture media. MTs were stabilized 1 h prior to isolation from cells by supplying 10 µmol/l paclitaxel (Merck KGaA, Darmstadt, Germany) to culture media. Cells were washed with PBS and detached from culture surface by trypsin-EDTA. Cells were pelleted by centrifugation at 200 g, 3 min, followed by PBS wash and second centrifugation. Pelleted cells were carefully resuspended in 200 µl of lysis buffer (for isolation of intact MTs). Suspension was sonicated by 4 pulses of 20 % power, 0.4 s, using UP50H sonicator with sonotrode MS1 (Hielscher Ultrasonics GmbH, Teltow, Germany). If necessary, four extra pulses were executed, based on a quick observation on a confocal microscope. Sonicated cell suspension was spun down at 500 g for 8 min. The supernatant was then used for immunoprecipitation of isolated free MTs on antibody-coupled agarose beads.

3.2.1.6. Isolation of MTs polymerized in cell lysate of RPE cells

Two 10cm PD of RPE stable cell line was grown for each isolation experiment to ~95 % confluency. Cells were induced 24 h before starting the experiment by 20 ng/ml doxycycline hyclate (Merck KGaA, Darmstadt, Germany) added to culture media. Cells were washed with PBS and detached from dish surface by trypsin-EDTA. Cells were pelleted by centrifugation at 200 g, 3 min, followed by PBS wash and second centrifugation. Pelleted cells were resuspended in 200 µl of cold lysis buffer (for polymerization in lysate). Suspension was sonicated on ice by 5 × 4 pulses of 90 % power, 0.9 s, using UP50H sonicator with sonotrode MS1 (Hielscher Ultrasonics GmbH, Teltow, Germany). Cell lysates were centrifuged in ultracentrifuge 1.5 ml tubes using Optima MAX-XP Ultracentrifuge (Beckman Coulter Life Sciences, Indianapolis, Indiana, USA) at 70,000 g, 4 °C, 35 min.

Supernatant was moved to a new tube, supplemented with 1.5 mmol/l GTP (to stabilize MTs and promote polymerization) and 1 µl of 3 mmol/l cytochalasin D (inhibitor of actin polymerization). Samples were then warmed to 37 °C for 45 minutes to induce polymerization of MTs. Samples were observed on a confocal microscope; samples were resonicated by 4 pulses, 20 % power, 0.4 s in cases when MTs were too tangled together. Samples were then used for immunoprecipitation of polymerized free MTs on antibody-coupled agarose beads.

3.2.1.7. Immunoprecipitation of free MTs

Pierce protein A/G magnetic agarose beads (Thermo Fisher Scientific, Waltham, Massachusetts, USA) were preincubated with anti-tubulin YL1/2 antibody diluted 1:50 in PBS at 4 °C overnight on a rotator. 50 µl of original slurry was used per one sample for immunoprecipitation. Before immunoprecipitation for MTs enrichment, beads were pelleted by a magnet and washed twice with PBS. All liquid was then discarded and beads were mixed with sample containing free MTs. Samples were then incubated one hour on a rocker at room temperature to bind MTs to the beads.

A series of washing steps in buffers with increasing ionic strength and supplied with 10 µmol/l paclitaxel then followed. Samples for mass spectrometry (MS) analysis were taken along. After the incubation, all supernatant was discarded and the beads were gently washed with 200 µl of BRB80 twice. 60 µl of BRB80 was then used to resuspend the beads and 15 µl was taken as a MS test sample. Rest was discarded. Beads were then washed twice with 200 µl of HMP400 and resuspended in 45

µl of HMP400, of which 15 µl was taken for MS analysis. Washing with HMP600, 200 µl twice, then followed. Finally, beads were resuspended in 30 µl HMP600 and 15 µl was taken for MS analysis.

3.2.1.8. Confocal fluorescent microscopy

Confocal microscopy was performed on Carl Zeiss LSM 880 NLO microscope with Zen Black software version 2.1 SP3 (Carl Zeiss AG, Oberkochen, Germany). Setting was kept unchanged for acquisition of corresponding samples of one experiment, inter-experiment changes were minimalised. All pictures were taken with plan-apochromat 63× oil objective M27, 1.4 numerical aperture. For differential interference contrast (DIC), transmitted light illuminator HAL 100 was used with corresponding detector LSM T-PMT. Fluorescence was acquired using argon laser excitation (488 nm), usually set to 0.5 % (live-cell imaging), or 2 % (isolation of MTs). Emission of GFP was detected using MBS 488 and spectral 32-channel GaAsP detector between 490–606 nm. The pinhole was set to 1 Airy unit. All acquisition was done in integration mode with detector master gain 800, digital offset 0 and digital gain 1. For live-cell imaging, 3.5cm PD holder was used. Objective and XL covering box were heated to 37 °C, and humidified atmosphere with 5 % CO_2 was supplied. Images were processed by Fiji software (Schindelin *et al.* 2012). For the purpose of clear readability, contrast levels were adjusted in presented pictures (denoted for each picture in the caption).

3.2.2. MIPs in axonemal MTs (TAILS complex)

3.2.2.1. IF labelling of sperm cells in suspension

Staining and washing media were removed by pelleting the cells in a centrifuge at 500 g, 4 °C, 5 min. Samples were left on a rotator at room temperature for incubation steps. Cells were washed twice with 0.1% (w/V) polyvinyl alcohol in PBS filtered on a filter with 0.3 µm pores after each incubation step.

30 pejets with frozen sperm from liquid nitrogen storage were thawed in warm water bath and collected into a microcentrifuge tube. Cells were washed and fixed by 3% PFA in MSB for 20 minutes. For staining steps, suspension volume was split into stained samples and control samples. Primary antibody labelling was performed in 0.5% Triton X-100 with 3% BSA (bovine serum albumin) in MSB for 2 h; TAT1 tubulin antibody was diluted 25×, DCDC2C antibody was diluted 150×. Secondary antibodies staining was performed again in 0.5% Triton X-100 with 3% BSA in PBS for 2 h; GAR cy3 and DAM DL488 were both diluted 400×. Antibody solutions were spun 14,300 g for 3 min to remove precipitations and contaminants. Controls were treated as full-stained sample except for concomitant primary and secondary antibodies were omitted.

Stained sperm samples were checked on a microscope. Nuclei were stained overnight with 100 ng/ml DAPI (4',6-diamidino-2-phenylindole). Sonication was executed on ice, 2 × 5 pulses of 80 % power, 0.8 s, using UP50H sonicator with sonotrode MS1 (Hielscher Ultrasonics GmbH, Teltow, Germany).

3.2.2.2. Widefield fluorescent microscopy of sperm cells

IF-labelled bull sperm cells were imaged on DM6B-Z fluorescent microscope equipped with DFC7000 T camera (Leica Microsystems CMS GmbH, Wetzlar, Germany). All images were taken with HC PL FLUOTAR dry objective, magnification 40×, 0.8 numerical aperture. Channels, excitation bandpass (BP) filters (centre of permitted band in nm / width of band in nm), dichroic mirrors (DM), and suppression longpass (LP) filters (shortest wavelength permitted in nm) were set-up in following way: DAPI – BP 360/40, DM 400, LP 425; green – BP 470/40, DM 510, LP 515; red – BP 545/25, DM 565, BP 605/70. Brightfield channel was imaged with phase contrast (technique PH2). Köhler's illumination was set for all acquisitions. Exposure time and gain were 300 ms and 5 for DAPI, 800 ms and 8 for green and red. All three channels were acquired with lamp intensity set at 17 %. The microscope was operated with LAS X software, version 3.7.3.

3.2.2.3. FACS of IF labelled sperm cells

IF labelled, sonicated, and DAPI-stained bull sperm was sorted using FACSAria Fusion cytometry sorter (BD, Franklin Lakes, New Jersey, USA). IF labelling and fragmentation was checked for each sample including controls before sorting.

Prior to loading into the sorter, samples were diluted in PBS and filtered with a 50µm pore size filter if necessary. Sheath pressure (sorting liquid: sterile PBS) was set to 75 psi and 70 µm nozzle was used. Fluorescence excitation was carried out by 405, 488, and 561 nm lasers. Detectors, band-pass (BP) filters (centre of band in nm / width of band in nm), and voltages were set as following: FSC – BP 488/10, 300 V; SSC – BP 488/10, 300 V; DAPI – BP 450/50, 405 V; FITC – BP 525/20, 460 V; PE – BP 585/15, 600 V. Detection threshold for FSC (to discriminate events from noise) was 500. Compensation matrix was not set.

Data were acquired in BD FACSDiva software version 8.0.1. Control samples were measured first (intact cells, sonicated cells, DAPI-stained intact cells, DAPI-stained sonicated cells). Single stained cells were measured afterwards. At least 10,000 events were acquired for each control sample. Triple-stained samples for sorting were first recorded without sorting to analyse their fluorescent properties and set areas for gating. Gating strategy excluded all DAPI-positive fragments and sorted two fractions, tip-enriched (tubulin+, DCDC2C+, and tip-depleted (tubulin+, DCDC2C−).

Sorted fractions were supplied with cOmplete protease inhibitors (Roche, Basel, Switzerland) to reach 1× concentration. Sorted fragments were pelleted by centrifugation 50,000 g, 4 °C, 1 h in Optima XPN-90 ultracentrifuge with SW 40 Ti swinging-bucket rotor and 14 × 95 mm open-top polypropylene centrifuge tubes (Beckman Coulter Life Sciences, Indianapolis, Indiana, USA).

3.2.2.4. Fluorescent spectrophotometry of sorted sperm cells

To validate the quality of sorted fractions, we measured fluorescence spectra using a spectrofluorometer FluoroMax-3 (Horiba Ltd., Kyoto, Japan). Samples were pipetted into sterilised quartz cuvettes and mixed before analysis. Synchronous spectra with 20 nm excitation–emission wavelength offset were recorded; data were corrected for lamp emission profile. Fluorescence was integrated over 0.5 s and measured between 420 and 600 nm in 2 nm intervals. Unstained sonicated cells were used as a control. Measured spectra were normalised to 1 by average intensity of emission on interval of 440–460 nm. To calculate enrichment of red fluorescent signal compared to green signal, average intensities in intervals 494–498 nm and 550–554 nm were considered (with subtracted emission of negative control in these intervals). The ratio of green emission intensity / red emission intensity was then calculated for both sorted fractions.

3.2.2.5. Mass spectrometry

Samples were de-crosslinked at 98 °C for 30 min. Mass spectrometry analysis was performed by facility staff at Proteomics Core Facility, EMBL, Heidelberg, Germany. Briefly, disulphide bridges in the samples were reduced by dithiothreitol and cysteines were alkylated with 2-chloroacetmide. Samples were digested by trypsin to produce short peptides. Samples were labelled with Tandem Mass Tag (TMT10plex) labels. Peptides were purified in liquid chromatography column and directly loaded by spraying into Orbitrap Fusion mass spectrometer (Thermo Fisher Scientific, Waltham, Massachusetts, USA). Full mass scan was acquired with mass range 375-1500 m/z. High complexity full proteomes were obtained; tip-enriched and tip-depleted fractions were then compared. Proteins with only one unique peptide were dropped from the analysis. A protein was considered a “hit”, if the false discovery rate was smaller 0.05 and a fold change of at least 2-fold was observed. A protein was considered a “candidate”, if the false discovery rate was smaller 0.2 and a fold change of at least 1.5-fold was observed.

4. Results

4.1. MIPs in dynamic MTs

In the first part of this diploma thesis, we endeavoured to identify new candidates for MIPs in dynamic MTs. We worked with human cell lines cultured *in vitro* as source material for their easy production in large quantities and the availability of biochemical and genetic methods.

We undertook two independent methodical approaches for MIPs identification – the BioID approach, and the direct isolation approach.

4.1.1. BioID approach

In this approach, we aimed to produce a MIP candidate list by the BioID proximity labelling method. In BioID, proteins in the close vicinity of an active biotin ligase are covalently labelled by biotin moieties. We exploited the fact that αTAT1 and MAP6 (Coombes *et al.* 2016, Cuveillier *et al.* 2020) were already shown to localize inside MTs. αTAT1 and MAP6 were tagged by miniTurbo, a recently published promiscuous biotin ligase with enhanced processivity (Branon *et al.* 2018). MiniTurbo should be brought inside the lumen of MTs, where it can preferentially biotinylate other MIPs in proximity. Biotinylated proteins then could be isolated by streptavidin-conjugated beads and identified by MS.

4.1.1.1. Inducible RPE cell lines expressing BioID-tagged proteins were generated.

To circumvent the necessity to repeatedly transfect cultured cells for expression of the biotin ligase, we decided to produce Tet-On RPE cell lines expressing desired protein constructs when doxycycline is added to the media. We used the Flp-in system with FRT homologous recombination sites and geneticin resistance to generate the transgenic lines (**Table 8**).

Each construct was tested on transiently transfected Tet-On RPE cells (which require induction by doxycycline for expression). Additionally, these constructs were also transfected to wild-type U-2 osteosarcoma cells (U2OS; induction-independent) to compare cell type-dependent effects. Finally, we checked the localisation of fusion proteins in stable lines themselves. Results from these experiments are in the figures below. The summary of observed localization patterns is in **Table 8**.

Table 8: List of generated Tet-On RPE inducible lines and figures with corresponding transfected cells or stable cell lines. A short description of observed localization patterns in GFP constructs is also stated.

Fusion proteins	Figure	Localization pattern
miniTurbo-GFP	Fig. 12	Cytosolic
GFP-αTAT1	Fig. 13	Cytosolic
αTAT1-GFP	Fig. 14	Cytosolic (poorly expressed)
miniTurbo-GFP-αTAT1	Fig. 15	Cytosolic
GFP-MAP6	Fig. 16	Mostly cytosolic, Golgi apparatus (RPE cells), rarely centrosomes (U2OS cells and RPE stable lines)
MAP6-GFP	Fig. 17	Cytosolic, MTs (U2OS cells, transfected RPE cells), Golgi apparatus (RPE cells)
miniTurbo-GFP-MAP6	Fig. 18	Cytosolic
MAP6-miniTurbo-GFP	Fig. 19	MTs, Golgi apparatus (RPE cells)
miniTurbo-GFP-MAP4	Fig. 20	MTs
GFP-α-tubulin	Fig. 24	MTs, cytosol

MiniTurbo-GFP protein had homogenous cytoplasmic localization, with infrequent protein clusters in strongly transfected cells (**Fig. 12**). MiniTurbo by itself does not localise to any specific organelle. Out of all vectors with αTAT1, none had MT localization (**Fig. 13**, **Fig. 14**, **Fig. 15**). GFP-MAP6 protein, on the other hand, showed localization to centrosomes, surrounding MTs, Golgi apparatus, and cytoplasm (**Fig. 16**). Switched order of proteins in the MAP6-GFP vector did not improve the

localization; only weakly transfected U2OS and RPE cells had partial MT localization (**Fig. 17**). Mini-Turbo-GFP-MAP6 fusion protein did not localize to MTs and accumulated in the cytoplasm (**Fig. 18**). Sufficient localization was reached with MAP6-miniTurbo-GFP vector (**Fig. 19**). It had MT localization in U2OS cells; in RPE cells, Golgi apparatus was possibly positive as well besides MTs. The best localization was observed for MAP4 protein in miniTurbo-GFP-MAP4 vector (**Fig. 20**), which localized solely to MTs in all cases.

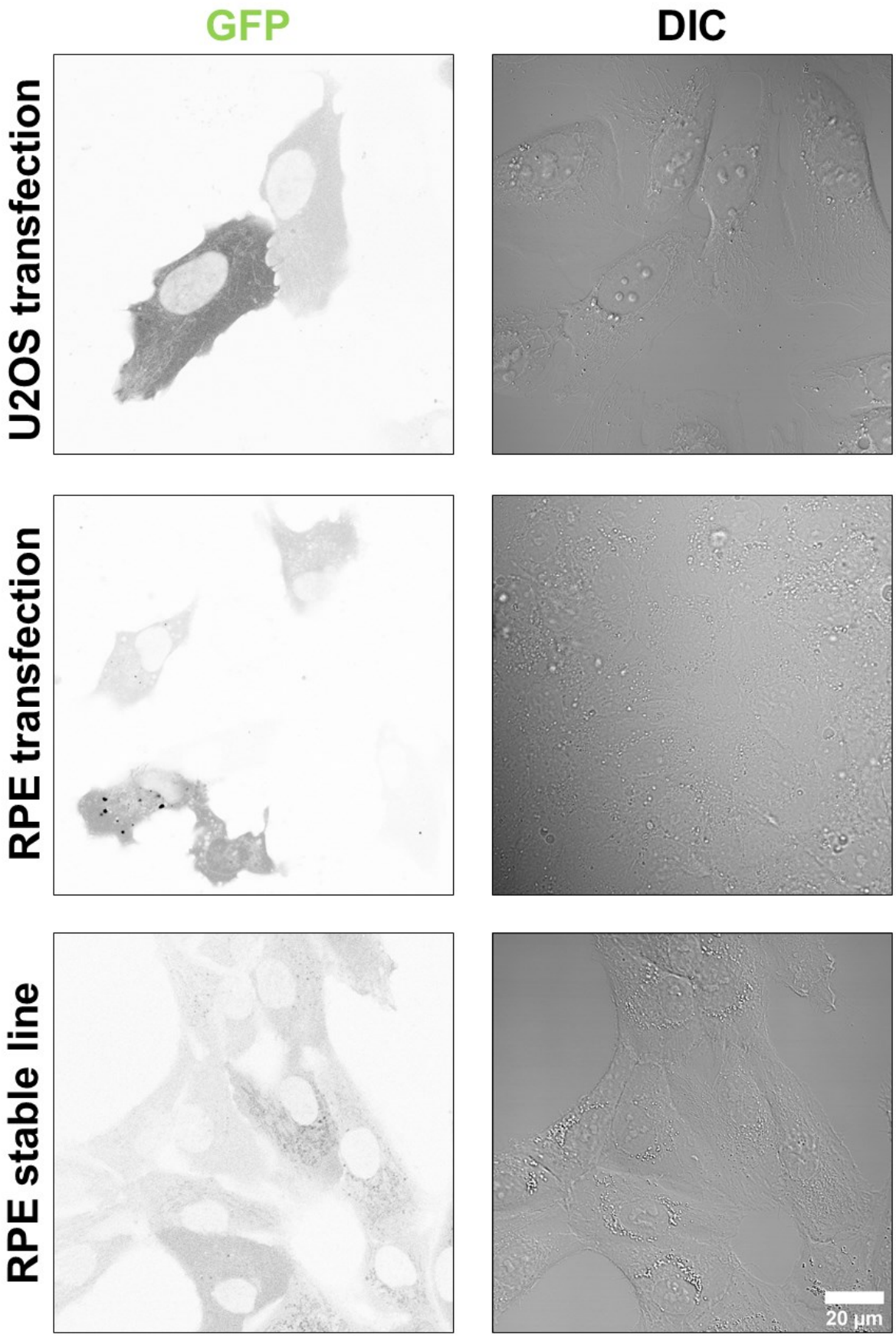

Fig. 12: MiniTurbo-GFP vector in U2OS and RPE cells. The localization was cytosolic in all three cases. In some strongly transfected cells, the fusion protein aggregated. Contrast: 200/255 U2OS, 200/255 RPE transfection, 230/255 RPE stable line.

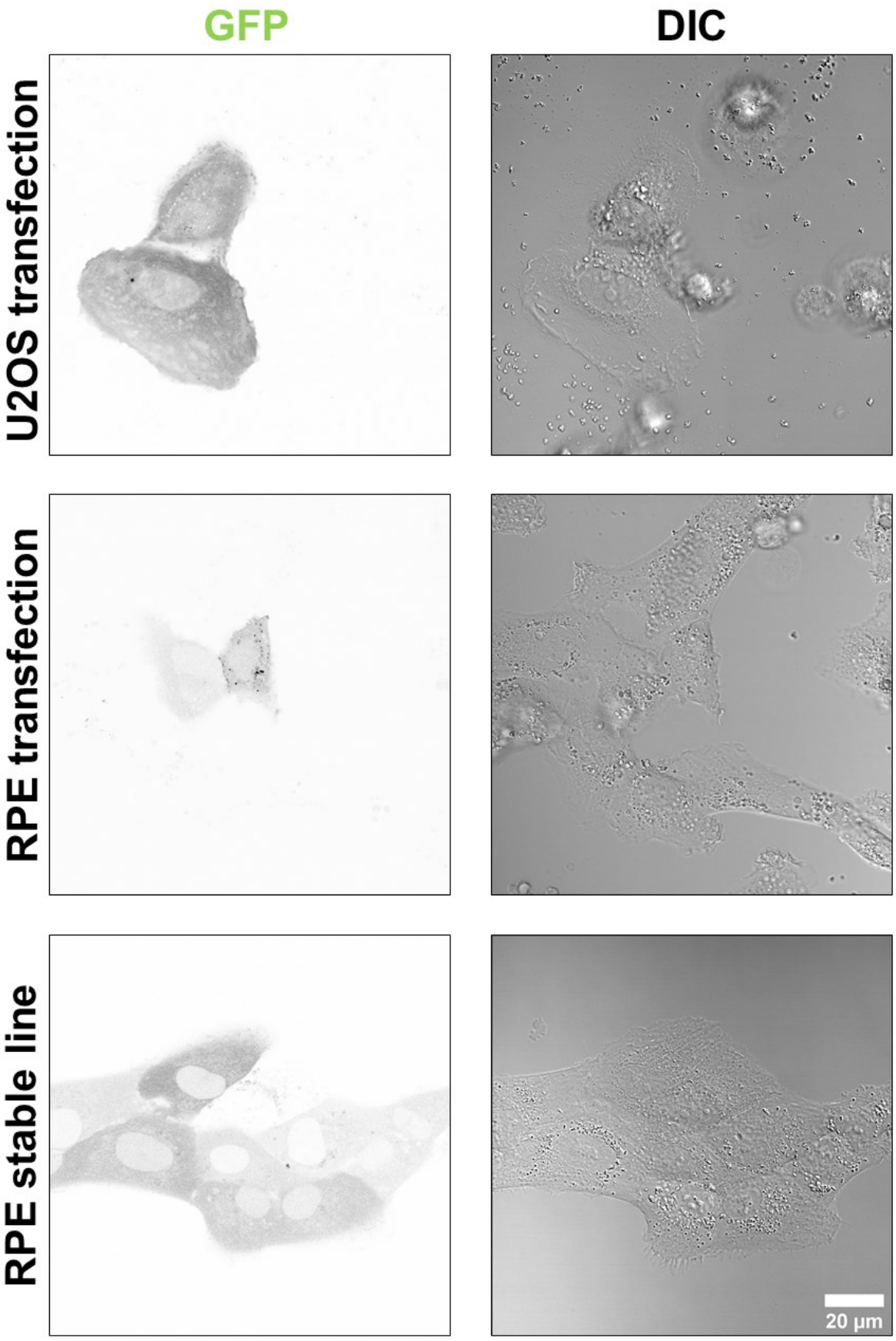

Fig. 13: GFP-αTAT1 vector in U2OS and RPE cells. The localization was cytosolic in all three cases. In some strongly transfected cells, the fusion protein aggregated. No localization to microtubules was ever observed with this vector. Contrast: 200/255 U2OS, 200/255 RPE transfection, 200/255 RPE stable line.

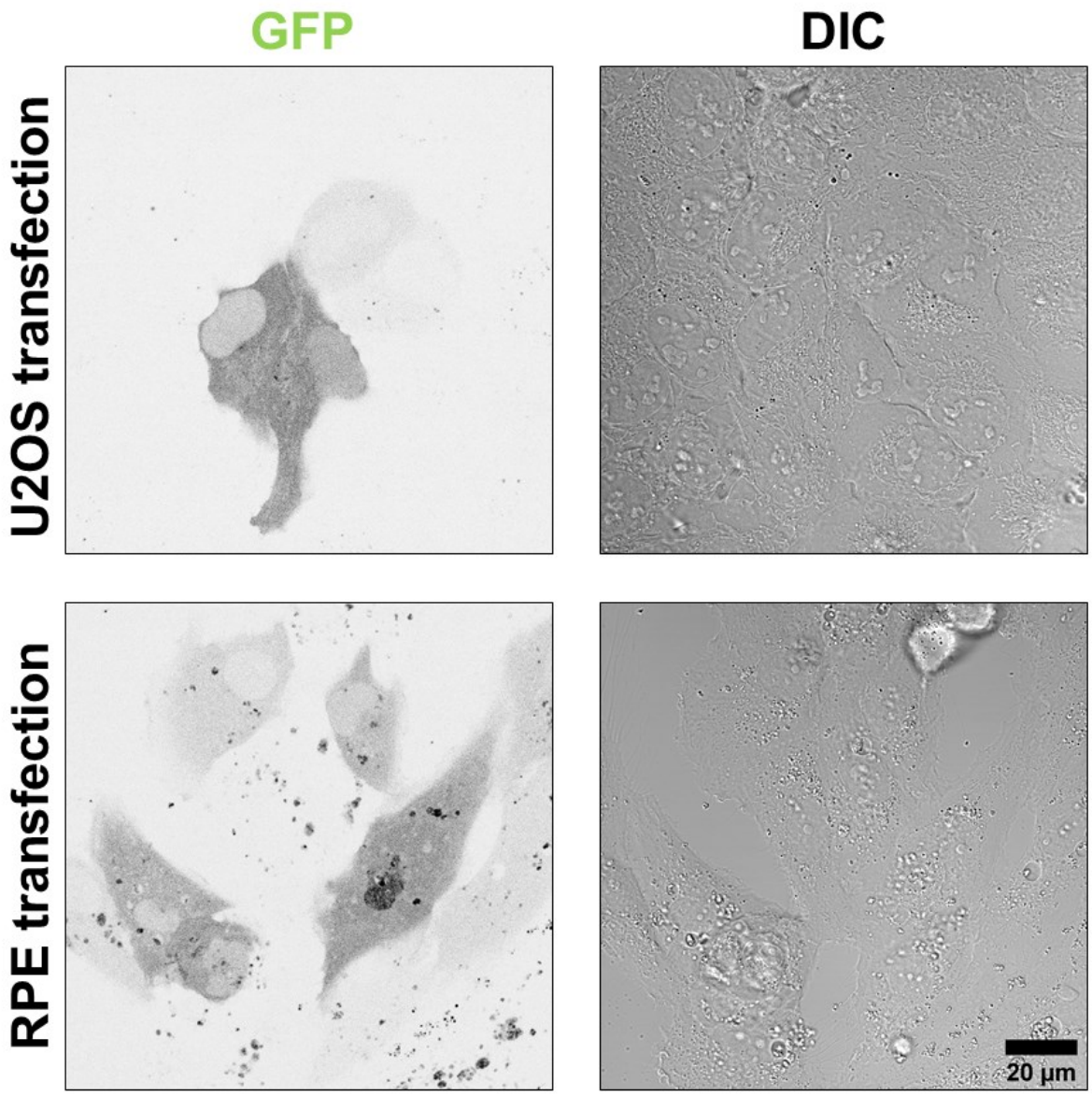

Fig. 14: αTAT1-GFP vector in U2OS and RPE cells. RPE stable line with this vector was not produced. The localization in transfection experiments was cytosolic for U2OS and RPE. The vector expressed very poorly. Transfected RPE cells showed elevated autofluorescence in vesicles. Contrast: 240/255 U2OS, 240/255 RPE transfection.

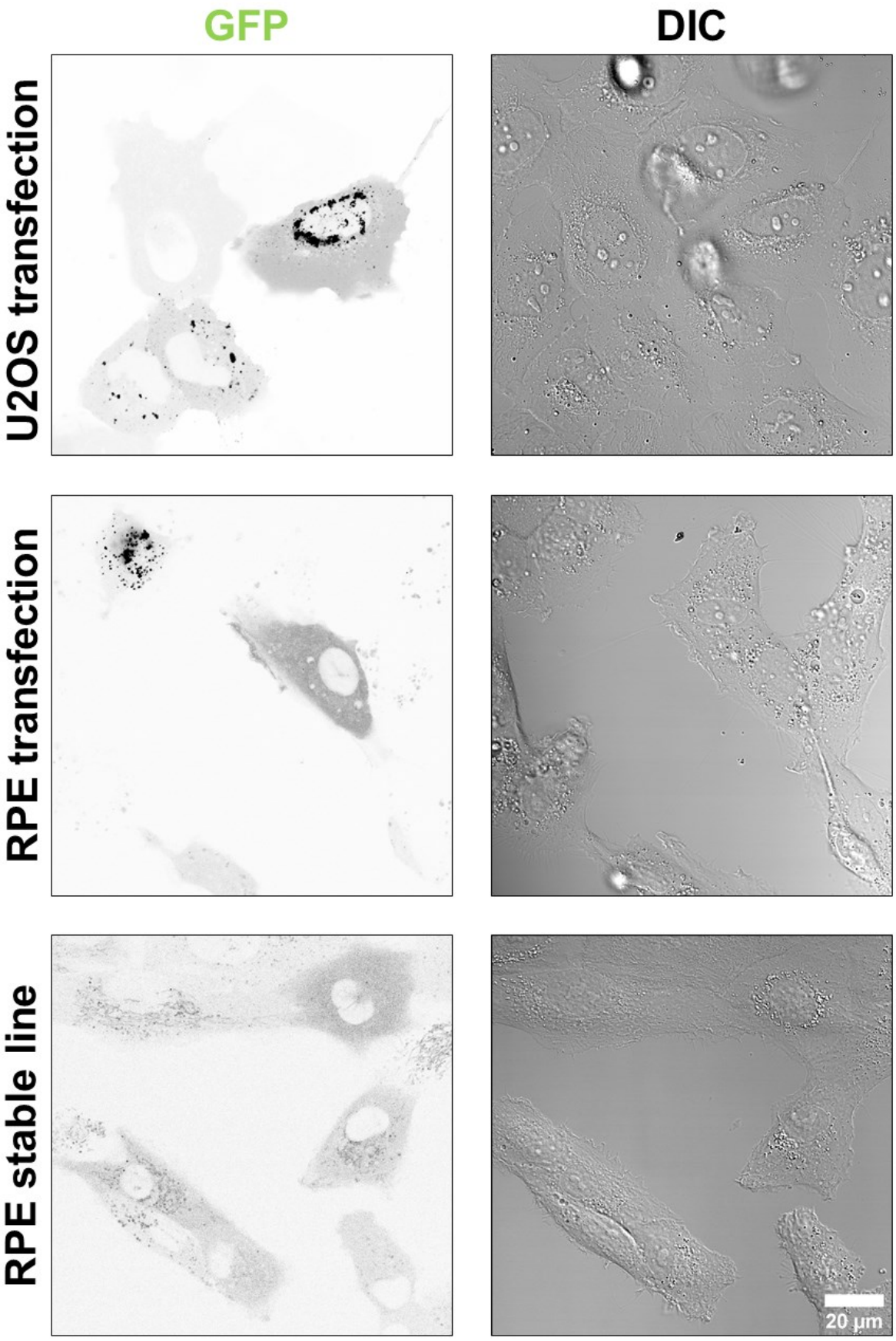

Fig. 15: miniTurbo-GFP-αTAT1 vector in U2OS and RPE cells. The localization was cytosolic in all three cases. In some strongly transfected cells, the fusion protein aggregated. No localization to microtubules was ever observed with this vector. GFP signal in RPE stable line was very weak. Contrast: 0/255 U2OS, 0/255 RPE transfection, 240/255 RPE stable line.

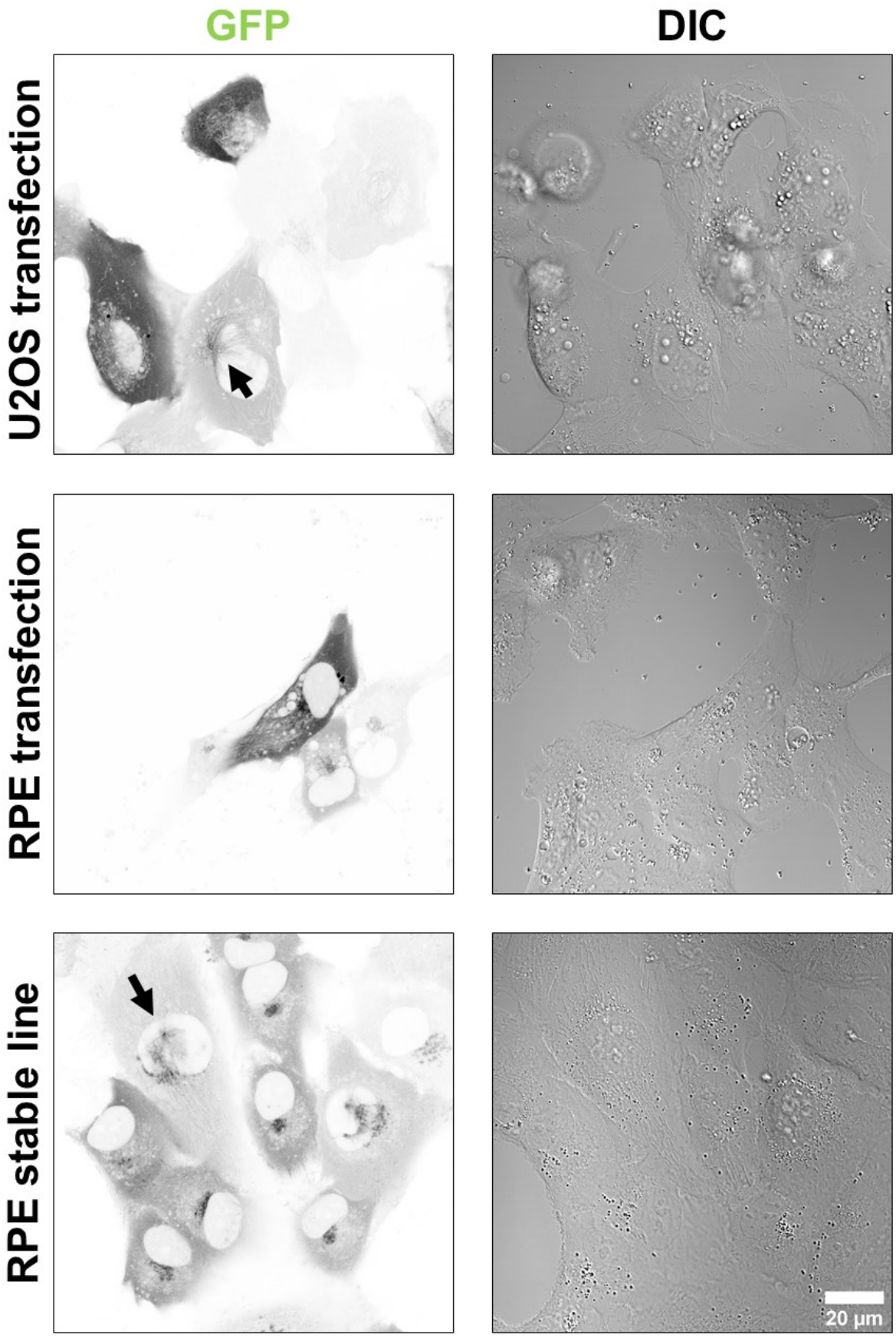

Fig. 16: GFP-MAP6 vector in U2OS and RPE cells. The localization was mostly cytosolic. In RPE cells, Golgi apparatus was also GFP positive. Rarely, in U2OS transfected cells and in RPE stable line, centrosomes and radial MTs around were visible (arrows). Contrast: 80/255 U2OS, 80/255 RPE transfection, 80/255 RPE stable line.

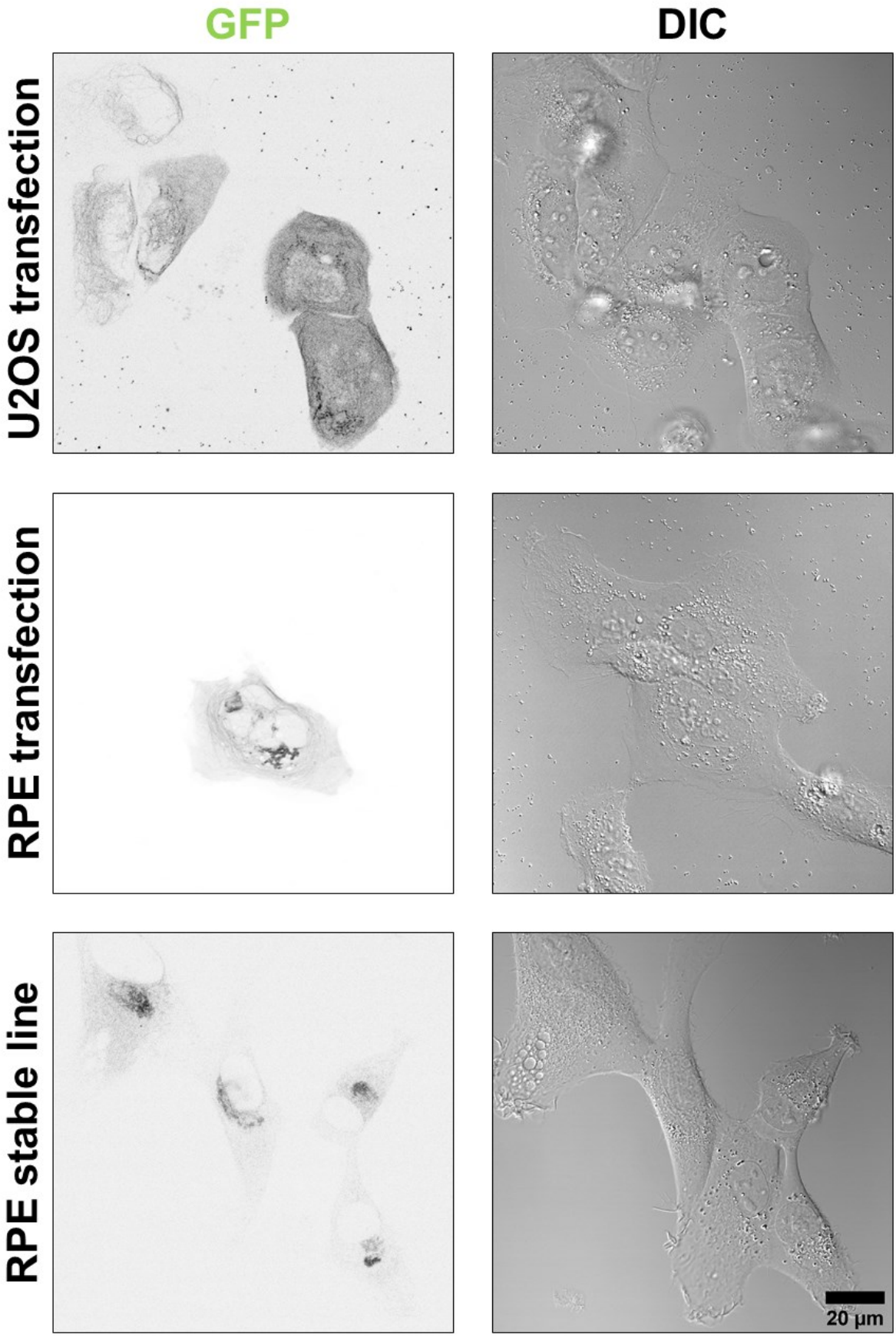

Fig. 17: MAP6-GFP vector in U2OS and RPE cells. The fusion protein localization in U2OS transfected cells was mainly cytoplasmic, MTs were positive as well in weakly transfected cells. Transfected RPE cells showed MT localization, strong signal in vesicles (possibly Golgi apparatus), and weakly in cytoplasm. Stable RPE line had weak cytoplasmic and strong Golgi signal, no MTs were observed. Contrast: 240/255 U2OS, 100/255 RPE transfection, 240/255 RPE stable line.

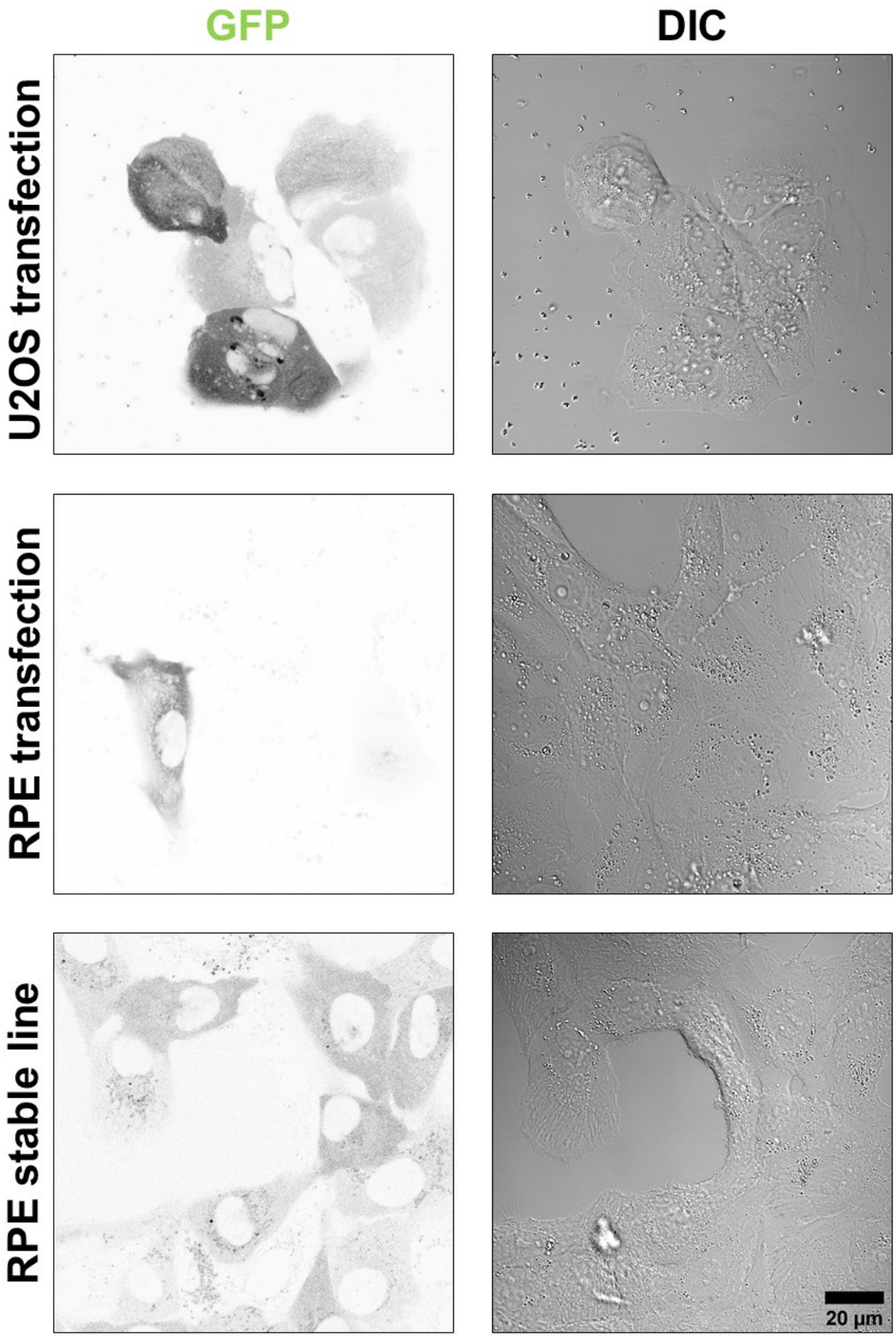

Fig. 18: miniTurbo-GFP-MAP6 vector in U2OS and RPE cells. The localization was cytoplasmic in all cases; strongly transfected U2OS cells contained protein aggregates. Signal in RPE stable line was on the similar level to autofluorescence of some vesicles. Contrast: 200/255 U2OS, 100/255 RPE transfection, 240/255 RPE stable line.

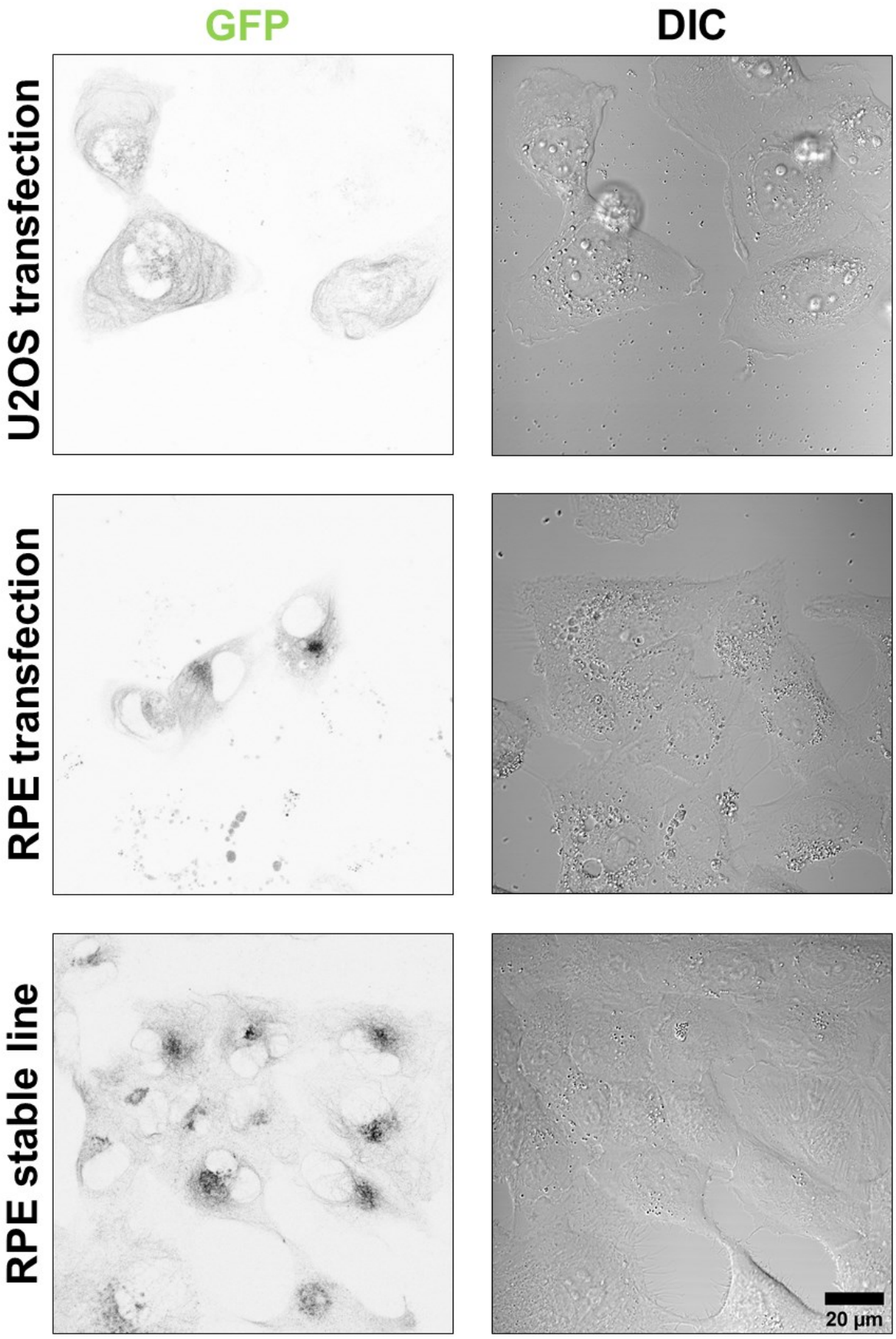

Fig. 19: MAP6-miniTurbo-GFP vector in U2OS and RPE cells. The expressed protein localized to MTs in U2OS cells. In both transfected RPE and stable line RPE cells, the localization was both to MTs and Golgi. Highly autofluorescent vesicles were observed in transfected RPE cells. Contrast: 200/255 U2OS, 220/255 RPE transfection, 230/255 RPE stable line.

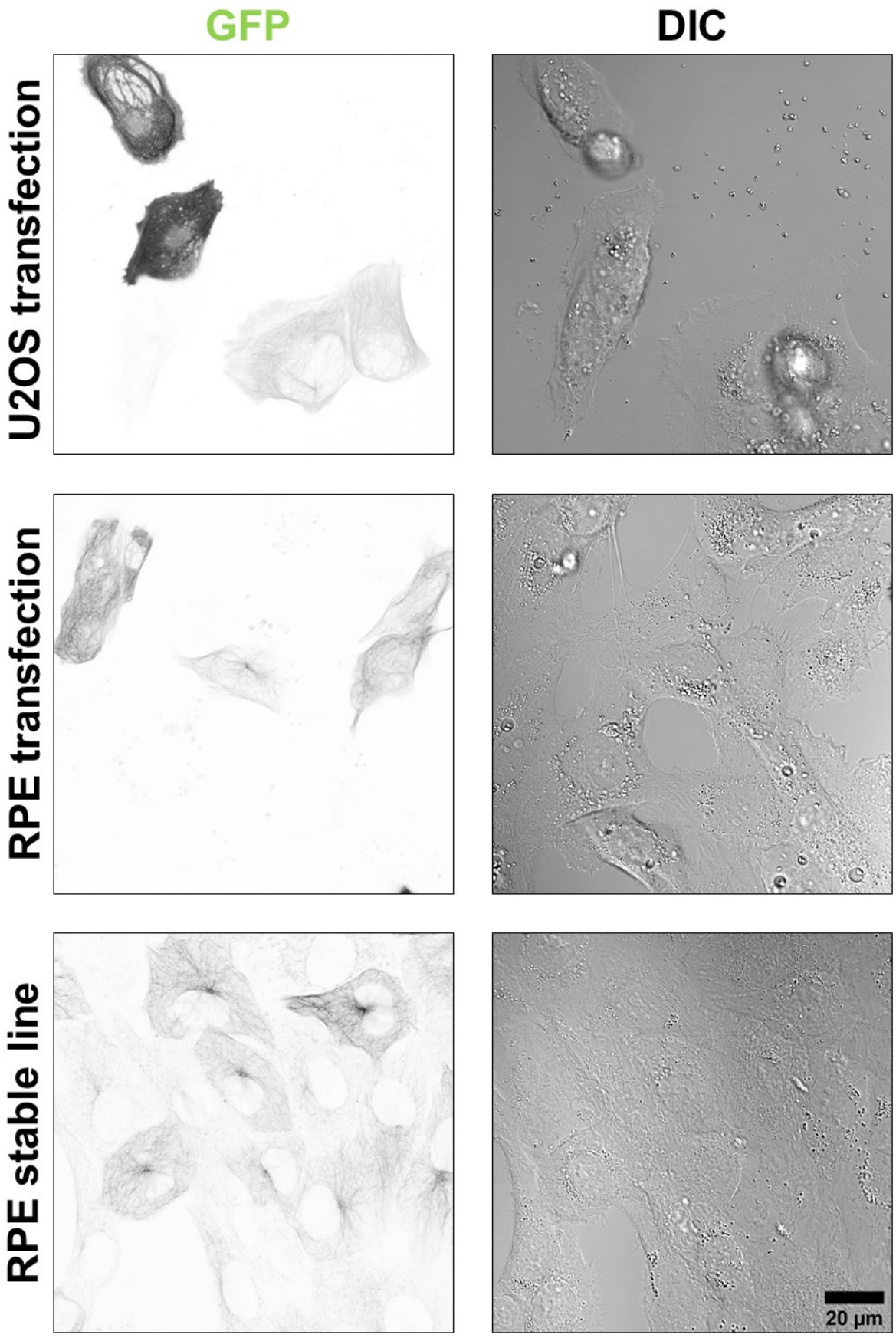

Fig. 20: MiniTurbo-GFP-MAP4 vector in U2OS and RPE cells. The localization was correct on MTs in all cells. Contrast: 0/255 U2OS, 150/255 RPE transfection, 0/255 RPE stable line.

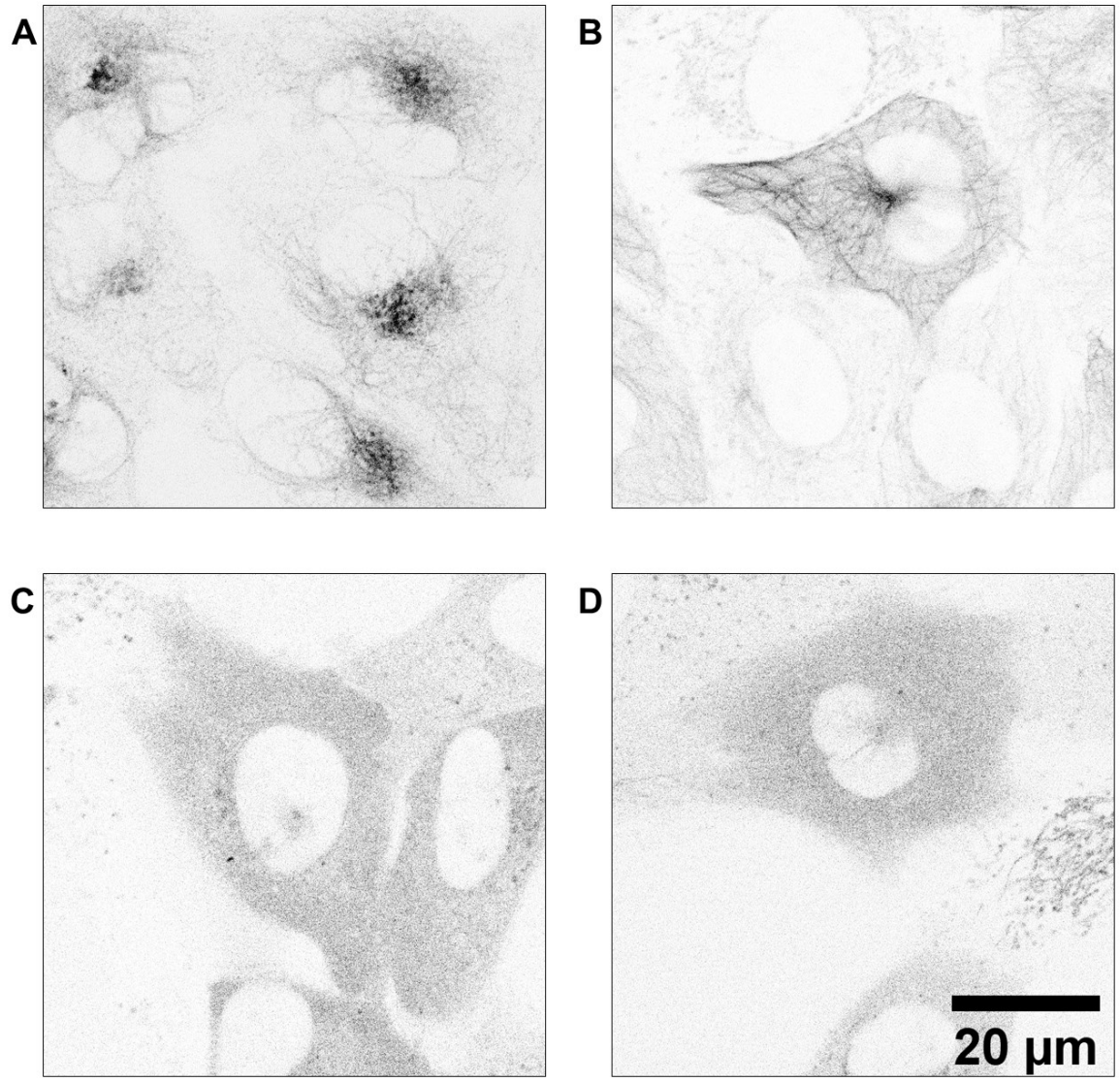

Fig. 21: Detail of four induced RPE stable lines. GFP signal after induction is in all panels. **A:** MAP6-miniTurbo-GFP line, expressed fusion protein localizes to MTs and Golgi apparatus. **B:** miniTurbo-GFP-MAP4 line, localization to MTs. **C:** miniTurbo-GFP-MAP6 line, cytoplasmic localization. **D:** miniTurbo-GFP-αTAT1, cytoplasmic localization. Contrast: **A** 230/255, **B** 0/255 **C** 240/255, **D:** 240/255.

Based on the observed localization of expressed proteins in stable RPE lines (**Fig. 21**), we excluded αTAT1 vectors from biotinylation experiments. They did not provide localization to MTs, so no enrichment of MIPs could be expected in the resulting biotinylated proteome. We continued only with MAP6-miniTurbo-GFP vector plus miniTurbo-GFP-MAP4 as control with localization to the outer surface of MTs. GFP-α-tubulin line (**Fig. 24**) was used in intact MTs isolation approach for identifying MIPs (chapter 4.1.2).

4.1.1.2. Proteins were labelled by miniTurboin in biotinylation experiments.

We first tested the biotinylation activity of the miniTurbo-GFP-MAP4 construct (**Fig. 22**) to see the endogenous background of biotinylated proteins and possible leakage of expression without induction by doxycycline. Induced cells of the RPE stable line were incubated with biotin added to culture media 10, 60, or 120 min before cell harvesting. As expected, longer biotin incubation resulted in a larger amount of biotinylated proteins, as revealed by western blot labelled by streptavidin-HRP (horseradish peroxidase). No biotinylated proteins were observed in uninduced cells or cells without biotin supplemented in media.

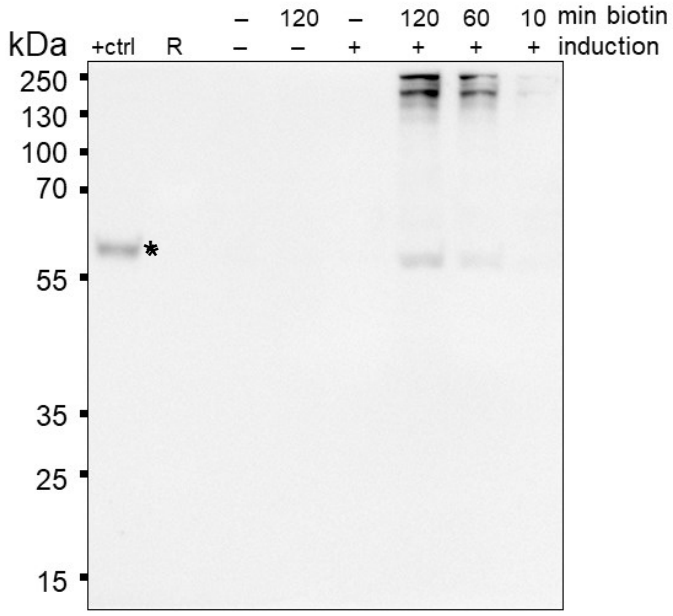

Fig. 22: Western blot of miniTurbo-GFP-MAP4 RPE stable line lysates. Expression of the fusion protein was induced by doxycycline in some of the samples as indicated. Biotinylation was triggered by adding biotin to media for indicated time period. Cells were then harvested and crude cell lysates were run on PAGE. Blotted biotinylated proteins were visualized with streptavidin-HRP. Commercial biotinylated tubulin was included as a positive control (**+ctrl**; marked with asterisk). **R**, size marker.

After the verification that miniTurbo is indeed active upon biotin stimulation, we performed biotinylation using MAP6 construct which should enrich the biotinylated proteome in MIPs, compared to MAP4 as a bait protein. We induced MAP6-miniTurbo-GFP and miniTurbo-GFP-MAP4 cell lines with doxycycline and initiated the biotinylation. Cells were then lysed and biotinylated proteins were fished out by streptavidin-conjugated agarose beads. Crude lysates, fished-out biotinylated proteins, and unbound supernatant were then analysed by western blot stained with streptavidin-HRP (**Fig. 23**). Biotinylated proteins were indeed present in both cell lines in total lysates and in the fraction bound to beads. Supernatants after precipitation were depleted of the biotin signal. In mock-treated cells without biotin incubation, no biotinylation was detected.

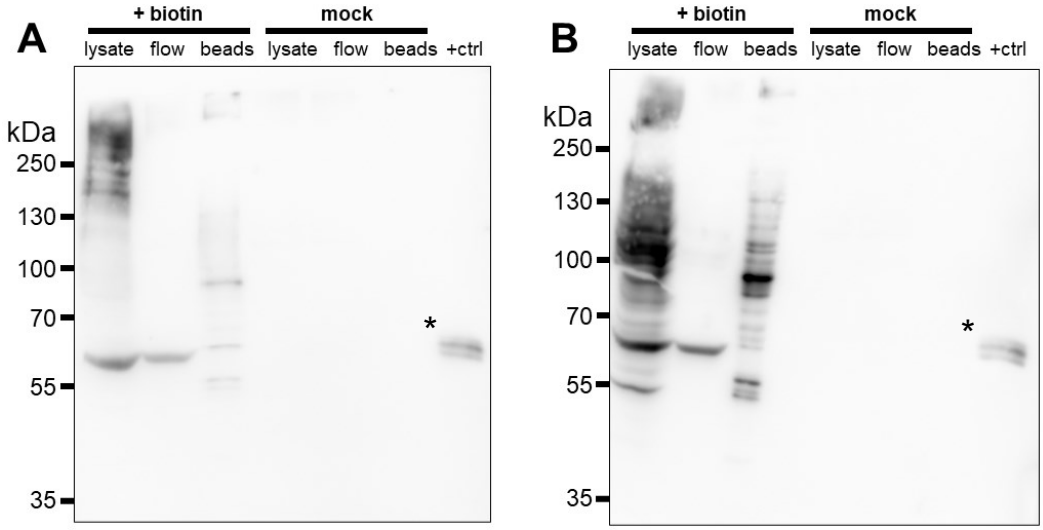

Fig. 23: Streptavidin precipitation of biotinylated proteins in RPE stable cell lines. A: miniTurbo-GFP-MAP4 line. **B:** MAP6-miniTurbo-GFP line. All cell samples were induced by doxycycline. Half of cells was incubated with biotin in media for 24 hours (**+ biotin**), half of cells was mock-treated with DMSO (**mock**). Crude lysates, flow-through of unbound lysate, and precipitated proteins on beads were run on PAGE (**lysate**, **flow**, **beads** respectively). Commercial biotinylated tubulin was included as a positive control (+ctrl, marked with asterisk).

4.1.2. Direct isolation of MTs approach

4.1.2.1. Isolation of intact MTs without depolymerization

As an alternative approach for identifying MIPs in dynamic MTs, we tried to isolate intact MTs from cultured human cell lines directly, without depolymerization in the process. For this purpose, we utilized the GFP-α-tubulin stable RPE cell line (**Fig. 24**). Using this line enabled us to easily observe MTs during the process of isolation and check on their quality. Otherwise, fluorescently-tagged docetaxel could be used for MTs visualization.

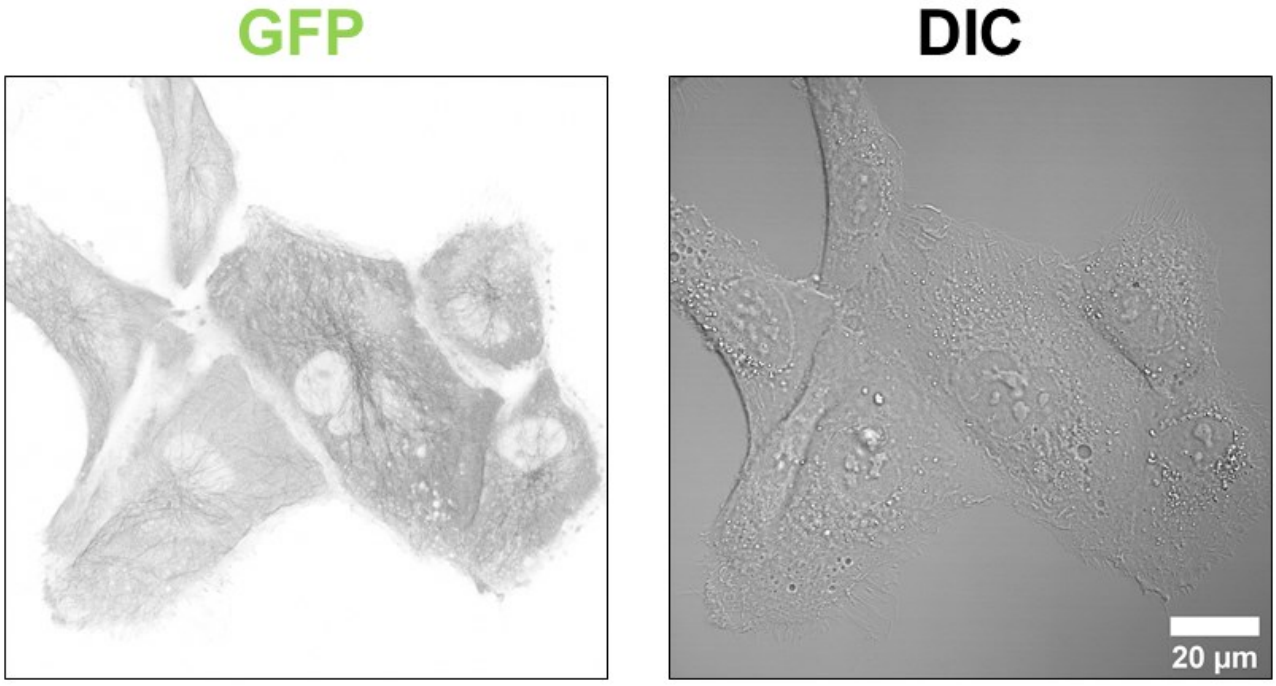

Fig. 24: GFP-α-tubulin RPE stable cell line. The expressed fusion protein localizes to MTs and cytosol, since not all tubulin dimers are in the polymerized state. Contrast: 130/255.

Prior to isolation, MTs in the cells to be harvested were pre-stabilized by paclitaxel. Cells were then detached from the cultivation plasticware by trypsin and washed. Mild lysis permeabilized the membranes but left the MTs polymerized; to maintain conditions favouring the polymerized state of MTs, samples were never chilled on ice, all buffers were of room temperature, and EGTA was supplied to chelate Ca^{2+} ions which are known to destabilized MTs both directly and via calmodulin-mediated activities (Schliwa *et al.* 1981). The lysis buffer also contained paclitaxel, GTP, and Mg^{2+} ions for MTs stabilization. Cells were lysed by NP-40 detergent. ATP was supplemented as well since it prevents protein aggregation via its hydrotropic nature (Patel *et al.* 2017). After resuspension in lysis buffer, cells were broken by mild sonication and observed on a confocal microscope. Loose MTs could be seen (**Fig. 25 A, Supplement 2**).

MTs in suspension were then immunoprecipitated on agarose beads with anti-tubulin antibody (**Fig. 25**). Beads with attached MTs were then washed in a series of steps with increasing molar concentration of the HMP buffer (80, 400, 600 mmol/l), to destabilize unspecific interactions of proteins and to detach outer MAPs from microtubules. All washing buffers contained paclitaxel to prevent depolymerization of MTs. We hypothesised that MIPs should remain trapped inside MTs, given that the MT lattice is intact. MTs remained bound to beads even in the highest concentration of HMP used (**Fig. 25 D**). We collected samples for MS analysis along the washing procedure with increasing molar concentration to elucidate which proteins detached at various buffer concentrations. The resulting proteome is currently being analysed, therefore it is not presented here.

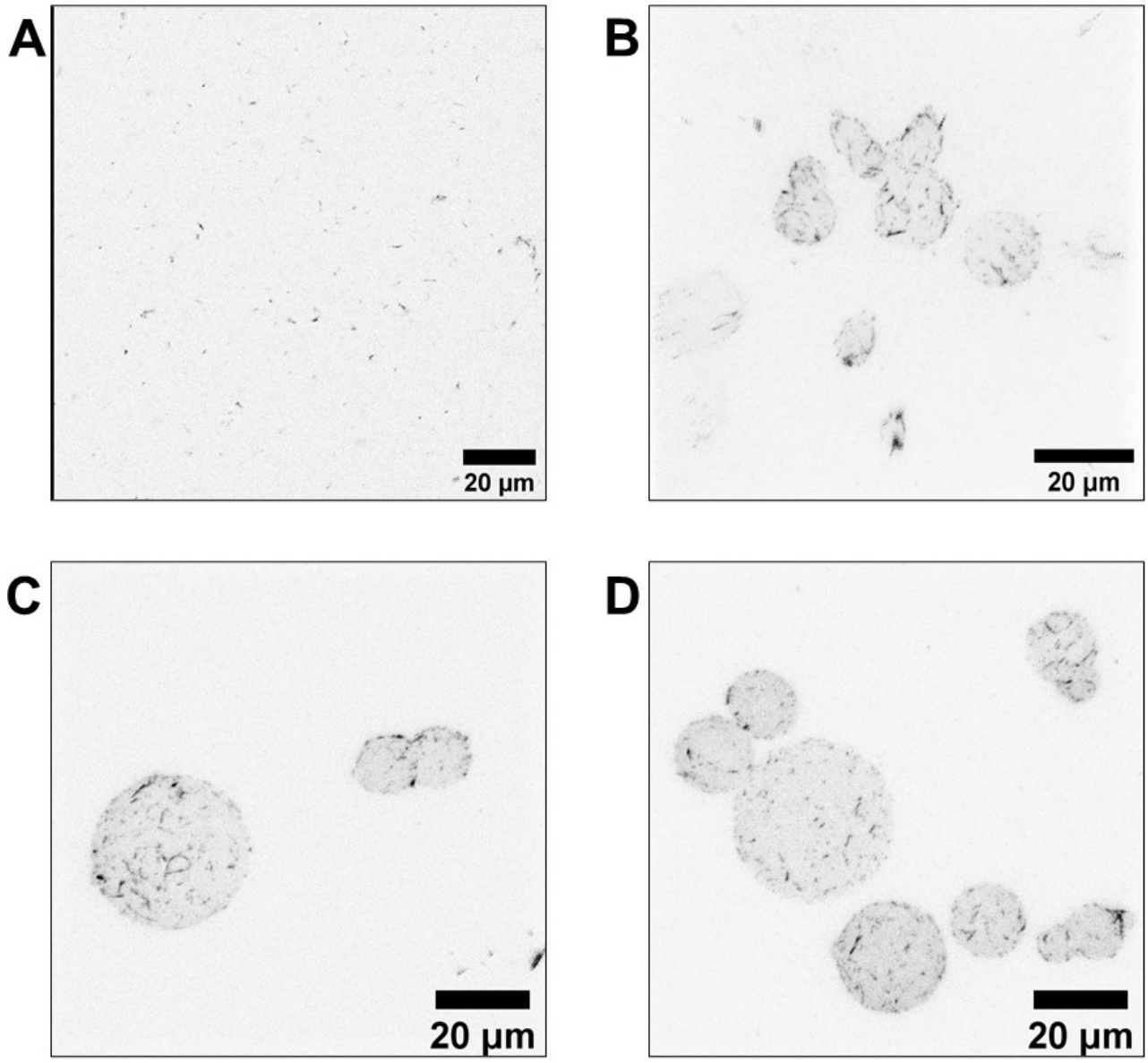

Fig. 25: Direct isolation of intact MTs from RPE GFP-α-tubulin stable cell line. GFP signal is shown in all panels. **A:** MTs after lysis of cells by detergent and sonication. **B:** MTs attached to beads with anti-tubulin antibody after BRB80 wash. **C:** MTs attached to beads after HMP400 wash. **D:** MTs attached to beads after HMP600 wash. Contrast: **A** 200/255, **B** 60/255, **C** 60/255, **D** 60/255.

4.1.2.2. Isolation of MTs polymerized in cell lysate

Besides experiments aiming to isolate intact MTs without depolymerization, we also explored the possibility to induce polymerization of MTs in concentrated cell lysate and isolate those. Highly concentrated cell lysate might resemble the cytoplasmic environment so that entry of MIPs to MTs would take place. MTs polymerized in the lysate were longer than intact isolated MTs (**Fig. 26 A**).

For polymerization of MTs in cell lysate, RPE cells were harvested and lysed in lysis buffer. Thorough sonication on ice followed to properly break all cells. Insoluble structures and debris were spun down and discarded, the supernatant was supplied with GTP and MTs were let to polymerize at 37 °C. Subsequent immunoprecipitation was the same as for intact MTs isolated from cells (**Fig. 26 B**, **C**). Again, samples were taken along the washing procedure for MS to assess detaching of bound proteins caused by high salt concentrations. The resulting proteome is currently being analysed, therefore it is not presented here.

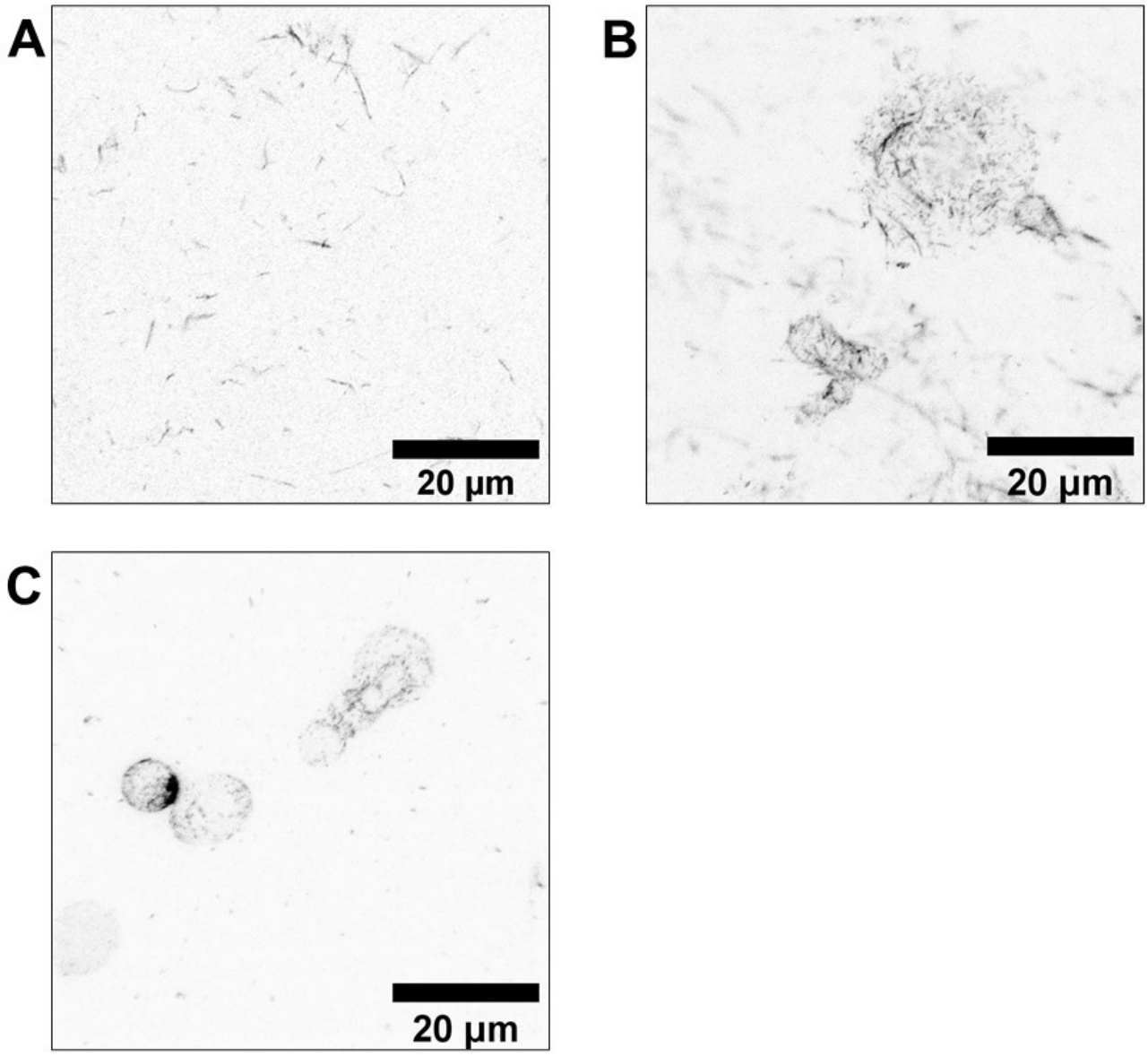

Fig. 26: MTs polymerized in RPE GFP-α-tubulin stable cell line lysate. GFP signal is shown in all panels. **A:** MTs after polymerization in lysate. **B:** MTs attached to beads with anti-tubulin antibody after BRB80 wash. **C:** MTs attached to beads after HMP600 wash. Contrast: 100/255 in all subpanels.

4.2. MIPs in axonemal MTs (TAILS complex)

In the second part of this thesis, we aimed to identify the protein constituent(s) of the TAILS complex in sperm cells. We selected the bull as the model animal since bull sperm is readily available in large quantities and is known to contain TAILS in the tip (Zabeo 2021). Our approach for obtaining the sperm cell tip proteome was IF labelling of sonicated sperm cells and subsequent enriching for tip fragments on a flow cytometry sorter.

4.2.1. Obtaining sperm tip proteome using FACS

Bull sperm cells were stained with anti-tubulin (axonemal marker) along with anti-DCDC2C (tip marker) primary antibodies, followed by secondary fluorophore-conjugated antibodies and DAPI (head marker). Cells were then sonicated to detach the flagellum from the head and break it into fragments. FACS was then used to sort out tip-containing fragments (tubulin and DCDC2C positive) and the rest of the fragments from the flagellum (tubulin positive, DCDC2C negative). Heads and unbroken sperm cells were discarded (DAPI positive). Tip-enriched and tip-depleted samples were analysed by MS and their proteomes were then obtained. A graphic summary of this approach is shown in **Fig. 27**.

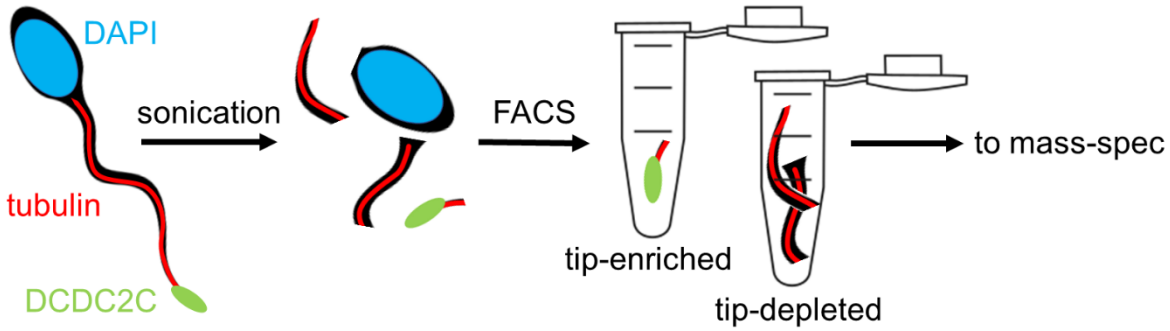

Fig. 27: Schematic outline of immunofluorescence & FACS approach for generating sperm tip proteome. Comment is in the main text.

4.2.1.1. Flagellum tips from bull sperm cells were sorted using FACS.

We aimed to develop a protocol for a strong IF labelling of tubulin and DCDC2C protein. This goal was fulfilled partially, as DCDC2C staining was optimal, but tubulin was labelled to a low extent (**Fig. 28**). However, this suboptimal stain was sufficient for generating a tip enriched fraction using FACS.

In the FACS gating strategy (**Fig. 29**), DAPI-positive events (heads and intact sperm cells) were first gated out. The DAPI-positive fraction was clearly distinguishable since the DAPI stain was strong and highly specific for DNA in the nuclei. Neither tubulin nor DCDC2C labelling produced an unequivocal positive fraction. DAPI-negative fragments were then gated in for tubulin signal (green light emission channel). All tubulin-positive fragments were finally gated into DCDC2C-positive and DCDC2C-negative fractions, which were subsequently sorted into two tubes. Other fragments were discarded. The cytometric data from sorting are displayed in **Fig. 29**. ~5.9 × 10^6 fragments were collected in tip-enriched fraction (~6 ml of suspension). ~12 × 10^6 fragments were collected in tip-depleted fraction (~12 ml of suspension).

Fig. 28: Final IF labelling experiment on bull sperm preceding the FACS. Tubulin labelling was unsatisfactory, DCDC2C labelling sufficed. Cells were sonicated and stained with DAPI afterwards. Tubulin antibody: TAT1 anti α-tubulin. Secondary antibodies: DAM DL488, GAR cy3. Contrast: 0–255 for both channels.

4.2.1.2. Collected samples were pelleted and checked on fluorescent spectrophotometer.

Fractions collected by FACS were too diluted to be processed further directly. Fractions had to be centrifuged first in an ultracentrifuge. ~200 µl of PBS was left for pellet resuspension.

To confirm that the sorted fractions are indeed either depleted or enriched in tip fragments, we measured their emission spectra using fluorescent spectrophotometer. The resulting spectra are shown in **Fig. 30**. Both sorted samples showed peaks of emission for both fluorophores used in IF labelling. Tip-enriched fraction had a relatively stronger emission of cy3 fluorophore coming from the DCDC2C signal. The ratios of emission intensity in green/red peaks was calculated – they were 5.22 and 6.90 for tip-enriched and tip-depleted fractions, respectively. Before sending for MS analysis, samples were decrosslinked by heat which induces the decomposition of methylene bridges (Kennedy-Darling & Smith 2014).

4.2.1.3. Tip-enriched proteome had DCDC2C among other hits.

Both sorted fractions (tip-enriched and tip-depleted) were sent to MS analysis at EMBL proteomics core facility, Heidelberg, Germany. In total, 844 unique proteins were detected, out of which 44 were marked as hits with at least two-fold enrichment in the tip proteome. Hits identified with only two unique peptides were excluded, generating the final list of 26 proteins. Importantly, DCDC2C itself was marked as a hit, indicating that the tips were indeed concentrated successfully. The list of hits is shown in **Table 9** without any further manual curation.

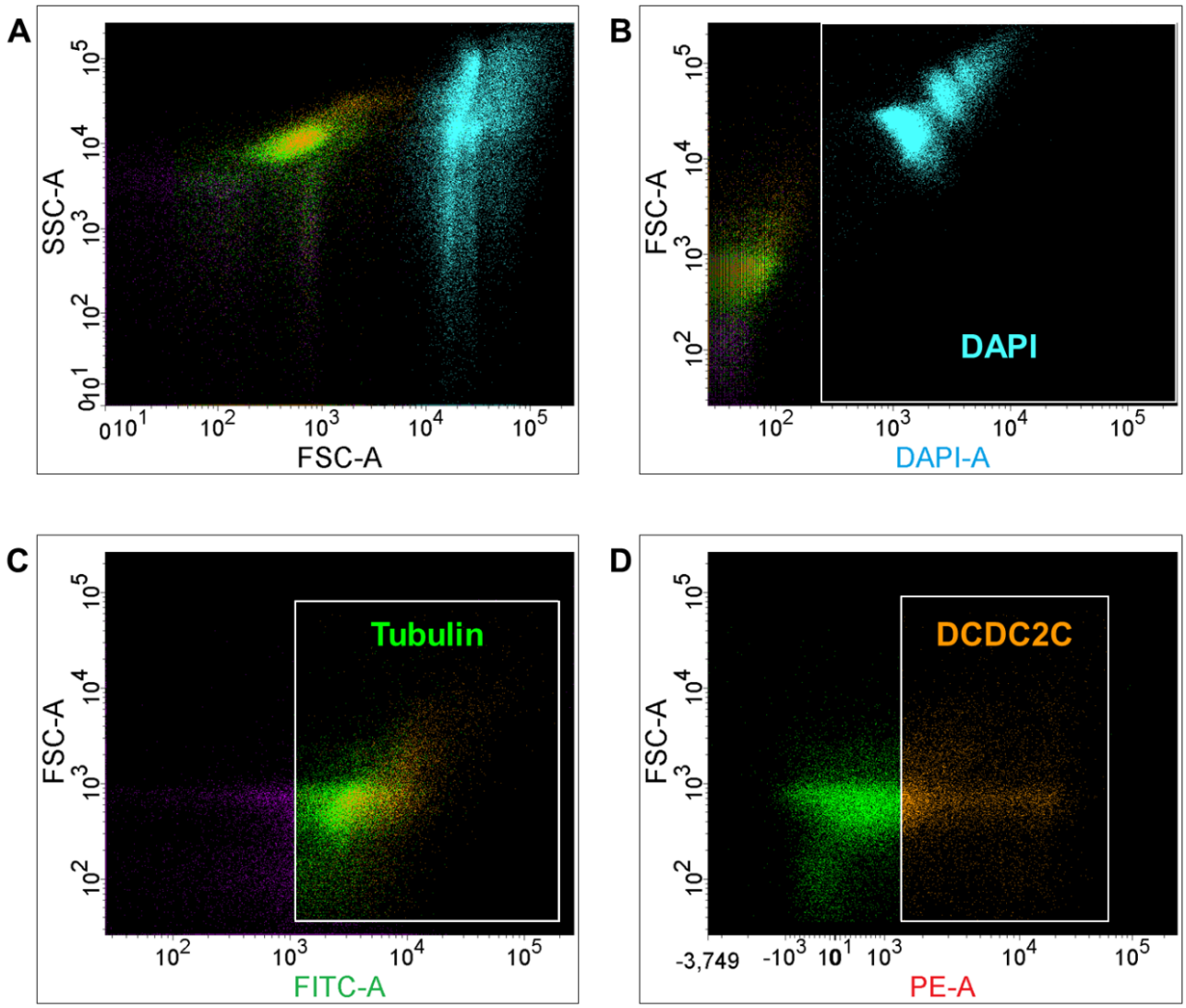

E

Population	#Events	%Parent	%Total
All Events	110,000	####	100.0
DAPI	51,046	46.4	46.4
NOT(DAPI)	58,954	53.6	53.6
Tubulin	29,130	49.4	26.5
DCDC2C	9,267	31.8	8.4
NOT (DCDC2)	19,863	68.2	18.1

Fig. 29: Sorting of labelled frozen bull sperm fragments from IF labelling on Fig. 28. A: Dot plot of forward scatter, area of peak (FSC-A) against side scatter, area of peak (SSC-A). **B:** Dot plot of DAPI signal against forward scatter. Gate-out area of DAPI-positive fragments is shown (light blue points). Points outside constitute the NOT(DAPI) fraction (purple). **C:** Dot plot of tubulin signal (FITC-A) against forward scatter. Gate-in area of tubulin-positive fragments is shown (green points). **D:** Dot plot of DCDC2C signal (PE-A) against forward scatter. Gate-in are of DCDC2C-positive fragments is shown (orange points). DCDC2C (tip-enriched) and NOT(DCDC2C) (tip-depleted) fractions were sorted. **E:** Gating strategy. Number of events, share on mother fraction in %, and share on total number of events in % are listed for each gated fraction. A subset of 110,000 events from the sorted sample is shown.

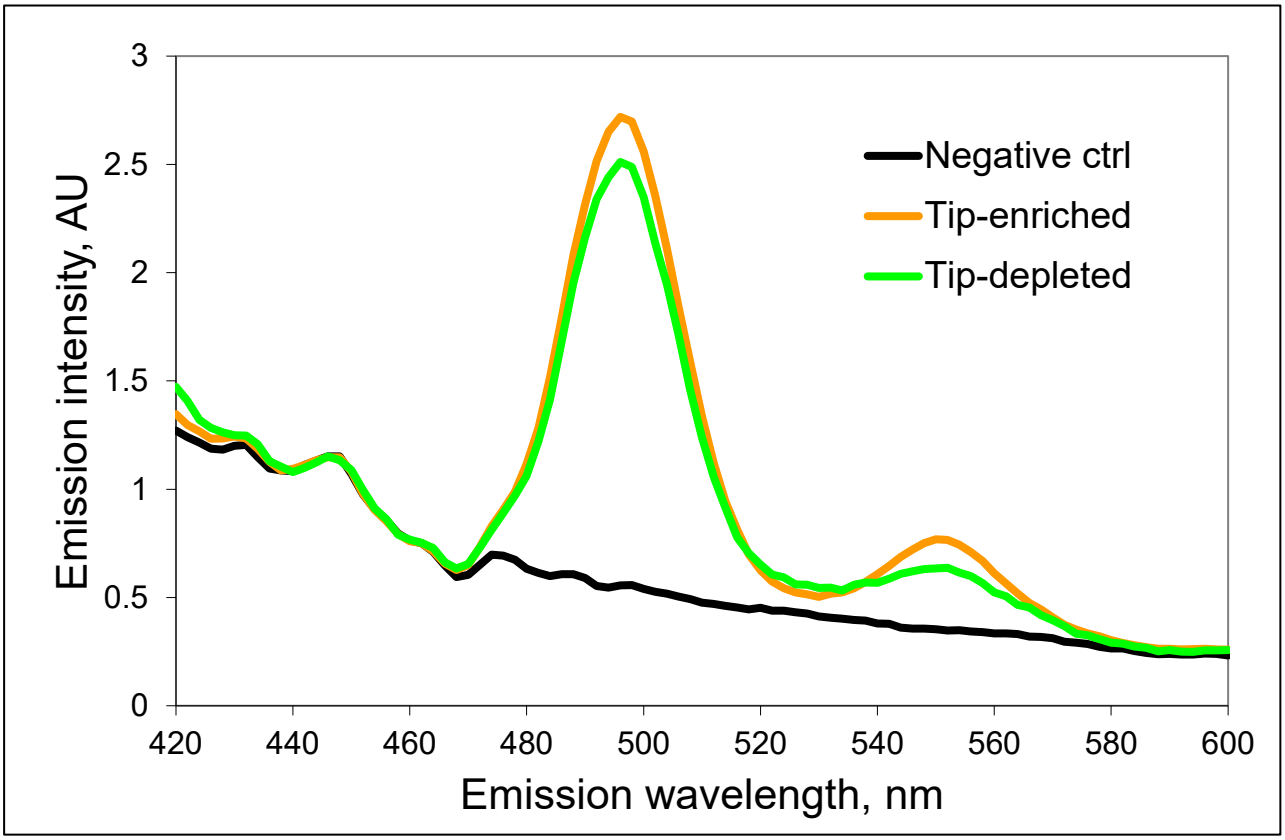

Fig. 30: Emission spectra of sorted fractions measured on fluorescent spectrophotometer. Synchronous spectra with wavelength distance of 20 nm were used. Two distinct peaks of emission are observable in both sorted fractions. Unstained sonicated sperm cells were used as a negative control. AU, arbitrary units.

Table 9: List of hits from MS analysis of FACS-generated tip-enriched proteome. Proteins are listed in alphabetical order.

UniProt gene name	UniProt protein name
ACTL7B	Actin-like protein 7B
ATP6V1A	V-type proton ATPase catalytic subunit A
CBY2	Isoform 2 of Protein chibby homolog 2
CCDC166	Coiled-coil domain containing 166
CCT8	T-complex protein 1 subunit theta
CLTC	Clathrin heavy chain 1
DCDC2C	Doublecortin domain containing 2C
DNAI4	WD repeat domain 78
EEF1G	Elongation factor 1-gamma
GRK3	G protein-coupled receptor kinase
HSP90AA1	Heat shock protein HSP 90-alpha
HSP90AB1	Heat shock protein HSP 90-beta
HSP90B1	Endoplasmin
HSPA5	Endoplasmic reticulum chaperone BiP
LOC523503	Alpha-mannosidase
PDIA3	Protein disulfide-isomerase A3
PPP2CB	Serine/threonine-protein phosphatase 2A catalytic subunit beta isoform
PSMC5	26S proteasome regulatory subunit 8
PSMC6	26S proteasome regulatory subunit 10B
PSMD11	26S proteasome non-ATPase regulatory subunit 11
PSMD12	26S proteasome non-ATPase regulatory subunit 12
RAB42	Uncharacterized protein
TPP2	Tripeptidyl-peptidase 2
TSKS	Testis specific serine kinase substrate
UCHL1	Ubiquitin carboxyl-terminal hydrolase isozyme L1
YWHAE	14-3-3 protein epsilon

5. Discussion

This diploma thesis aimed to identify new MIPs in dynamic MTs in the cytoplasm and in stabilised MTs of the axoneme (particularly the members of the TAILS complex in sperm cells). In the dynamic MTs project, we utilized proximity labelling by BioID, or alternatively, we isolated MTs directly from cells. For the TAILS project, we aimed to analyse the flagellar proteome with TAILS members being enriched by IF labelling and cytometry sorting. Both approaches then generated a list of proteins identified by MS with MIPs being possibly enriched in them (only TAILS proteome is included in this thesis; proteomic analysis of MS data from dynamic MTs has not been completed yet).

5.1. "Dynamic" and "axonemal" MTs

We discerned dynamic (cytosolic) and axonemal (stabilized) MT categories in this thesis, which is necessarily a simplistic and arbitrary categorization. After detailed scrutiny, cytoplasmic MTs show heterogeneity e. g. in terms of their resistance to depolymerization-inducing drugs like nocodazole (Baas *et al.* 1993), or resistance to cold-induced depolymerization (Guillaud *et al.* 1998). Also, the dynamic behaviour differs in individual MTs in one cell (Webster & Borisy 1989). Another issue is that the axoneme is technically part of the cytoplasm, too, since it is continuous with the cytoplasmic membrane and the bulk volume of the cell. Nevertheless, the entry of molecules to the cilium is at least partially controlled by permeability barriers (Kee *et al.* 2012), similarly to the nuclear pore complexes restricting entry of molecules to the nucleus; reviewed in (Verhey & Yang 2016). Thus, it can be argued that the ciliary volume is restricted and contains "cilioplasm" rather than cytoplasm (Jin *et al.* 2014), analogous to nuclear "nucleoplasm". A review (Ichikawa & Bui 2018) distinguishes similar categories of "cytoplasmic" and "central pairs + doublets (axonemal)" MTs as we do here.

The best characteristic describing the "axonemal MTs" would probably be their precise organization into a defined assemblage, i. e. the axoneme with firmly set architecture and repeat length (Oda, Yanagisawa, Kamiya, *et al.* 2014). The organization of the axoneme is looser in primary cilia (Kiesel *et al.* 2020), but still well-defined at least in the proximal part. "Dynamic MTs", on the other hand, lack this organization, and the positions in the cell, numbers, and repeat length of "dynamic MTs" are not predetermined. Axonemes are thus easier to study by cryo-EM techniques because the regular repetition of structural features facilitates the averaging and masking used during computing 3D models from raw EM data (reviewed in (Castaño-Díez & Zanetti 2019)). Densities without strict periodicity would be averaged out in 3D reconstructions of MTs (Wang *et al.* 2021).

5.2. MIPs in dynamic MTs: BioID approach

Our endeavour to identify candidates for new MIPs in dynamic MTs was split into two independent approaches (BioID approach and direct isolation approach) to increase our chances to succeed. The BioID approach is discussed in this subchapter.

5.2.1. Biotinylation by miniTurbo biotin ligase

BioID method exploits biotin ligase enzyme (originally BirA* variant was being used), which is engineered to prematurely release its product, biotinoyl-5'-AMP (Roux *et al.* 2012). This labile form of biotin moiety leaves the active site of the enzyme and reacts rapidly with primary amino groups of proteins (lysines or N-termini) yielding a covalent biotin label on the proteins vicinal to the ligase. Proteins with the biotin label are in turn purified by the immense affinity of biotin to streptavidin (Weber *et al.* 1989). The localization of the biotin ligase in the cell is manipulated by a fused bait protein. Among other proximity labelling assays, BioID holds several advantages, as summarized in (Varnaitė & MacNeill 2016): Most importantly, BioID does not require direct interaction between the bait and the sought protein. Vicinal but noninteracting proteins can be labelled as well if they fall into the radius of labelling (~10 nm for BirA* variant) (D. I. Kim *et al.* 2014).

A newly published miniTurbo variant of promiscuous biotin ligase is superior in enzymatic and structural parameters (Branon *et al.* 2018). Specifically, it biotinylates faster, has lower biotinylation background (although endogenous biotinylation background still applies (Grant *et al.* 2019)), and the molecular weight is only 28 kDa, compared to 35 kDa of BirA*. A smaller tag is desirable in our case since the luminal entry to MTs is limited by the size of the protein entering (Nihongaki *et al.* 2021). The labelling radius of miniTurbo can span up to ~35 nm, but this length can be tuned by changing the duration of the labelling (May *et al.* 2020). Thus, we used miniTurbo as the biotin ligase for BioID experiments. MiniTurbo (or similar variant TurboID) have been already used in many proteomic studies – labelling proteins of mitochondrial matrix (Haorong Li *et al.* 2021), exploration of interacting proteins in an extraribosomal complex in yeast (Larochelle *et al.* 2019), or proteomic analysis of rare cell types in *Arabidopsis* (Mair *et al.* 2019).

We probed the dependency of biotinylation on time only superficially. It was shown (for TurboID enzyme variant, similar to miniTurbo) that labelling time windows as short as 10 min can be sufficient for protein identification on MS (Branon *et al.* 2018). Although we detected biotinylated proteins after 10 minutes of biotinylation as well, we performed the streptavidin pulldown on samples biotinylated for 24 hours. Prolonged biotinylation ensured that enough signal could be detected on western blots after streptavidin pulldown. Optimization of the method was therefore easier.

Of course, longer biotinylation leads to lower specificity compared to a shorter biotinylation window (Branon *et al.* 2018). The reason is that amino groups in the surroundings are saturated after some time with biotin labels so that biotinoyl-5'-AMP diffuses further before it encounters a free amino group to react with. More distant proteins are then biotinylated, especially for the miniTurbo and TurboID variants which are immensely efficient (May *et al.* 2020). For this reason, the presented experiments serve as a proof of principle only, shorter biotinylation window is needed to produce a more specific list of hits potentially enriched in MIPs. Furthermore, MAP6 and MAP4 bait proteins are separated only by the MT wall, which is penetrable by biotinoyl-5'-AMP through fenestrations between tubulin dimers (given that biotinoyl-5'-AMP (573.5 Da) is in a similar size range as paclitaxel (853.9 Da) which can penetrate (Nogales *et al.* 1999)). MiniTurbo located on the outer surface of MTs can thus possibly biotinylated MIPs as well, although such control is still thought to be better than sole miniTurbo with cytoplasmic localization (Larochelle *et al.* 2019). Careful design of biotinylation time is thus needed to avoid saturation of target moieties for MAP4-fused miniTurbo.

5.2.2. Localization as the crucial parameter in BioID experiments

5.2.2.1. Localization of αTAT1 vectors

The key factor for BioID experiments is to ensure that the bait protein (αTAT1 and MAP6 in our case) provides a correct localization of the biotin ligase (K. F. Cho *et al.* 2020). Improper localization might lead to proteomes contaminated by proteins located in unrelated organelles. This emerged as the weak spot of this approach, since αTAT1 – even though described as a MIP in several works – completely lacked microtubular localization in all tested vectors, regardless of N- or C-terminus position and linker presence (**Fig. 21**). αTAT1 is known to localize to MTs, as well as to the nucleus in a cell-cycle dependent manner (Nekooki-Machida *et al.* 2018). In neurons, αTAT1 colocalizes with MTs to a high extent (Kalebic, Martinez, *et al.* 2013). On the other hand, Friedman *et al.* published the expression of GFP-αTAT1 in mouse embryonic fibroblasts with prominent signal in the nucleus and negligible signal on MTs (Friedmann *et al.* 2012). Also, Shida *et al.* showed expression of αTAT1 (with the sequence identical as used in this thesis) in hTERT-RPE cells with diffuse cytoplasmic and nuclear localization (Shida *et al.* 2010).

We cannot rule out the possibility that the correct localization of expressed αTAT1 fusion proteins was masked by the stronger cytoplasmic signal because of overexpression. (Shida *et al.* 2010) published data supporting this hypothesis – αTAT1 overexpression elevated the K40 acetylation levels without visibly localizing to MTs. The hypothesis might be further tested by mildly permeabilizing the cells during acquisition and observing changes in signal patterns. Such an approach was used to visualize fluorescent protein entry to the lumen of MTs by molecular trap (Nihongaki *et al.* 2021). One should be careful while using BioID in detergent-treated cells, though, because detergents are

known to disrupt MTs and affect the proteins binding to them (Witman, Carlson, Berliner, *et al.* 1972).

5.2.2.2. Localization of MAP6 vectors

MAP6 in our hands localized better to MTs than αTAT1 vectors (**Fig. 21**). Fused miniTurbo with MAP6 at the N-terminus showed MT localization, although incomplete (or even marginal in the case of MAP6-GFP vector). Initially, we only cloned the vectors with MAP6 at the C-terminus, but these vectors did not ensure localization to MTs. After this failure, we designed and cloned the N-variants which included protein linkers between MAP6, miniTurbo, and GFP. Short oligopeptide linkers can help to sterically separate linked domains and prevent structural clashes (reviewed in (Chen *et al.* 2013)) and the length of 5 residues suffice to isolate linked domains and enhance protein functionality (Zhao *et al.* 2008). Either the N-terminal position or the introduced linkers between individual proteins helped to maintain correct localization to MTs. MAP6 protein is mostly disordered (no structure has been published so far and predictions show low probabilities of secondary structures, as seen in the UniProt database ('UniProtKB - Q96JE9 (MAP6_HUMAN)' 2021)), so the effect of other proteins fused with MAP6 sequence is hard to infer. Similar problems were highlighted in a large study on protein localization which employed N- and C-terminal tagging by fluorescent proteins and analysed inflicted distortions in localization of >800 mammalian proteins (Stadler *et al.* 2013). The authors observed frequent mislocalization for both N- and C-terminal tagging. Generally, tagging by fluorescent or other probes is feasible and widely used for MAPs, consulting with literature and testing of several variants are unavoidable steps in expression vectors preparation, as summarized in (Goodson *et al.* 2010).

Although localizing to MTs, the most promising MAP6-miniTurbo-GFP vector also localized to the Golgi apparatus. This localization is maintained by N-terminal palmitoylation (Gory-Fauré *et al.* 2014). To further increase the ratio of expressed MAP6-miniTurbo-GFP protein localizing to MTs, three N-terminal cysteines which are targeted by the palmitoylation PTM could be mutated. This might result in a biotinylated proteome more specific for MIPs with fewer off-targets from other cellular compartments. Alternatively, a MAP6 fragment including residues 90–177 was shown to be sufficient to bind MTs without other cellular localization (Lefèvre *et al.* 2013). However, luminal localization of MAP6 was shown only for the whole protein (Cuveillier *et al.* 2020) and one cannot simply infer that any fragment of MAP6 co-localizing with MTs is automatically binding to the MT lumen.

5.3. MIPs in dynamic MTs: Direct isolation approach

5.3.1. Isolation of MTs without depolymerization

Direct isolation of MTs was our alternative approach to identify MIPs in dynamic MTs. In commonly used tubulin isolation protocols, MTs undergo repeated rounds of depolymerization by cold (Borisy *et al.* 1975, Vallee 1982). Repolymerization of tubulin is easily achievable by supplementing paclitaxel, MT-stabilizing and polymerization-promoting drug (Schiff *et al.* 1979). MAPs can repeatedly reassociate with repolymerized MTs (Vallee 1982) because the outer surface is available from the solution. MIPs, however, need to overcome the barrier of the tubulin lattice for binding to the interior (Nihongaki *et al.* 2021), and we hypothesize that their dissociation and repeated binding is limited compared to MAPs. Therefore, we had to develop a protocol for MTs isolation without any depolymerizing steps.

Paclitaxel was a key component of our isolation protocol for its ability to stabilize MTs and prevent depolymerization. Paclitaxel was initially thought not to affect the binding of MAPs (Vallee 1982) in isolation experiments, but recent works using cryo-EM techniques prove that paclitaxel changes the structure and increases the flexibility of MT lattice (Kellogg *et al.* 2017), even the number of protofilaments might be altered (J F Díaz *et al.* 1998). Furthermore, paclitaxel can reduce the affinity of MAPs towards MTs, as shown for MAP4 (Xiao *et al.* 2012) or tau protein (Kar *et al.* 2003). The

same might be true for MIPs, especially since the taxanoid binding site is facing the luminal side (Nogales *et al.* 1999). By using paclitaxel for stabilizing MTs, we pay the price of some MAPs or MIPs being possibly lost. Kellog and colleagues suggest that non-hydrolysable analogues of GTP might be a better alternative to paclitaxel. We might employ different ways of MT stabilization in our future experiments if the paclitaxel-induced conformational change in the lattice becomes an issue.

During the washing steps which followed after immunoprecipitation of MTs, we used increasing salt concentrations (80, 400, and 600 mmol/l) which are known to induce MAP detaching (Vallee 1982). Provided the isolated MTs were long enough and with a minimal number of lattice defects, MIPs could have stayed trapped inside the lumen (either still bound to or detached from the lattice). 400 mmol/l salt concentration is sufficiently high to induce MAPs dissociation from MTs (concentration of 350 mmol/l is reported by (Sloboda 2015) and (Vallee 1982) to detach MAP1 and MAP2). Given the diverse concentrations used for MAP extraction ((Orbach & Howard 2019) used 500 mmol/l for axonemal MAPs, for instance), we included the 600 mmol/l salt concentration as an extra fail-safe step. MTs remain unperturbed by this salt concentration because values as high as 1 mol/l were successfully used to strip off MAPs (Akella *et al.* 2010).

For the isolation, we employed the GFP-α-tubulin stable cell line which enables easy visualization of MTs. As an alternative, fluorescently labelled paclitaxel or similar drug docetaxel can be used. In this case, the label serves as the stabilizing agent at the same time. We have tested this possibility, but the labelling had lower reproducibility compared to GFP-α-tubulin (data not shown). There is a theoretical possibility of MIPs/MAPs being affected by the fused GFP domain to tubulin. We observed no changes in the MT network in the GFP-α-tubulin line compared to wild-type cells, as visualized by IF labelling (data not shown). Similar tagging was for example used by (Nihongaki *et al.* 2021), too, also without any deleterious effects on MTs. GFP-α-tubulin is widely accepted as a valid approach to visualize MTs without serious perturbations in MT dynamics or MAP binding patterns, as reviewed in (Goodson *et al.* 2010). Also, our GFP-α-tubulin cell line expresses endogenous untagged α-tubulin along with the tagged one, so MTs contain a mixture of these two. This further decreases the potential for adverse effects caused by the GFP tag.

5.3.2. Isolation of MTs polymerized in cell lysate

In case the isolation of MTs without depolymerization would have failed, we engaged in modified isolation experiments using MTs polymerized in concentrated cell lysate. Cells were first harshly lysed by detergent and sonication and debris was removed by centrifugation. Cleared supernatants were left at 37 °C to polymerize MTs with GTP and paclitaxel supplied. We hypothesised that the lysate might maintain the ability to assemble MTs with MIPs present inside. This assumption is supported by several works showing MIP entry by co-polymerization with tubulin *in vitro*: e. g. (Cuveillier *et al.* 2020) for MAP6, (Kirima & Oiwa 2018) for axonemal MIP called FAP85. The treatment after polymerization, i. e. immunoprecipitation and washing with high ionic strength buffers, was the same as for intact MTs from cells. Once we obtain the MS data, we plan to compare them to the data obtained from the direct isolation of MTs without depolymerization and reevaluate whether polymerization in lysate can serve our purposes.

5.4. MIPs in axonemal MTs (TAILS complex)

The TAILS complex has been discovered very recently in human sperm cells by the group of Johanna Höög (Zabeo *et al.* 2018). TAILS has the form of an intraluminal interrupted helix at the distal terminus of axonemal MTs (in the tip). This discovery might be considered surprising, since mammalian sperm cells have been studied thoroughly for centuries, especially by microscopists (Birkhead & Montgomerie 2009). Clearly, it is worth investigating even well-studied models when modern techniques (cryo-EM in this case) are being used.

The TAILS complex has been described structurally in low resolution only so far, virtually all other knowledge (like protein composition, function, associated pathologies etc.) is missing.

Identifying at least one of the members of this complex would immensely boost the research of TAILS since it would enable *in vitro* studies and knock-out characterization. A call for identifying MIP identities was communicated by several scientists in the field, e. g. in the review of (Ichikawa & Bui 2018).

This thesis had identification of TAILS members as one of its goals. To do so, we generated a list of proteins enriched in the tip of bull sperm cells, which should therefore include TAILS members as well. Such a list has not been obtained before for mammalian cells to our knowledge.

5.4.1. IF labelling of bull sperm cells

IF labelling of is a vital step for all FACS applications (Tung *et al.* 2007, Cossarizza *et al.* 2017). In our case, weak staining would lead to a low catch rate of tips, so that the sorting would take inadequately long to accumulate enough material. On the other hand, unspecific overstain would lead to contaminated sorted fractions and a non-representative, misleading list of hits on MS. Thus, we devoted significant time to the optimization of the IF labelling protocol.

5.4.1.1. DCDC2C IF labelling

The key protein enabling FACS to be used for tip enrichment is DCDC2C. It was discovered to localize exclusively to flagellum tips (Jumeau *et al.* 2017). Importantly, a polyclonal antibody against DCDC2C is available, making IF labelling possible.

DCDC2C antibody labelling was in our hands reliable and specific in nearly all experiments executed. In the early optimization attempts, a second bleak staining spot labelled with DCDC2C rarely appeared at the base of the flagellum. This second spot could be merely stemming from unspecific overstaining of the sample since it was not observed in final staining protocols with lower background signal. Another (purely speculative but exciting) explanation could be that DCDC2C is indeed a member of TAILS and it constitutes a spiral MIP discovered at the base of the flagellum in tracheal ciliated cells at the same time (Greenan *et al.* 2020). Jumeau and colleagues published IF labelling data which contain a similar pattern in one cell as we observed (Jumeau *et al.* 2017). The enrichment of DCDC2C in the tip compared to the distal parts of the flagellum revealed by MS speaks against, though. A definitive answer will require the identification of the proteins constituting both the TAILS and basal body crescent MIP.

5.4.1.2. Tubulin IF labelling

Tubulin IF labelling was used to mark the whole length of the axoneme to gate it in. Tubulin stain could have been omitted in theory, but double staining for tip fragments improved the purity of the fraction (debris autofluorescent in only one channel could be then gated out). We initially considered this tubulin-less setup combined with gating based on FSC and SSC signal – sonication produced a distinctive cloud of flagellum fragments seen in the FSC~SSC dot-plot, negative for DAPI (see **Fig. 29 A**). Generally, a combination of markers for gating is recommended rather than single markers (Tung *et al.* 2007), so we kept the tubulin labelling included.

Tubulin labelling of bull sperm cells was troublesome and required an unexpected amount of optimization. Over 25 different protocols were tested, but we did not reach satisfactory results (data not shown due to space limitations). Tubulin labelling produced a strong signal at flagellar extremities – at the tip and the base –, but the remaining length of the axoneme was labelled weakly and often non-homogenously. This pattern was probably caused by the presence of the fibrous sheath (densely-packed cylinder covering the axoneme (Young *et al.* 2016)) around the axoneme in the central part of the flagellum.

Other factors which could have played a role in suboptimal tubulin labelling were insufficient permeabilization and binding capabilities of the TAT1 antibody. TAT1 antibody could be hardly replaced by another anti-tubulin antibody, though, for it is available in large quantities required for suspension stains and FACS (thanks to the generosity of Vladimír Varga, IGM, Prague, Czech Republic). TAT1 antibody was raised in mouse against *T. brucei* α-tubulin (Woods *et al.* 1989), so altered affinity towards mammalian sperm cell tubulin could not be ruled out. Other tools for specific labelling are available nowadays, like DNA aptamers (Pu *et al.* 2015), or synthetic antibodies (sybodies) (Zimmermann *et al.* 2020), which stand out by their binding affinities and controllable

production protocol. Classical antibodies are large (~160 kDa), so they might be sterically hindered from targeting their antigen in crowded environments (Nihongaki *et al.* 2021). Thus, a sybody might have met our needs better.

Although initial experiments carried out on bull sperm stored at 4 °C yielded sufficient homogeneity and strength of tubulin signal, we had to switch to sperm stored in liquid nitrogen. Sperm stored at 4 °C quickly developed high autofluorescence of mitochondria and was spoiled by contamination outgrowth. Sperm frozen in liquid nitrogen had negligible autofluorescence and was without any observable contamination. These factors favoured frozen sperm, even though its labelling was consistently worse than that of refrigerated sperm. Frozen sperm was reported to have altered antigenic properties, compared to fresh sperm (Alexander & Kay 1977). Another work studied the effect of cryostorage on tubulin in human sperm (Desrosiers *et al.* 2006). The amount of tubulin extracted by a non-reducing buffer was higher for frozen than for fresh samples. The authors speculate that the MT structure might weaken over time even in liquid nitrogen, rendering MTs more susceptible to extraction once thawed. Such a conclusion supports our observation of deteriorated staining of MTs in thawed sperm cells. As a workaround, a different marker could be used instead of tubulin, e. g. proteins of the fibrous sheath (Young *et al.* 2016), which would not colocalize with DCDC2C at the tip, though.

During the optimization, we tested a broad array of conditions, including the type of primary and secondary antibodies, fluorophores combinations, various detergents and their concentrations, and permeabilization as a single step or during antibody labelling. Despite our suboptimal tubulin staining, we ultimately decided to proceed to FACS anyway in order not to delay the whole project.

5.4.2. FACS of IF-labelled sonicated bull sperm cells

Flagellar fragments differed substantially from usual cell samples in the terms of size and shape. For this reason, standard procedures used for cell sorting – gating in singlets from clusters and living cells from dead (Tung *et al.* 2007) – did not apply. The detection threshold which discerns events from electronic noise had to be set much lower so it could record fragments as small as 200 nm (the width of the flagellum tip (Zabeo *et al.* 2018)), which is at the detection limit of modern flow cytometers (Erdbrügger *et al.* 2014). Solutions used for IF labelling were therefore filtered or cleared by centrifugation, because any pertaining contamination by organic or inorganic particles would be recorded and therefore slow down the processing.

Compared to microscopes, FACS does not process spatial information (Cunningham 2010). Each event is assigned a single number value in each fluorescent channel, so small bright objects might have a similar fluorescence value as large dim objects. Linking distinct populations of events detected by FACS to biological structures observed in a microscope is thus intricate. The interpretation of cytometry data was further complicated by inter-experiment variability – gate setting used in one experiment could not be applied to a replicate and had to be adjusted *ad hoc* arbitrarily. Such variability could arise from a large array of reasons, illustrated by a case when replication of a cytometry experiment failed because of different agitation speeds (Hines *et al.* 2014). Imaging flow cytometry (which combines a microscope and a cytometer in one device) could have been a method of choice for understanding better how IF labelled sonicated sperm cells translated into cytometry plots, as summarized in a review (Barteneva *et al.* 2012).

5.4.2.1. Volume and amount of sorted samples

Sorting sessions were usually carried on until the whole sample volume was processed. For the negligible size of the fragments, the sorted sample appeared virtually empty when investigated using a light microscope. Tips had to be spun down in an ultracentrifuge and resuspended in much lower volume (~200 µl instead of 6 ml). This step turned out to be crucial. In several other attempts, we failed to concentrate the fragments properly. Spectroscopy measurement then showed only background noise with negligible specific signal. The whole experimental efforts then turned in vain. For these reasons, we were not able to produce replicates for the MS analysis yet.

We then verified that fractions enriched in tips had indeed a lower ratio of tubulin/DCDC2C fluorescence signal on a fluorescence spectrophotometer. We obtained a surprisingly clear spectrum (**Fig. 30**), given how little the protein content was (checked by Bradford protein assay, NanoDrop,

and Coomassie-stained PAGE, data not shown). Apparently, the light detection sensitivity of fluorescent spectroscopy is far over the sensitivity of biochemical protein detection. Also, proteins in sorted fractions were not in solution, but still part of the flagellar fragments as a suspension, which might have impacted the results.

5.4.3. MS proteomic analysis and list of hits

MS analysis of tip-enriched and tip-depleted fractions was carried out at the proteomics facility of EMBL in Heidelberg, which has sufficient instrumentation and experience to process even trace amounts of samples. The obtained proteome was based on mere two samples (one for each condition). Shall the proteome be considered robust enough to infer implications for the further course of the project, additional replicates will be necessary. The list in **Table 9** should be considered preliminary also because it accounts for statistics of the MS analysis only, not the biological relevance of individual proteins, which is yet to be assessed manually. That said, the presence of DCDC2C among hits indicates that our proteome can be attributed at least some degree of trustworthiness. Contamination by human biological material could be easily excluded from the dataset because the sperm cells originated from the bull.

5.4.4. TAILS identification project – future steps

This thesis was part of a broader project devoted to TAILS, carried out by Johanna Höög's group at the University of Gothenburg, Sweden. Currently, a 3D structural model of the TAILS complex in sperm cells is being constructed from single particle cryo-EM and cryo-EM tomography data. Previously, another tip proteome was generated (with the contribution of the author of this thesis) based on different sedimentation of flagellar fragments in sucrose ultracentrifugation gradients. More detailed analysis will be performed, hopefully, once more replicates of the FACS sorting are analysed. This analysis will include a comparison of hits with proteomes from other species by BLAST (basic local alignment search tool) – we expect the TAILS protein members to have homologues in all vertebrate species shown to possess TAILS (*Homo sapiens* (Zabeo *et al.* 2018), *Bos taurus*, *Gallus gallus domesticus*, *Xenopus tropicalis* (Zabeo 2021), *Equus ferus caballus*, *Sus scrofa f. domestica* (Leung *et al.* 2021); *Mus musculus* is surprisingly lacking TAILS (Leung *et al.* 2021)). Furthermore, proteins with homologues in species lacking TAILS (*Trypanosoma brucei* (Zabeo 2021), *Chlamydomonas reinhardtii* (Jordan *et al.* 2018)) will be excluded from further consideration.

After the completion of proteomic studies and cryo-EM 3D reconstruction, we will select a handful of best-fitting candidates for verification. First, localization will be assessed by IF labelling of sperm cells (provided antibody will be available). Then, *in vitro* experiments with MTs will be carried to see whether the protein localizes to MTs, specifically to its lumen. Finally, male patients with mutations of corresponding candidate protein will be sought – if found, 3D reconstruction of their sperm cells tips will be build to see possible distortions or absence of the TAILS complex. The long-term goal is to map known defects of human sperm motility to axonemal structural features, to deepen the knowledge of how structure translates to movement in sperm.

5.5. MIPs in microtubular research

Microtubules have been subject to thorough study since the early descriptive works using optical microscopy (Schmidt 1939) or later EM (Grigg & Hodge 1949, Fawcett & Porter 1954). New roles of MTs in cells emerged along with the continuing development of biochemical and biophysical tools. The effort devoted to MTs is immense (or even "aggressive" as described in a historical review by Brinkley (Brinkley 1997)), yet it still yields new and unforeseen knowledge gaps.

With the advent of high-resolution cryo-EM, reconstitution of (nearly) native MT assemblies and MT-related complexes become feasible. Previous structural methods, like X-ray crystallography, were of limited help since intricate complexes could not crystallize out of cellular complex purely *in vitro*. Cryo-EM techniques overcame this limitation; however, obtaining atomic resolution remains challenging in particular applications.

The progress of methods naturally links to change in prominent subfields of MT research. A glimpse at the Portfolio page dedicated to MTs of Springer Nature publishing house (www.nature.com/subjects/microtubules) gives a nice representation of what is in the mainstream of current MT research. At the time of 19th of July 2021, five top-listed articles are focused on PTMs of MTs in neurons, spindle biomechanics, MAPs recruitment to MTs, a novel MT drug, and finally, new MIPs identified via cryo-EM. This selection illustrates the trend of merging structural biology with chemistry, physics, and more and more often, neuroscience and physiology. Also, it shows that MIPs as a topic are gaining a leading position.

The luminal compartment of MTs stood away from the research interest for most of the time MTs were known to exist. Before the cryo-EM era, microscopists suggested that the lumen might serve as a transport track for tubulin dimers or other material. Burton suggested that MTs can transport their own building blocks to distal parts of the cell (Burton 1984). Slautterback hypothesized that MTs might transport water and ions like cellular pipes (Slautterback 1963). The possibility that MTs transport water or ions was ruled out when the structure of MTs lattice was revealed (Nogales *et al.* 1999). The transport hypothesis re-emerged with the observations of MIP particles by cryo-EM (Garvalov *et al.* 2006, Bouchet-Marquis *et al.* 2007). MTs were also suggested to serve as storage for proteins or RNA (Garvalov *et al.* 2006). Odde proposed that MTs can serve as vehicles for drug delivery (Odde 1998); this idea was further explored by Inaba who designed tau-derived peptides which can be encapsulated in the MT lumen (Inaba *et al.* 2018). The importance of the MT lumen as a compartment will be reevaluated once more data are collected on MIPs entry and mobility in the MT interior.

The existence of MIPs has been either ignored or too difficult to study for a long time. The first report of "full microtubules" dates as early as 1966 (observed densities, however, appear that they might have been mere artefacts of heavy metals stains) (Bassot & Martoja 1966). More convincing work by Burton was even as a whole dedicated to luminal material of MTs in frog olfactory neurons (Burton 1984). Still, MIPs gained broader interest among the research community much later, starting in 2006 when cryo-EM was used for the first time to study MIPs (Garvalov *et al.* 2006). Soon after, αTAT was shown to be the first identified MIP (Shida *et al.* 2010). Many other proteins followed, out of which the majority was in stable axonemal MTs (Ma *et al.* 2019). The only further MIP found inside dynamic MTs so far is MAP6 (Cuveillier *et al.* 2020). MIPs are a frequent phenomenon present among eukaryotic species, e. g. in the parasite *Toxoplasma gondii* (Wang *et al.* 2021). We can expect the list of MIPs to be expanded soon, along with new insights into the lumen entry mechanisms and functions performed there.

6. Conclusions

This thesis presents a pilot study of MIPs identification in our laboratory. The methods used here (namely IF labelling of sperm cells in suspension, FACS, Flp-in cell lines, biotinylation with BioID, and isolation of MTs) had to be developed *ab initio*. As a consequence, the project became mostly technical and methodological with limited output of directly useful data since many hurdles arose during the optimization (e. g. improperly localizing fusion proteins in RPE stable cell lines). Furthermore, the project outline had to be modified upon COVID-19 outburst and related restrictions of lab operation.

Our endeavours to identify new MIPs were split into two independent projects – the dynamic MTs project, and the axonemal MTs project (carried with cooperation with Johanna Höög's laboratory based in Gothenburg, Sweden). Both projects used a different set of methods and were interlinked by the topic only.

In the dynamic MTs project, we established two ways for identifying MIPs (proximity labelling by BioID, and direct isolation of MTs from cells with subsequent washing). We generated ten inducible RPE cell lines and probed two different bait proteins fused with GFP and miniTurbo biotin ligase in various combinations and arrangements. We found a combination with desired localization pattern. These cell lines can readily facilitate biotinylation experiments with a scalable level of expression without the need to repeatedly transfect cells. GFP-α-tubulin RPE stable line proved to be an invaluable tool for MTs visualization. We optimized the method of isolation of intact MTs from cells, which (at least to our knowledge), had not been reported before for dynamic MTs used for subsequent biochemical analysis. Thus, we can now isolate intact MTs directly from cells without depolymerization. We have reached the goals for the dynamic MTs part of the thesis only partially – the proteomic data of biotinylation and MTs isolation experiments have not been analysed yet and are being processed at the time of finishing the thesis.

The next steps in the dynamic MTs project will comprise optimization of the biotinylation times based on MS profiles in the BioID method. In the intact MTs isolation method, we plan to use MAP4 and MAP6 stable lines to test whether MAPs (represented by MAP4) are indeed stripped of by high salt buffers and whether MIPs (represented by MAP6) remain present in the washed MTs. Then, thorough consideration of hits will follow, and characterization of selected candidates *in vitro* and *in vivo* in the terms of localization and interaction towards MTs. Verification of candidates for MIPs was beyond the scope of the diploma project from the very beginning.

In the axonemal MTs project devoted to the TAILS complex, we successfully isolated tip fragments of the sperm cells and generated a list of candidates enriched in tips. Our developed protocol is a proof of principle that fragments with the negligible size of approximately 0.2 × 3 μm can be FACS sorted and analysed by MS. With suitable markers, it could be applied to other fragmentable biological samples to study a specific subset of the whole sample, e. g. cilia of ciliated epithelial cells, or individual organelles within cells. The goals set for the axonemal MTs part of the diploma project were met, although more replicates have to be analysed to verify the obtained list of candidates.

As summarized in the discussion, the list of TAILS candidates will be combined with previously gathered proteomic and structural data. The most promising candidate proteins for TAILS will then be tested by localization assessment using IF labelling and by *in vitro* experiments on purified components of TAILS. The group of Johanna Höög will eventually strive to transition the findings on TAILS to clinics and search for male patients suffering from sperm motility impairment stemming from defective function/structure of TAILS.

In conclusion, we generated and verified experimental tools for studying MIPs in diverse types of MTs. Our preliminary data suggest that our approaches are valid, although further experiments are needed to confirm our findings. This work can serve as a starting point for next projects devoted to the identification of MIPs.

7. List of supplements

1. Maps of plasmids used in the thesis (.pdf)
2. Intact MTs isolated from RPE GFP-α-tubulin cell line before immunoprecipitation (.mp4)

8. References

Afzelius, B.A., Dallai, R., Lanzavecchia, S. & Bellon, P.L. (1995) Flagellar structure in normal human spermatozoa and in spermatozoa that lack dynein arms. *Tissue Cell*, **27**, 241–7. doi:10.1016/s0040-8166(95)80044-1

Aguezzoul, M., Andrieux, A. & Denarier, E. (2003) Overlap of promoter and coding sequences in the mouse STOP gene (Mtap6). *Genomics*, **81**, 623–7. doi:10.1016/s0888-7543(03)00053-3

Akella, J.S., Wloga, D., Kim, J., Starostina, N.G., Lyons-Abbott, S., Morrissette, N.S., Dougan, S.T., *et al.* (2010) MEC-17 is an alpha-tubulin acetyltransferase. *Nature*, **467**, 218–22, Nature Publishing Group. doi:10.1038/nature09324

Al-Amoudi, A., Chang, J.J., Leforestier, A., McDowall, A., Salamin, L.M., Norlén, L.P.O., Richter, K., *et al.* (2004) Cryo-electron microscopy of vitreous sections. *EMBO J.*, **23**, 3583–3588. doi:10.1038/sj.emboj.7600366

Alexander, N.J. & Kay, R. (1977) Antigenicity of frozen and fresh spermatozoa. *Fertil. Steril.*, **28**, 1234–7, Elsevier Masson SAS. doi:10.1016/s0015-0282(16)42923-7

Andrieux, A., Salin, P.A., Vernet, M., Kujala, P., Baratier, J., Gory-Fauré, S., Bosc, C., *et al.* (2002) The suppression of brain cold-stable microtubules in mice induces synaptic defects associated with neuroleptic-sensitive behavioral disorders. *Genes Dev.*, **16**, 2350–64. doi:10.1101/gad.223302

Baas, P.W., Ahmad, F.J., Pienkowski, T.P., Brown, A. & Black, M.M. (1993) Sites of microtubule stabilization for the axon. *J. Neurosci.*, **13**, 2177–85. doi:10.1523/JNEUROSCI.13-05-02177.1993

Baker, T.S. & Amos, L.A. (1978) Structure of the tubulin dimer in zinc-induced sheets. *J. Mol. Biol.*, **123**, 89–106. doi:10.1016/0022-2836(78)90378-9

Barteneva, N.S., Fasler-Kan, E. & Vorobjev, I.A. (2012) Imaging flow cytometry: coping with heterogeneity in biological systems. *J. Histochem. Cytochem.*, **60**, 723–33. doi:10.1369/0022155412453052

Bassot, J.M. & Martoja, R. (1966) [Histological and ultrastructural data on the cytoplasmic microtubules of the ejaculatory canal of orthopteral insects]. *Z. Zellforsch. Mikrosk. Anat.*, **74**, 145–81. doi:10.1007/BF00399654

Bigman, L.S. & Levy, Y. (2020) Tubulin tails and their modifications regulate protein diffusion on microtubules. *Proc. Natl. Acad. Sci. U. S. A.*, **117**, 8876–8883. doi:10.1073/pnas.1914772117

Birkhead, T.R. & Montgomerie, R. (2009) Three centuries of sperm research. in *Sperm Biology*, First Edit., pp. 1–42, Elsevier. doi:10.1016/B978-0-12-372568-4.00001-X

Bitan, A., Rosenbaum, I. & Abdu, U. (2012) Stable and dynamic microtubules coordinately determine and maintain Drosophila bristle shape. *Development*, **139**, 1987–96. doi:10.1242/dev.076893

Borisy, G.G., Marcum, J.M., Olmsted, J.B., Murphy, D.B. & Johnson, K.A. (1975) Purification of tubulin and associated high molecular weight proteins from porcine brain and characterization of microtubule assembly in vitro. *Ann. N. Y. Acad. Sci.*, **253**, 107–32. doi:10.1111/j.1749-6632.1975.tb19196.x

Bosc, C., Andrieux, A. & Job, D. (2003) STOP proteins. *Biochemistry*, **42**, 12125–32. doi:10.1021/bi0352163

Bouchet-Marquis, C., Zuber, B., Glynn, A.-M., Eltsov, M., Grabenbauer, M., Goldie, K.N., Thomas, D., *et al.* (2007) Visualization of cell microtubules in their native state. *Biol. cell*, **99**, 45–53. doi:10.1042/BC20060081

Branon, T.C., Bosch, J.A., Sanchez, A.D., Udeshi, N.D., Svinkina, T., Carr, S.A., Feldman, J.L., *et al.* (2018) Efficient proximity labeling in living cells and organisms with TurboID. *Nat. Biotechnol.*, **36**, 880–887. doi:10.1038/nbt.4201

Brinkley, W. (1997) Microtubules: a brief historical perspective. *J. Struct. Biol.*, **118**, 84–6. doi:10.1006/jsbi.1997.3854

Burton, P.R. (1984) Luminal material in microtubules of frog olfactory axons: structure and distribution. *J. Cell Biol.*, **99**, 520–8. doi:10.1083/jcb.99.2.520

Caplow, M. & Fee, L. (2002) Dissociation of the tubulin dimer is extremely slow, thermodynamically very unfavorable, and reversible in the absence of an energy source. *Mol. Biol. Cell*, **13**, 2120–31.

doi:10.1091/mbc.e01-10-0089
Castaño-Díez, D. & Zanetti, G. (2019) In situ structure determination by subtomogram averaging. *Curr. Opin. Struct. Biol.*, **58**, 68–75. doi:10.1016/j.sbi.2019.05.011
Chalfie, M. & Thomson, J.N. (1982) Structural and functional diversity in the neuronal microtubules of Caenorhabditis elegans. *J. Cell Biol.*, **93**, 15–23. doi:10.1083/jcb.93.1.15
Chen, X., Zaro, J.L. & Shen, W.-C. (2013) Fusion protein linkers: property, design and functionality. *Adv. Drug Deliv. Rev.*, **65**, 1357–69, Elsevier B.V. doi:10.1016/j.addr.2012.09.039
Cheng, Y., Grigorieff, N., Penczek, P.A. & Walz, T. (2015) A primer to single-particle cryo-electron microscopy. *Cell*, **161**, 438–449, Elsevier Inc. doi:10.1016/j.cell.2015.03.050
Cho, K.F., Branon, T.C., Udeshi, N.D., Myers, S.A., Carr, S.A. & Ting, A.Y. (2020) Proximity labeling in mammalian cells with TurboID and split-TurboID. *Nat. Protoc.*, **15**, 3971–3999, Springer US. doi:10.1038/s41596-020-0399-0
Cho, Y. & Cavalli, V. (2012) HDAC5 is a novel injury-regulated tubulin deacetylase controlling axon regeneration. *EMBO J.*, **31**, 3063–78, Nature Publishing Group. doi:10.1038/emboj.2012.160
Coombes, C., Yamamoto, A., McClellan, M., Reid, T.A., Plooster, M., Luxton, G.W.G., Alper, J., *et al.* (2016) Mechanism of microtubule lumen entry for the α-tubulin acetyltransferase enzyme αTAT1. *Proc. Natl. Acad. Sci. U. S. A.*, **113**, E7176–E7184. doi:10.1073/pnas.1605397113
Cossarizza, A., Chang, H.-D., Radbruch, A., Akdis, M., Andrä, I., Annunziato, F., Bacher, P., *et al.* (2017) Guidelines for the use of flow cytometry and cell sorting in immunological studies. *Eur. J. Immunol.*, **47**, 1584–1797. doi:10.1002/eji.201646632
Creppe, C., Malinouskaya, L., Volvert, M.-L., Gillard, M., Close, P., Malaise, O., Laguesse, S., *et al.* (2009) Elongator controls the migration and differentiation of cortical neurons through acetylation of alpha-tubulin. *Cell*, **136**, 551–64, Elsevier Inc. doi:10.1016/j.cell.2008.11.043
Cunningham, R.E. (2010) Overview of flow cytometry and fluorescent probes for flow cytometry. *Methods Mol. Biol.*, **588**, 319–26. doi:10.1007/978-1-59745-324-0_31
Cuveillier, C., Delaroche, J., Seggio, M., Gory-Fauré, S., Bosc, C., Denarier, E., Bacia, M., *et al.* (2020) MAP6 is an intraluminal protein that induces neuronal microtubules to coil. *Sci. Adv.*, **6**, eaaz4344. doi:10.1126/sciadv.aaz4344
Dallai, R., Afzelius, B.A. & Witalinski, W. (1995) The axoneme of the spider spermatozoon. *Bolletino di Zool.*, **62**, 335–338. doi:10.1080/11250009509356085
David-Pfeuty, T., Erickson, H.P. & Pantaloni, D. (1977) Guanosinetriphosphatase activity of tubulin associated with microtubule assembly. *Proc. Natl. Acad. Sci. U. S. A.*, **74**, 5372–6. doi:10.1073/pnas.74.12.5372
Delphin, C., Bouvier, D., Seggio, M., Couriol, E., Saoudi, Y., Denarier, E., Bosc, C., *et al.* (2012) MAP6-F is a temperature sensor that directly binds to and protects microtubules from cold-induced depolymerization. *J. Biol. Chem.*, **287**, 35127–35138, Â© 2012 ASBMB. Currently published by Elsevier Inc; originally published by American Society for Biochemistry and Molecular Biology. doi:10.1074/jbc.M112.398339
Desrosiers, P., Légaré, C., Leclerc, P. & Sullivan, R. (2006) Membranous and structural damage that occur during cryopreservation of human sperm may be time-related events. *Fertil. Steril.*, **85**, 1744–52. doi:10.1016/j.fertnstert.2005.11.046
Díaz, J F, Valpuesta, J.M., Chacón, P., Diakun, G. & Andreu, J.M. (1998) Changes in microtubule protofilament number induced by Taxol binding to an easily accessible site. Internal microtubule dynamics. *J. Biol. Chem.*, **273**, 33803–10. doi:10.1074/jbc.273.50.33803
Díaz, José Fernando, Barasoain, I. & Andreu, J.M. (2003) Fast kinetics of Taxol binding to microtubules. Effects of solution variables and microtubule-associated proteins. *J. Biol. Chem.*, **278**, 8407–19. doi:10.1074/jbc.M211163200
Dimitrov, A., Quesnoit, M., Moutel, S., Cantaloube, I., Poüs, C. & Perez, F. (2008) Detection of GTP-tubulin conformation in vivo reveals a role for GTP remnants in microtubule rescues. *Science*, **322**, 1353–6. doi:10.1126/science.1165401
Dymek, E.E., Lin, J., Fu, G., Porter, M.E., Nicastro, D. & Smith, E.F. (2019) PACRG and FAP20 form the inner junction of axonemal doublet microtubules and regulate ciliary motility. *Mol. Biol. Cell*, **30**, 1805–1816. doi:10.1091/mbc.E19-01-0063
Erdbrügger, U., Rudy, C.K., Etter, M.E., Dryden, K.A., Yeager, M., Klibanov, A.L. & Lannigan, J.

(2014) Imaging flow cytometry elucidates limitations of microparticle analysis by conventional flow cytometry. *Cytometry. A*, **85**, 756–70. doi:10.1002/cyto.a.22494

Erickson, H.P. (1974) Microtubule surface lattice and subunit structure and observations on reassembly. *J. Cell Biol.*, **60**, 153–67. doi:10.1083/jcb.60.1.153

Eshun-Wilson, L., Zhang, R., Portran, D., Nachury, M. V., Toso, D.B., Löhr, T., Vendruscolo, M., *et al.* (2019) Effects of α-tubulin acetylation on microtubule structure and stability. *Proc. Natl. Acad. Sci. U. S. A.*, **116**, 10366–10371. doi:10.1073/pnas.1900441116

Fawcett, D.W. & Porter, K.R. (1954) A study of the fine structure of ciliated epithelia. *J. Morphol.*, **94**, 221–281. doi:10.1002/jmor.1050940202

Freedman, H., Huzil, J.T., Luchko, T., Ludueña, R.F. & Tuszynski, J.A. (2009) Identification and characterization of an intermediate taxol binding site within microtubule nanopores and a mechanism for tubulin isotype binding selectivity. *J. Chem. Inf. Model.*, **49**, 424–36. doi:10.1021/ci8003336

Friedmann, D.R., Aguilar, A., Fan, J., Nachury, M. V. & Marmorstein, R. (2012) Structure of the α-tubulin acetyltransferase, αTAT1, and implications for tubulin-specific acetylation. *Proc. Natl. Acad. Sci. U. S. A.*, **109**, 19655–60. doi:10.1073/pnas.1209357109

Gardner, M.K., Zanic, M., Gell, C., Bormuth, V. & Howard, J. (2011) Depolymerizing kinesins Kip3 and MCAK shape cellular microtubule architecture by differential control of catastrophe. *Cell*, **147**, 1092–103, Elsevier Inc. doi:10.1016/j.cell.2011.10.037

Garvalov, B.K., Zuber, B., Bouchet-Marquis, C., Kudryashev, M., Gruska, M., Beck, M., Leis, A., *et al.* (2006) Luminal particles within cellular microtubules. *J. Cell Biol.*, **174**, 759–65. doi:10.1083/jcb.200606074

Ghosh-Roy, A., Kulkarni, M., Kumar, V., Shirolikar, S. & Ray, K. (2004) Cytoplasmic dynein-dynactin complex is required for spermatid growth but not axoneme assembly in Drosophila. *Mol. Biol. Cell*, **15**, 2470–83. doi:10.1091/mbc.e03-11-0848

Gilpin, W., Bull, M.S. & Prakash, M. (2020) The multiscale physics of cilia and flagella. *Nat. Rev. Phys.*, **2**, 74–88, Springer US. doi:10.1038/s42254-019-0129-0

Goodson, H. V., Dzurisin, J.S. & Wadsworth, P. (2010) Methods for expressing and analyzing GFP-tubulin and GFP-microtubule-associated proteins. *Cold Spring Harb. Protoc.*, **2010**, pdb.top85. doi:10.1101/pdb.top85

Gory-Fauré, S., Windscheid, V., Brocard, J., Montessuit, S., Tsutsumi, R., Denarier, E., Fukata, Y., *et al.* (2014) Non-microtubular localizations of Microtubule-Associated Protein 6 (MAP6). *PLoS One*, **9**. doi:10.1371/journal.pone.0114905

Grant, M.K.O., Shapiro, S.L., Ashe, K.H., Liu, P. & Zahs, K.R. (2019) A Cautionary Tale: Endogenous Biotinylated Proteins and Exogenously-Introduced Protein A Cause Antibody-Independent Artefacts in Western Blot Studies of Brain-Derived Proteins. *Biol. Proced. Online*, **21**, 6, Biological Procedures Online. doi:10.1186/s12575-019-0095-z

Grati, M., Chakchouk, I., Ma, Q., Bensaid, M., Desmidt, A., Turki, N., Yan, D., *et al.* (2015) A missense mutation in DCDC2 causes human recessive deafness DFNB66, likely by interfering with sensory hair cell and supporting cell cilia length regulation. *Hum. Mol. Genet.*, **24**, 2482–91. doi:10.1093/hmg/ddv009

Greenan, G.A., Vale, R.D. & Agard, D.A. (2020) Electron cryotomography of intact motile cilia defines the basal body to axoneme transition. *J. Cell Biol.*, **219**. doi:10.1083/jcb.201907060

Grigg, G. & Hodge, A. (1949) Electron Microscopic Studies of Spermatozoa I. The Morphology of the Spermatozoon of the Common Domestic Fowl (Gallus Domesticus). *Aust. J. Biol. Sci.*, **2**, 271. doi:10.1071/BI9490271

Guillaud, L., Bosc, C., Fourest-Lieuvin, A., Denarier, E., Pirollet, F., Lafanechère, L. & Job, D. (1998) STOP proteins are responsible for the high degree of microtubule stabilization observed in neuronal cells. *J. Cell Biol.*, **142**, 167–79. doi:10.1083/jcb.142.1.167

Hines, W.C., Su, Y., Kuhn, I., Polyak, K. & Bissell, M.J. (2014) Sorting out the FACS: a devil in the details. *Cell Rep.*, **6**, 779–81, Elsevier. doi:10.1016/j.celrep.2014.02.021

Howes, S.C., Alushin, G.M., Shida, T., Nachury, M. V. & Nogales, E. (2014) Effects of tubulin acetylation and tubulin acetyltransferase binding on microtubule structure. *Mol. Biol. Cell*, **25**, 257–66. doi:10.1091/mbc.E13-07-0387

Hubbert, C., Guardiola, A., Shao, R., Kawaguchi, Y., Ito, A., Nixon, A., Yoshida, M., *et al.* (2002) HDAC6 is a microtubule-associated deacetylase. *Nature*, **417**, 455–8. doi:10.1038/417455a

Ichikawa, M. & Bui, K.H. (2018) Microtubule Inner Proteins: A Meshwork of Luminal Proteins Stabilizing the Doublet Microtubule. *Bioessays*, **40**, 1700209. doi:10.1002/bies.201700209

Ichikawa, M., Liu, D., Kastritis, P.L., Basu, K., Hsu, T.C., Yang, S. & Bui, K.H. (2017) Subnanometre-resolution structure of the doublet microtubule reveals new classes of microtubule-associated proteins. *Nat. Commun.*, **8**, 15035, Nature Publishing Group. doi:10.1038/ncomms15035

Igaev, M. & Grubmüller, H. (2020) Microtubule instability driven by longitudinal and lateral strain propagation. *PLoS Comput. Biol.*, **16**, e1008132. doi:10.1371/journal.pcbi.1008132

Inaba, H., Yamamoto, T., Kabir, A.M.R., Kakugo, A., Sada, K. & Matsuura, K. (2018) Molecular Encapsulation Inside Microtubules Based on Tau-Derived Peptides. *Chemistry*, **24**, 14958–14967. doi:10.1002/chem.201802617

Inoue, H., Nojima, H. & Okayama, H. (1990) High efficiency transformation of Escherichia coli with plasmids. *Gene*, **96**, 23–28. doi:10.1016/0378-1119(90)90336-P

Ishikawa, T. (2017) Axoneme Structure from Motile Cilia. *Cold Spring Harb. Perspect. Biol.*, **9**, 1–16. doi:10.1101/cshperspect.a028076

Ittner, L.M. & Götz, J. (2011) Amyloid-β and tau--a toxic pas de deux in Alzheimer's disease. *Nat. Rev. Neurosci.*, **12**, 65–72, Nature Publishing Group. doi:10.1038/nrn2967

Janke, C. (2014) The tubulin code: Molecular components, readout mechanisms, functions. *J. Cell Biol.*, **206**, 461–472. doi:10.1083/jcb.201406055

Jin, X., Mohieldin, A.M., Muntean, B.S., Green, J.A., Shah, J. V., Mykytyn, K. & Nauli, S.M. (2014) Cilioplasm is a cellular compartment for calcium signaling in response to mechanical and chemical stimuli. *Cell. Mol. Life Sci.*, **71**, 2165–78. doi:10.1007/s00018-013-1483-1

Jordan, M.A., Diener, D.R., Stepanek, L. & Pigino, G. (2018) The cryo-EM structure of intraflagellar transport trains reveals how dynein is inactivated to ensure unidirectional anterograde movement in cilia. *Nat. Cell Biol.*, **20**, 1250–1255, Springer US. doi:10.1038/s41556-018-0213-1

Jumeau, F., Chalmel, F., Fernandez-Gomez, F.-J., Carpentier, C., Obriot, H., Tardivel, M., Caillet-Boudin, M.-L., *et al.* (2017) Defining the human sperm microtubulome: an integrated genomics approach. *Biol. Reprod.*, **96**, 93–106. doi:10.1095/biolreprod.116.143479

Kadavath, H., Cabrales Fontela, Y., Jaremko, M., Jaremko, Ł., Overkamp, K., Biernat, J., Mandelkow, E., *et al.* (2018) The Binding Mode of a Tau Peptide with Tubulin. *Angew. Chem. Int. Ed. Engl.*, **57**, 3246–3250. doi:10.1002/anie.201712089

Kadavath, H., Hofele, R. V., Biernat, J., Kumar, S., Tepper, K., Urlaub, H., Mandelkow, E., *et al.* (2015) Tau stabilizes microtubules by binding at the interface between tubulin heterodimers. *Proc. Natl. Acad. Sci. U. S. A.*, **112**, 7501–6. doi:10.1073/pnas.1504081112

Kalebic, N., Martinez, C., Perlas, E., Hublitz, P., Bilbao-Cortes, D., Fiedorczuk, K., Andolfo, A., *et al.* (2013) Tubulin Acetyltransferase αTAT1 Destabilizes Microtubules Independently of Its Acetylation Activity. *Mol. Cell. Biol.*, **33**, 1114–1123. doi:10.1128/mcb.01044-12

Kalebic, N., Sorrentino, S., Perlas, E., Bolasco, G., Martinez, C. & Heppenstall, P.A. (2013) αTAT1 is the major α-tubulin acetyltransferase in mice. *Nat. Commun.*, **4**, 1962. doi:10.1038/ncomms2962

Kar, S., Fan, J., Smith, M.J., Goedert, M. & Amos, L.A. (2003) Repeat motifs of tau bind to the insides of microtubules in the absence of taxol. *EMBO J.*, **22**, 70–7. doi:10.1093/emboj/cdg001

Kee, H.L., Dishinger, J.F., Blasius, T.L., Liu, C.-J., Margolis, B. & Verhey, K.J. (2012) A size-exclusion permeability barrier and nucleoporins characterize a ciliary pore complex that regulates transport into cilia. *Nat. Cell Biol.*, **14**, 431–7, Nature Publishing Group. doi:10.1038/ncb2450

Kellogg, E.H., Hejab, N.M.A., Howes, S., Northcote, P., Miller, J.H., Díaz, J.F., Downing, K.H., *et al.* (2017) Insights into the Distinct Mechanisms of Action of Taxane and Non-Taxane Microtubule Stabilizers from Cryo-EM Structures. *J. Mol. Biol.*, **429**, 633–646, The Authors. doi:10.1016/j.jmb.2017.01.001

Kennedy-Darling, J. & Smith, L.M. (2014) Measuring the formaldehyde Protein-DNA cross-link reversal rate. *Anal. Chem.*, **86**, 5678–81. doi:10.1021/ac501354y

Kiesel, P., Alvarez Viar, G., Tsoy, N., Maraspini, R., Gorilak, P., Varga, V., Honigmann, A., *et al.* (2020) The molecular structure of mammalian primary cilia revealed by cryo-electron tomography. *Nat. Struct. Mol. Biol.*, **27**, 1115–1124, Springer US. doi:10.1038/s41594-020-0507-4

Kim, D.I., Birendra, K.C., Zhu, W., Motamedchaboki, K., Doye, V. & Roux, K.J. (2014) Probing nuclear pore complex architecture with proximity-dependent biotinylation. *Proc. Natl. Acad. Sci. U. S. A.*, **111**, E2453-61. doi:10.1073/pnas.1406459111

Kim, S. & Dynlacht, B.D. (2013) Assembling a primary cilium. *Curr. Opin. Cell Biol.*, **25**, 506–11, Elsevier Ltd. doi:10.1016/j.ceb.2013.04.011

Kirima, J. & Oiwa, K. (2018) Flagellar-associated Protein FAP85 Is a Microtubule Inner Protein That Stabilizes Microtubules. *Cell Struct. Funct.*, **43**, 1–14. doi:10.1247/csf.17023

Kohl, L. & Bastin, P. (2005) The flagellum of trypanosomes. *Int. Rev. Cytol.*, **244**, 227–85. doi:10.1016/S0074-7696(05)44006-1

Koning, R.I., Zovko, S., Bárcena, M., Oostergetel, G.T., Koerten, H.K., Galjart, N., Koster, A.J., *et al.* (2008) Cryo electron tomography of vitrified fibroblasts: microtubule plus ends in situ. *J. Struct. Biol.*, **161**, 459–68. doi:10.1016/j.jsb.2007.08.011

Kormendi, V., Szyk, A., Piszczek, G. & Roll-Mecak, A. (2012) Crystal structures of tubulin acetyltransferase reveal a conserved catalytic core and the plasticity of the essential N terminus. *J. Biol. Chem.*, **287**, 41569–75. doi:10.1074/jbc.C112.421222

L'Hernault, S.W. & Rosenbaum, J.L. (1985) Chlamydomonas alpha-tubulin is posttranslationally modified by acetylation on the epsilon-amino group of a lysine. *Biochemistry*, **24**, 473–8. doi:10.1021/bi00323a034

Larochelle, M., Bergeron, D., Arcand, B. & Bachand, F. (2019) Proximity-dependent biotinylation mediated by TurboID to identify protein-protein interaction networks in yeast. *J. Cell Sci.*, **132**. doi:10.1242/jcs.232249

LeDizet, M. & Piperno, G. (1986) Cytoplasmic microtubules containing acetylated alpha-tubulin in Chlamydomonas reinhardtii: spatial arrangement and properties. *J. Cell Biol.*, **103**, 13–22. doi:10.1083/jcb.103.1.13

Lefèvre, J., Savarin, P., Gans, P., Hamon, L., Clément, M.J., David, M.O., Bosc, C., *et al.* (2013) Structural basis for the association of MAP6 protein with microtubules and its regulation by calmodulin. *J. Biol. Chem.*, **288**, 24910–24922. doi:10.1074/jbc.M113.457267

Letournel, F., Bocquet, A., Dubas, F., Barthelaix, A. & Eyer, J. (2003) Stable tubule only polypeptides (STOP) proteins co-aggregate with spheroid neurofilaments in amyotrophic lateral sclerosis. *J. Neuropathol. Exp. Neurol.*, **62**, 1211–9. doi:10.1093/jnen/62.12.1211

Leung, M.R., Roelofs, M.C., Ravi, R.T., Maitan, P., Henning, H., Zhang, M., Bromfield, E.G., *et al.* (2021) The multi-scale architecture of mammalian sperm flagella and implications for ciliary motility. *EMBO J.*, **40**, e107410. doi:10.15252/embj.2020107410

Li, Haorong, Frankenfield, A.M., Houston, R., Sekine, S. & Hao, L. (2021) Thiol-Cleavable Biotin for Chemical and Enzymatic Biotinylation and Its Application to Mitochondrial TurboID Proteomics. *J. Am. Soc. Mass Spectrom.* doi:10.1021/jasms.1c00079

Li, Huilin, DeRosier, D.J., Nicholson, W. V., Nogales, E. & Downing, K.H. (2002) Microtubule structure at 8 Å resolution. *Structure*, **10**, 1317–28. doi:10.1016/S0969-2126(02)00827-4

Lin, J. & Nicastro, D. (2018) Asymmetric distribution and spatial switching of dynein activity generates ciliary motility. *Science*, **360**. doi:10.1126/science.aar1968

Lin, S., Sterling, N.A., Junker, I.P., Helm, C.T. & Smith, G.M. (2017) Effects of αTAT1 and HDAC5 on axonal regeneration in adult neurons. (S. Di Giovanni, Ed.)*PLoS One*, **12**, e0177496. doi:10.1371/journal.pone.0177496

Ludueña, R.F., Shooter, E.M. & Wilson, L. (1977) Structure of the tubulin dimer. *J. Biol. Chem.*, **252**, 7006–14. doi:10.1016/s0021-9258(19)66927-9

Ma, M., Stoyanova, M., Rademacher, G., Dutcher, S.K., Brown, A. & Zhang, R. (2019) Structure of the Decorated Ciliary Doublet Microtubule. *Cell*, **179**, 909-922.e12, Elsevier Inc. doi:10.1016/j.cell.2019.09.030

MacTaggart, B. & Kashina, A. (2021) Posttranslational modifications of the cytoskeleton. *Cytoskeleton (Hoboken).*, 1–32. doi:10.1002/cm.21679

Mair, A., Xu, S.-L., Branon, T.C., Ting, A.Y. & Bergmann, D.C. (2019) Proximity labeling of protein complexes and cell-type-specific organellar proteomes in Arabidopsis enabled by TurboID. *Elife*, **8**, 1–45. doi:10.7554/eLife.47864

Marshall, W.F. & Rosenbaum, J.L. (2001) Intraflagellar transport balances continuous turnover of

outer doublet microtubules: implications for flagellar length control. *J. Cell Biol.*, **155**, 405–14. doi:10.1083/jcb.200106141

May, D.G., Scott, K.L., Campos, A.R. & Roux, K.J. (2020) Comparative Application of BioID and TurboID for Protein-Proximity Biotinylation. *Cells*, **9**. doi:10.3390/cells9051070

Mitchison, T. & Kirschner, M. (1984) Dynamic instability of microtubule growth. *Nature*, **312**, 237–42. doi:10.1038/309126a0

Miyake, Y., Keusch, J.J., Wang, L., Saito, M., Hess, D., Wang, X., Melancon, B.J., *et al.* (2016) Structural insights into HDAC6 tubulin deacetylation and its selective inhibition. *Nat. Chem. Biol.*, **12**, 748–54, Nature Publishing Group. doi:10.1038/nchembio.2140

Moores, C.A., Perderiset, M., Francis, F., Chelly, J., Houdusse, A. & Milligan, R.A. (2004) Mechanism of microtubule stabilization by doublecortin. *Mol. Cell*, **14**, 833–9. doi:10.1016/j.molcel.2004.06.009

Nekooki-Machida, Y., Nakakura, T., Nishijima, Y., Tanaka, H., Arisawa, K., Kiuchi, Y., Miyashita, T., *et al.* (2018) Dynamic localization of α-tubulin acetyltransferase ATAT1 through the cell cycle in human fibroblastic KD cells. *Med. Mol. Morphol.*, **51**, 217–226, Springer Japan. doi:10.1007/s00795-018-0195-x

Nicastro, D., Fu, X., Heuser, T., Tso, A., Porter, M.E. & Linck, R.W. (2011) Cryo-electron tomography reveals conserved features of doublet microtubules in flagella. *Proc. Natl. Acad. Sci. U. S. A.*, **108**, E845-53. doi:10.1073/pnas.1106178108

Nicastro, D., McIntosh, J.R. & Baumeister, W. (2005) 3D structure of eukaryotic flagella in a quiescent state revealed by cryo-electron tomography. *Proc. Natl. Acad. Sci. U. S. A.*, **102**, 15889–94. doi:10.1073/pnas.0508274102

Nicastro, D., Schwartz, C., Pierson, J., Gaudette, R., Porter, M.E. & McIntosh, J.R. (2006) The molecular architecture of axonemes revealed by cryoelectron tomography. *Science*, **313**, 944–8. doi:10.1126/science.1128618

Nihongaki, Y., Matsubayashi, H.T. & Inoue, T. (2021) A molecular trap inside microtubules probes luminal access by soluble proteins. *Nat. Chem. Biol.*, **17**, 888–895, Springer US. doi:10.1038/s41589-021-00791-w

Nogales, E., Whittaker, M., Milligan, R.A. & Downing, K.H. (1999) High-resolution model of the microtubule. *Cell*, **96**, 79–88. doi:10.1016/S0092-8674(00)80961-7

Nogales, E., Wolf, S.G. & Downing, K.H. (1998) Structure of the αβ tubulin dimer by electron crystallography. *Nature*, **391**, 199–203. doi:10.1038/34465

Nogales, E., Wolf, S.G., Khan, I.A., Ludueña, R.F. & Downing, K.H. (1995) Structure of tubulin at 6.5 A and location of the taxol-binding site. *Nature*, **375**, 424–7. doi:10.1038/375424a0

Nonaka, S., Tanaka, Y., Okada, Y., Takeda, S., Harada, A., Kanai, Y., Kido, M., *et al.* (1998) Randomization of left-right asymmetry due to loss of nodal cilia generating leftward flow of extraembryonic fluid in mice lacking KIF3B motor protein. *Cell*, **95**, 829–37. doi:10.1016/S0092-8674(00)81705-5

North, B.J., Marshall, B.L., Borra, M.T., Denu, J.M. & Verdin, E. (2003) The human Sir2 ortholog, SIRT2, is an NAD+-dependent tubulin deacetylase. *Mol. Cell*, **11**, 437–44. doi:10.1016/S1097-2765(03)00038-8

Oda, T., Yanagisawa, H., Kamiya, R. & Kikkawa, M. (2014) A molecular ruler determines the repeat length in eukaryotic cilia and flagella. *Science*, **346**, 857–60. doi:10.1126/science.1260214

Oda, T., Yanagisawa, H. & Kikkawa, M. (2014) Detailed structural and biochemical characterization of the nexin-dynein regulatory complex. (W. Marshall, Ed.)*Mol. Biol. Cell*, **26**, 294–304. doi:10.1091/mbc.E14-09-1367

Odde, D.J. (1998) Diffusion inside microtubules. *Eur. Biophys. J.*, **27**, 514–20. doi:10.1007/s002490050161

Odde, D.J., Cassimeris, L. & Buettner, H.M. (1995) Kinetics of microtubule catastrophe assessed by probabilistic analysis. *Biophys. J.*, **69**, 796–802, Elsevier. doi:10.1016/S0006-3495(95)79953-2

Orbach, R. & Howard, J. (2019) The dynamic and structural properties of axonemal tubulins support the high length stability of cilia. *Nat. Commun.*, **10**, 1838, Springer US. doi:10.1038/s41467-019-09779-6

Owa, M., Uchihashi, T., Yanagisawa, H., Yamano, T., Iguchi, H., Fukuzawa, H., Wakabayashi, K., *et*

al. (2019) Inner lumen proteins stabilize doublet microtubules in cilia and flagella. *Nat. Commun.*, **10**, 1143, Springer US. doi:10.1038/s41467-019-09051-x

Patel, A., Malinovska, L., Saha, S., Wang, J., Alberti, S., Krishnan, Y. & Hyman, A.A. (2017) ATP as a biological hydrotrope. *Science*, **356**, 753–756. doi:10.1126/science.aaf6846

Paul, D.M., Mantell, J., Borucu, U., Coombs, J., Surridge, K.J., Squire, J.M., Verkade, P., *et al.* (2020) In situ cryo-electron tomography reveals filamentous actin within the microtubule lumen. *J. Cell Biol.*, **219**. doi:10.1083/JCB.201911154

Perdiz, D., Mackeh, R., Poüs, C. & Baillet, A. (2011) The ins and outs of tubulin acetylation: more than just a post-translational modification? *Cell. Signal.*, **23**, 763–71, Elsevier Inc. doi:10.1016/j.cellsig.2010.10.014

Pigino, G., Maheshwari, A., Bui, K.H., Shingyoji, C., Kamimura, S. & Ishikawa, T. (2012) Comparative structural analysis of eukaryotic flagella and cilia from Chlamydomonas, Tetrahymena, and sea urchins. *J. Struct. Biol.*, **178**, 199–206, Elsevier Inc. doi:10.1016/j.jsb.2012.02.012

Pinto-Costa, R. & Sousa, M.M. (2021) Microtubules, actin and cytolinkers: how to connect cytoskeletons in the neuronal growth cone. *Neurosci. Lett.*, **747**, 135693, Elsevier B.V. doi:10.1016/j.neulet.2021.135693

Piperno, G. & Fuller, M.T. (1985) Monoclonal antibodies specific for an acetylated form of alpha-tubulin recognize the antigen in cilia and flagella from a variety of organisms. *J. Cell Biol.*, **101**, 2085–94. doi:10.1083/jcb.101.6.2085

Popov, K.I., Makepeace, K.A.T., Petrotchenko, E. V., Dokholyan, N. V. & Borchers, C.H. (2019) Insight into the Structure of the 'Unstructured' Tau Protein. *Structure*, **27**, 1710-1715.e4, Elsevier Ltd. doi:10.1016/j.str.2019.09.003

Poüs, C., Chabin, K., Drechou, A., Barbot, L., Phung-Koskas, T., Settegrana, C., Bourguet-Kondracki, M.L., *et al.* (1998) Functional specialization of stable and dynamic microtubules in protein traffic in WIF-B cells. *J. Cell Biol.*, **142**, 153–65. doi:10.1083/jcb.142.1.153

Prensier, G., Vivier, E., Goldstein, S. & Schrével, J. (1980) Motile flagellum with a '3 + 0' ultrastructure. *Science*, **207**, 1493–4. doi:10.1126/science.7189065

Pu, Y., Liu, Z., Lu, Y., Yuan, P., Liu, J., Yu, B., Wang, G., *et al.* (2015) Using DNA aptamer probe for immunostaining of cancer frozen tissues. *Anal. Chem.*, **87**, 1919–24. doi:10.1021/ac504175h

Rodríguez Echandía, E.L., Piezzi, R.S. & Rodríguez, E.M. (1968) Dense-core microtubules in neurons and gliocytes of the toad Bufo arenarum Hensel. *Am. J. Anat.*, **122**, 157–66. doi:10.1002/aja.1001220110

Roostalu, J., Thomas, C., Cade, N.I., Kunzelmann, S., Taylor, I.A. & Surrey, T. (2020) The speed of GTP hydrolysis determines GTP cap size and controls microtubule stability. *Elife*, **9**, 1–22. doi:10.7554/eLife.51992

Roux, K.J., Kim, D.I., Raida, M. & Burke, B. (2012) A promiscuous biotin ligase fusion protein identifies proximal and interacting proteins in mammalian cells. *J. Cell Biol.*, **196**, 801–10. doi:10.1083/jcb.201112098

San Agustin, J.T., Pazour, G.J. & Witman, G.B. (2015) Intrafagellar transport is essential for mammalian spermiogenesis but is absent in mature sperm. *Mol. Biol. Cell*, **26**, 4358–4372. doi:10.1091/mbc.E15-08-0578

Sandborn, E., Koen, P.F., McNabb, J.D. & Moore, G. (1964) Cytoplasmic microtubules in mammalian cells. *J. Ultrastruct. Res.*, **11**, 123–138. doi:10.1016/S0022-5320(64)80097-6

Schaedel, L., John, K., Gaillard, J., Nachury, M. V., Blanchoin, L. & Théry, M. (2015) Microtubules self-repair in response to mechanical stress. *Nat. Mater.*, **14**, 1156–63. doi:10.1038/nmat4396

Schaefer, A.W., Kabir, N. & Forscher, P. (2002) Filopodia and actin arcs guide the assembly and transport of two populations of microtubules with unique dynamic parameters in neuronal growth cones. *J. Cell Biol.*, **158**, 139–52. doi:10.1083/jcb.200203038

Schiff, P.B., Fant, J. & Horwitz, S.B. (1979) Promotion of microtubule assembly in vitro by taxol. *Nature*, **277**, 665–7. doi:10.1038/277665a0

Schindelin, J., Arganda-Carreras, I., Frise, E., Kaynig, V., Longair, M., Pietzsch, T., Preibisch, S., *et al.* (2012) Fiji: an open-source platform for biological-image analysis. *Nat. Methods*, **9**, 676–82. doi:10.1038/nmeth.2019

Schliwa, M., Euteneuer, U., Bulinski, J.C. & Izant, J.G. (1981) Calcium lability of cytoplasmic microtubules and its modulation by microtubule-associated proteins. *Proc. Natl. Acad. Sci. U. S. A.*, **78**, 1037–41. doi:10.1073/pnas.78.2.1037

Schmidt, W.J. (1939) Doppelbrechung der Kernspindel und Zugfasertheorie der Chromosomenbewegung. *Chromosoma*, **1**, 253–264. doi:10.1007/BF01271634

Schroer, T.A., Steuer, E.R. & Sheetz, M.P. (1989) Cytoplasmic dynein is a minus end-directed motor for membranous organelles. *Cell*, **56**, 937–46. doi:10.1016/0092-8674(89)90627-2

Shida, T., Cueva, J.G., Xu, Z., Goodman, M.B. & Nachury, M. V. (2010) The major alpha-tubulin K40 acetyltransferase alphaTAT1 promotes rapid ciliogenesis and efficient mechanosensation. *Proc. Natl. Acad. Sci. U. S. A.*, **107**, 21517–22. doi:10.1073/pnas.1013728107

Shimizu, H., Iwayama, Y., Yamada, K., Toyota, T., Minabe, Y., Nakamura, K., Nakajima, M., *et al.* (2006) Genetic and expression analyses of the STOP (MAP6) gene in schizophrenia. *Schizophr. Res.*, **84**, 244–52. doi:10.1016/j.schres.2006.03.017

Skultetyova, L., Ustinova, K., Kutil, Z., Novakova, Z., Pavlicek, J., Mikesova, J., Trapl, D., *et al.* (2017) Human histone deacetylase 6 shows strong preference for tubulin dimers over assembled microtubules. *Sci. Rep.*, **7**, 11547, Springer US. doi:10.1038/s41598-017-11739-3

Slautterback, D.B. (1963) Cytoplasmic microtubules: I. Hydra. *J. Cell Biol.*, **18**, 367–388. doi:10.1083/jcb.18.2.367

Sloboda, R.D. (2015) Isolation of microtubules and microtubule-associated proteins using Paclitaxel. *Cold Spring Harb. Protoc.*, **2015**, pdb.prot081190. doi:10.1101/pdb.prot081190

Soppina, V., Herbstman, J.F., Skiniotis, G. & Verhey, K.J. (2012) Luminal localization of α-tubulin K40 acetylation by cryo-EM analysis of fab-labeled microtubules. *PLoS One*, **7**, e48204. doi:10.1371/journal.pone.0048204

Stadler, C., Rexhepaj, E., Singan, V.R., Murphy, R.F., Pepperkok, R., Uhlén, M., Simpson, J.C., *et al.* (2013) Immunofluorescence and fluorescent-protein tagging show high correlation for protein localization in mammalian cells. *Nat. Methods*, **10**, 315–23. doi:10.1038/nmeth.2377

Stanley, H.P., Bowman, J.T., Romrell, L.J., Reed, S.C. & Wilkinson, R.F. (1972) Fine structure of normal spermatid differentiation in Drosophila melanogaster. *J. Ultrastruct. Res.*, **41**, 433–66. doi:10.1016/s0022-5320(72)90049-4

Stoddard, D., Zhao, Y., Bayless, B.A., Gui, L., Louka, P., Dave, D., Suryawanshi, S., *et al.* (2018) Tetrahymena RIB72A and RIB72B are microtubule inner proteins in the ciliary doublet microtubules. (T. Surrey, Ed.)*Mol. Biol. Cell*, **29**, 2566–2577. doi:10.1091/mbc.E18-06-0405

Szyk, A., Deaconescu, A.M., Spector, J., Goodman, B., Valenstein, M.L., Ziolkowska, N.E., Kormendi, V., *et al.* (2014) Molecular basis for age-dependent microtubule acetylation by tubulin acetyltransferase. *Cell*, **157**, 1405–15, Elsevier Inc. doi:10.1016/j.cell.2014.03.061

Taschner, M., Vetter, M. & Lorentzen, E. (2012) Atomic resolution structure of human α-tubulin acetyltransferase bound to acetyl-CoA. *Proc. Natl. Acad. Sci. U. S. A.*, **109**, 19649–54. doi:10.1073/pnas.1209343109

Tilney, L.G., Bryan, J., Bush, D.J., Fujiwara, K., Mooseker, M.S., Murphy, D.B. & Snyder, D.H. (1973) Microtubules: evidence for 13 protofilaments. *J. Cell Biol.*, **59**, 267–75. doi:10.1083/jcb.59.2.267

Topalidou, I., Keller, C., Kalebic, N., Nguyen, K.C.Q., Somhegyi, H., Politi, K.A., Heppenstall, P., *et al.* (2012) Genetically separable functions of the MEC-17 tubulin acetyltransferase affect microtubule organization. *Curr. Biol.*, **22**, 1057–65, Elsevier Ltd. doi:10.1016/j.cub.2012.03.066

Tung, J.W., Heydari, K., Tirouvanziam, R., Sahaf, B., Parks, D.R., Herzenberg, L.A. & Herzenberg, L.A. (2007) Modern flow cytometry: a practical approach. *Clin. Lab. Med.*, **27**, 453–68, v. doi:10.1016/j.cll.2007.05.001

UniProtKB - Q96JE9 (MAP6_HUMAN). (2021) . Retrieved August 8, 2021, from https://www.uniprot.org/uniprot/Q96JE9#structure

Vallee, R.B. (1982) A taxol-dependent procedure for the isolation of microtubules and microtubule-associated proteins (MAPs). *J. Cell Biol.*, **92**, 435–42. doi:10.1083/jcb.92.2.435

Varnaitė, R. & MacNeill, S.A. (2016) Meet the neighbors: Mapping local protein interactomes by proximity-dependent labeling with BioID. *Proteomics*, **16**, 2503–2518. doi:10.1002/pmic.201600123

Vaughan, S., Shaw, M. & Gull, K. (2006) A post-assembly structural modification to the lumen of

flagellar microtubule doublets. *Curr. Biol.*, **16**, 449–450. doi:10.1016/j.cub.2006.05.041
Verhey, K.J. & Yang, W. (2016) Permeability barriers for generating a unique ciliary protein and lipid composition. *Curr. Opin. Cell Biol.*, **41**, 109–16, Elsevier Ltd. doi:10.1016/j.ceb.2016.05.004
Wagner, J., Schaffer, M. & Fernández-Busnadiego, R. (2017) Cryo-electron tomography—the cell biology that came in from the cold. *FEBS Lett.*, **591**, 2520–2533. doi:10.1002/1873-3468.12757
Walker, R. a, O'Brien, E.T., Pryer, N.K., Soboeiro, M.F., Voter, W.A., Erickson, H.P. & Salmon, E.D. (1988) Dynamic instability of individual microtubules analyzed by video light microscopy: rate constants and transition frequencies. *J. Cell Biol.*, **107**, 1437–48. doi:10.1083/jcb.107.4.1437
Walton, T., Wu, H. & Brown, A. (2021) Structure of a microtubule-bound axonemal dynein. *Nat. Commun.*, **12**, 477, Springer US. doi:10.1038/s41467-020-20735-7
Wang, X., Fu, Y., Beatty, W.L., Ma, M., Brown, A., David Sibley, L. & Zhang, R. (2021) Cryo-EM structure of cortical microtubules from human parasite Toxoplasma gondii identifies their microtubule inner proteins. *Nat. Commun.*, **12**, 1–14, Springer US. doi:10.1038/s41467-021-23351-1
Weaver, B.A. (2014) How Taxol/paclitaxel kills cancer cells. *Mol. Biol. Cell*, **25**, 2677–81. doi:10.1091/mbc.E14-04-0916
Weber, P.C., Ohlendorf, D.H., Wendoloski, J.J. & Salemme, F.R. (1989) Structural origins of high-affinity biotin binding to streptavidin. *Science*, **243**, 85–8. doi:10.1126/science.2911722
Webster, D.R. & Borisy, G.G. (1989) Microtubules are acetylated in domains that turn over slowly. *J. Cell Sci.*, **92 (Pt 1)**, 57–65. doi:10.1242/jcs.92.1.57
Witman, G.B., Carlson, K., Berliner, J. & Rosenbaum, J.L. (1972) Chlamydomonas flagella. I. Isolation and electrophoretic analysis of microtubules, matrix, membranes, and mastigonemes. *J. Cell Biol.*, **54**, 507–39. doi:10.1083/jcb.54.3.507
Witman, G.B., Carlson, K. & Rosenbaum, J.L. (1972) Chlamydomonas flagella. II. The distribution of tubulins 1 and 2 in the outer doublet microtubules. *J. Cell Biol.*, **54**, 540–55. Retrieved from http://www.ncbi.nlm.nih.gov/pubmed/5044758
Woods, A., Sherwin, T., Sasse, R., MacRae, T.H., Baines, A.J. & Gull, K. (1989) Definition of individual components within the cytoskeleton of Trypanosoma brucei by a library of monoclonal antibodies. *J. Cell Sci.*, **93 (Pt 3)**, 491–500. Retrieved from http://www.ncbi.nlm.nih.gov/pubmed/2606940
Xiao, H., Wang, H., Zhang, X., Tu, Z., Bulinski, C., Khrapunovich-Baine, M., Hogue Angeletti, R., *et al.* (2012) Structural evidence for cooperative microtubule stabilization by Taxol and the endogenous dynamics regulator MAP4. *ACS Chem. Biol.*, **7**, 744–52. doi:10.1021/cb200403x
Xu, Z. & Afzelius, B.A. (1988) The substructure of marginal bundles in human blood platelets. *J. Ultrastruct. Mol. Struct. Res.*, **99**, 244–53. doi:10.1016/0889-1605(88)90068-7
Yajima, H., Ogura, T., Nitta, R., Okada, Y., Sato, C. & Hirokawa, N. (2012) Conformational changes in tubulin in GMPCPP and GDP-taxol microtubules observed by cryoelectron microscopy. *J. Cell Biol.*, **198**, 315–22. doi:10.1083/jcb.201201161
Young, S.A.M., Miyata, H., Satouh, Y., Aitken, R.J., Baker, M.A. & Ikawa, M. (2016) CABYR is essential for fibrous sheath integrity and progressive motility in mouse spermatozoa. *J. Cell Sci.*, **129**, 4379–4387. doi:10.1242/jcs.193151
Zabeo, D. (2021) *Revealing the architecture and composition of the sperm flagellum tip*, University of Gothenburg, Faculty of Science. Retrieved from http://hdl.handle.net/2077/67318
Zabeo, D., Croft, J.T. & Höög, J.L. (2019) Axonemal doublet microtubules can split into two complete singlets in human sperm flagellum tips. *FEBS Lett.*, **593**, 892–902. doi:10.1002/1873-3468.13379
Zabeo, D., Heumann, J.M., Schwartz, C.L., Suzuki-Shinjo, A., Morgan, G., Widlund, P.O. & Höög, J.L. (2018) A lumenal interrupted helix in human sperm tail microtubules. *Sci. Rep.*, **8**, 2727. doi:10.1038/s41598-018-21165-8
Zhao, H.L., Yao, X.Q., Xue, C., Wang, Y., Xiong, X.H. & Liu, Z.M. (2008) Increasing the homogeneity, stability and activity of human serum albumin and interferon-alpha2b fusion protein by linker engineering. *Protein Expr. Purif.*, **61**, 73–7. doi:10.1016/j.pep.2008.04.013
Zimmermann, I., Egloff, P., Hutter, C.A.J., Kuhn, B.T., Bräuer, P., Newstead, S., Dawson, R.J.P., *et al.* (2020) Generation of synthetic nanobodies against delicate proteins. *Nat. Protoc.*, **15**, 1707–1741, Springer US. doi:10.1038/s41596-020-0304-x